Theses and Dissertations

2016

Development of Novel High-Throughput Methodologies to Evaluate the Thermal Stability of High-Temperature Thin-Film Crystals for Energy Applications

Jonathan Kenneth Bunn
University of South Carolina

Follow this and additional works at: https://scholarcommons.sc.edu/etd

Part of the Chemical Engineering Commons

www.manaraa.com

Development of Novel High-Throughput Methodologies to Evaluate the Thermal Stability of High-Temperature Thin-Film Crystals for Energy Applications

by

Jonathan Kenneth Bunn

Bachelor of Science
University of South Carolina 2012

_____

Submitted in Partial Fulfillment of the Requirements

for the Degree of Doctor of Philosophy in

Chemical Engineering

College of Engineering and Computing

University of South Carolina

2016

Accepted by:

Jason Hattrick-Simpers, Major Professor

Kevin Huang, Committee Member

Ralph White, Committee Member

Edward Gatzke, Committee Member

John Weidner, Committee Member

Cheryl L. Addy, Vice Provost and Dean of the Graduate School

ii

DEDICATION

To my loving wife.

ACKNOWLEDGMENTS

with.

Thanks to all of the undergraduates that have worked with me over the years. To Randy Fang, Rachel Smoak, Mark Albing, and Patrick Barboun; you were a great asset to my research, working tirelessly over summers and semesters to accomplish great things. I know it was my job to be a mentor to you, and I hope that I was able to teach you a tenth of what you taught me.

Everyone else who has worked at SAGE in the past and present; I thank you. I have enjoyed collaborating with you and working side-by-side with you.

I extend my sincerest thank you to the rest of my committee members, Prof. Kevin Huang, Prof. Ralph White, Prof. Edward Gatzke, and Prof. John Weidner.

Richard Voepel, I thank you. Since I met you in undergraduates you have been one of my closest friends. The conversations we have had over the year, the 3:00 am trips to IHOP, the countless times we have argued on the back of napkins will always stay with me. You are a truly unique individual who motivated me to delve deeper into all subjects, especially mathematics and physics. You are a truly great man and a wonderful friend.

To my family, thank you. Mom and Dad, I could not have asked for better parents. You were always there for me while I was growing up, always showing me care and compassion even when I messed up. You fostered my sense of curiosity for the world around, teaching me to always ask questions and to be vigilant in finding the answers. You taught me that no mater what, I should strive to do whatever I wanted in life. Those lessons did me well, leading me to where I am now. Alex and Taylor, my brothers, thanks for putting up with your little brother all these years. I will always remember our childhood together and the lasting friendship we have developed. You two have taught me more about life than you will ever know.

To the dearest person in the world to me; my wife, I thank you the most. Without you I know I would not have made it this far. You have shown me more compassion

and understanding than I could have ever expected. You have, and will always be, my closest friend, confidant, and companion. I could never thank you enough for always being there for me and supporting me, no mater what. Dad always says that I am the lucky one in this marriage, and he is right. There is no one else I would rather be on this journey with.

Abstract

High temperature materials are used in a variety of energy applications such as jet turbines, high temperature sensors, and solid oxide fuel cells (SOFCs). Discovery of new materials and their optimization represents a difficult engineering challenge, as the materials have to be designed to have a high figure of merit during intense high temperature operations.

The large number of engineering considerations involved in the identification and optimization of such materials makes traditional one-by-one material investigations prohibitively time consuming. The time needed to explore large parameter domains can be significantly decreased through the use of high-throughput experimentation (HTE). HTE is an experimental paradigm where quick-serial or parallel techniques are used to create a "library" of samples covering multiple material parameters and then rapidly characterize the samples for their figure of merit.

This thesis will discuss development the of a HTE framework to investigate crystal phase dynamics of high-temperature thin-film materials and its use in the case-study investigations. The details associated with the design and validation of each portion of the HTE framework will be given, including the development of a sputter model that is used for model-guided sputtered thin-film synthesis, a novel HTE experimental methodology designed for the investigation of high-temperature thin-films, and a semi-supervised machine-learning algorithm is used to automatically extract phase information from the resulting diffraction and spectroscopy data. Finally, a detailed discussion of the application of the HTE framework to the investigation of corrosion resistant Fe-Cr-Al nuclear cladding materials and evaluation of scandia-stabilized-

zirconium and bismuth-yttria-ceria thin-films as SOFC electrolyte materials will be given.

Table of Contents

LIST OF TABLES

LIST OF FIGURES

xix

CHAPTER 1

INTRODUCTION

1.1 OVERVIEW

Within the energy generation sector, high temperature thin-films are used in a variety of applications. In many of these application, thin-films are used as protective layers for a bulk structural material, such as being the thermal barrier coatings/corrosion resistant coatings for high temperature jet turbines. Moreover, research focusing on using thin-films themselves for other applications, such as thin-film SOFC layers, has shown thin-films can be used to improve the performance of such technologies. Such thin-films represent a hard engineering challenge, as the thin-films need to be finely optimized to overcome obstacles that are intrinsic to the high temperature application itself, such as delamination due to thermal expansion mismatches between the film and the material it is attached to, and chemical resistance to the surrounding atmosphere. Furthermore, the thin-films must exhibit to have a high figure of merit, such as desirable ionic transport behavior, hardness, and electrical conductivity. One important aspect that underlies all of these concerns is the phase stability of the thin-film materials that are used. The specific crystal phase of a material controls many aspects of the desired properties, and governs how well the thin-film will perform. The crystal phases need to be stable at operating temperatures, and need to withstand thermal cycling the system will undergo during start-up and shut-down.

Due to the number of engineering considerations; traditional one-by-one material investigations, where a single sample has been synthesized and processed at a

1

single condition, take a significant amount of time. High-throughput experimentation (HTE) can be used to expedite the exploration and optimization of thin-film materials for energy applications. HTE is an experimental paradigm where multiple material parameters, such as composition and processing temperature, are varied simultaneously to create multiple samples on a "library". The individual samples of the library are then characterized using either quick-serial or parallel techniques, expediting materials exploration.

Two classes of high-temperature materials where phase stability is of the utmost importance are corrosion resistant materials and solid oxide fuel cell electrolyte materials. For both of these applications, phase transitions during operation can lead to suboptimal performance of the thin-film or can lead to film delamination and failure. If the thermal barrier coating of a jet turbine blade delaminates, the turbine blade itself can oxidize or melt leading to catastrophic turbine damage. If a solid oxide fuel cell electrolyte undergoes a crystal phase transition then the oxygen transport across entire fuel cell can dramatically decrease, yielding a reduction in the fuel cell ower output of the fuel cell. The large search domain that is associated with designing stable high-temperature systems make HTE the ideal device for materials exploration and optimization.

Here, the details of the HTE framework that I developed will be discussed and case studies about its application for the study of thin-film materials for two different classes of high-temperature energy applications will be presented. The first class of materials that will be discussed are corrosion resistant materials for application such as bond coats in jet turbines and protective coatings for nuclear cladding. The second class of materials that will be discussed are electrolyte materials for solid oxide fuel cells.

1.2 Corrosion Resistant Materials

One major application of high-temperature thin-films for energy applications is bond coats for gas and jet turbines. Currently, most gas and jet turbines are made out of nickel-based superalloys due to the high hardness and creep stress resistance of these materials at temperatures in excess of 1173 K [96]. Early efforts in turbine development showed that to increase the efficiency of turbines, the operation temperatures would need to be well above the melting temperature of the nickel-based superalloy materials [91]. To overcome this issue and to protect the superalloy from thermal damage, a layered coating is applied to the top of the superalloy, consisting of a bond coat, a thermally grown oxide, and a thermal barrier coating [20]. A diagram of the layered turbine assemble is shown in Fig. 1.1.
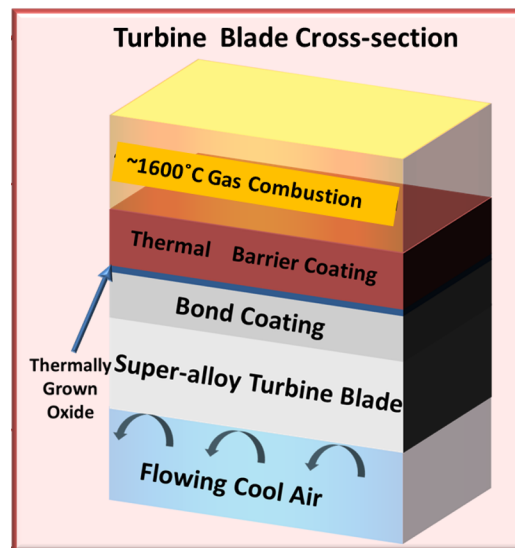
Figure 1.1   A schematic of the major layers of a high-temperature gas turbine.

The outermost later is a highly porous ceramic, such as meta-stable tetragonal (t') yttria-stabilized zirconia (YSZ). This ceramic layer is used to reduce the temperatures that the underlying super-alloy is exposed to, and is referred to as a thermal barrier coating (TBC) [20, 123]. Due to the large thermal expansion mismatches between

3

the TBC and the super-alloy, a layer is deposited between them called a bond coat (BC). This BC is generally made out of (Ni,Pt)-Al alloy or MCrAlY (where M is a transition metal), and is designed to thermally oxidize and preferentially form a passivating oxide at the high operating temperatures (>1273 K) [124, 132]. This oxide, called the thermally grown oxide (TGO), is typically α-Al$_2$O$_3$. α-Al$_2$O$_3$ has been selected as the passivating oxide due to its parabolic growth rate and high thermodynamic stability to moisture as compared to other oxides such as Cr$_2$O$_3$ [50]. Therefore, one of the main engineering goals when designing BCs is to promote the early exclusive formation of α-Al$_2$O$_3$ [34, 93].

Initially, there is a competition between the nucleation of multiple different oxides, including passivating α-Al$_2$O$_3$, NiO, and NiAl$_2$O$_6$. During the initial oxide growth, α-Al$_2$O$_3$ rarely forms, and instead first a mixture of metastable γ-Al$_2$O$_3$ and θ-Al$_2$O$_3$ nucleates at low temperatures. The metastable Al$_2$O$_3$ phases transition to α-Al$_2$O$_3$ at temperatures above 1273 K [51, 92, 140]. Due to the fact that an atomic rearrangement occurs during this phase transition, there is a significant decrease in oxide volume ($\sim5\%$). The stress developed in the TGO from the volume change is relieved by the formation of voids and cracks [51, 52]. The formation of voids, along with other factors such as thermal mismatch and diffusion of contaminants, can detrimentally lead to TGO delamination. The TBC on top of the TGO also delaminates, significantly decreasing the turbine lifespan [20]. Due to the gravity of BC and TGO failure, successful BC materials must exhibit preferential, if not exclusive, α-Al$_2$O$_3$ growth. This constraint has motivated the discovery of novel bond coat materials that form TGO with superior stability and corrosion resistance properties. This search is complicated, however, by the complex interdependency of the growth of the appropriate TGO with alloy composition, microstructure, interactions with the substrate, and the large range of possible alloying elements.

Another potential application of high-temperature thin-films for energy is protec-

tive coating for the nuclear rods inside power plants. These films could significantly mitigate the damage caused by a nuclear core meltdown. The process of containing the dangerous radioactive materials that form during a meltdown is further complicated by the potential of hydrogen explosions. These explosions can cause catastrophic damage to the containment structures of the affected and nearby reactors.

As the temperature within the reactor rises due to the run-away nuclear reaction, high-temperature, high-pressure steam is generated within the reactor. When temperature of the reactor exceeds 1473 K, the generated steam will oxidize the Zircaloy cladding material, forming ZrO_2 and hydrogen gas [131]. If the meltdown is not curbed quickly enough, the pressure of the concentrated hydrogen gas and steam reaches a point where it causes the containment dome around the reactor to rupture. When this occurs, the high-temperature hydrogen gas is introduced to the oxygen in air, causing it to react explosively. While these events are unlikely, discharge and ignition of high-pressure high-temperature hydrogen gas into the air is leading reason for the release of nuclear containments into the atmosphere from the recent nuclear disaster at the Fukushima Daiichi Nuclear Power Plant in 2011 and during the Chernobyl nuclear power plant disaster. [32].

To mitigate the risk of such events, investigations into the development of new, high-temperature (in excess of 1473 K [94]), oxidation-resistant nuclear cladding materials have begun. These investigations have mainly focused on replacing existing Zircaloy cladding materials with oxidation resistant alloys, such as Fe-Cr-Al [19, 24, 117]. Similar to the BC used in turbine applications, these alloys form a passivating α-Al_2O_3 layer when exposed to moisture and temperatures in excess of 1273 K [24, 121]. The content of Cr has to be finely controlled, as too much Cr will promote the growth of Cr_2O_3. In other lower temperature applications, Cr_2O_3 is a passivating oxide, but will react to moisture when exposed temperatures above 1273 K to form either CrO_3 which sublimes or a gaseous $CrO_2(OH)_2$ [14, 88]. Studies

5

have also shown that the desired passivating oxide forms on Fe-Cr-Al alloys with 5-20 at.% Cr and 5-10 at.% Al (balance Fe) in the presence of greater than 0.75 vol% O_2 [24, 97].

While Fe-Cr-Al alloys show promise as replacements for the Zircaloy cladding materials, the time needed for the certification process and re-design of current fuel rod assembly is a prohibitively lengthy processes [32]. An alternate solution to a complete replacement of current cladding materials is to add a corrosion resistant barrier coating on top of the cladding, capable of withstanding oxidation. To successfully translate bulk knowledge to a coating, further investigations of the oxidation behavior of Fe-Cr-Al thin-films need to be performed. Differences between bulk and thin-film material properties can stem from the non-equilibrium nature of coating synthesis techniques that are commonly used and the high probability that elements, specifically Al, could be depleted in a relatively short time-scale when compared to bulk Fe-Cr-Al alloys. This extreme sensitivity to composition coupled with the dynamic nature of the oxide growth and alloy composition means that a large number of Fe-Cr-Al compositions need to be investigated to ensure long term operation of the barrier coating.

1.3   Solid Oxide Fuel Cells

The need for more efficient ways of harnessing energy from carbon based fuels is imperative as the global demand for energy rises. A technology that shows significant promise in dramatically increasing this efficiency is fuel cells [119]. Fuel cells have the added advantage of creating lower amounts of pollutants, such as nitrogen oxides (NO_x), can easily be adapted to carbon capture technologies, and are not limited by the Carnot cycle due to the fact that they are not heat engines. This results in a reduction in the amount of CO_2 produced per kW*h of energy produced, while alleviating environmental concerns [119].

Two types of fuel cell technologies that have received a large amount of attention are proton exchange membrane fuel cells (PEMFCs) and solid oxide fuel cells (SOFCs). While PEMFCs operate at a lower temperature range than SOFCs (typically 353 K - 363 K[25] vs. 773 K - 1273 K[57]) they have the disadvantage of being limited to predominately using H_2 as a fuel source[126], requiring expensive precious metal ORR catalysts, and being highly susceptible to contaminants. SOFCs are fuel flexible as they can harness energy from various fuels such as H_2, LPG, biogas, and gasified coal [119]. SOFCs have also shown a high fuel efficiency (>55% of the lower heating value) and have shown 85% efficiency in combined heat and power applications that utilize waste heat [82, 111]. Furthermore, SOFCs do not require an expensive precious metal based catalyst to operate efficiently [111].

A SOFC is made up of three major parts: an anode, a cathode, and a solid oxide electrolyte, as shown in Fig. 1.2. SOFCs electro-chemically harness energy from a fuel source by flowing a gaseous fuel over the anode and oxygen over the cathode. The oxygen is reduced at the cathode to create a negatively charged oxygen ion. This oxygen ion then travels through the electrolyte to the anode. At the anode, the oxygen ion reacts with the fuel to create water, carbon dioxides, and free electrons. The free electrons pass back to the cathode via a conducting material, such as a wire, to create an electric circuit. Energy can then be harnessed from the electric circuit.

Yttria-stabilized zirconia (YSZ) is the traditional electrolyte material used in SOFCs [28]. The yttria addition stabilizes the cubic phase of zirconia and provides vacancy sites that increase oxygen ion diffusion through the lattice. However, YSZ has a large ionic resistance when the temperature of the electrolyte is below 1023 K, and for practical applications the operating temperature is generally above 1123 K [28, 136]. The high temperature increases the overall cost of SOFCs because expensive interconnect materials that are resistant to thermal shock and can operate at high temperatures are needed, and it is necessary to operate costly heat exchangers to

7
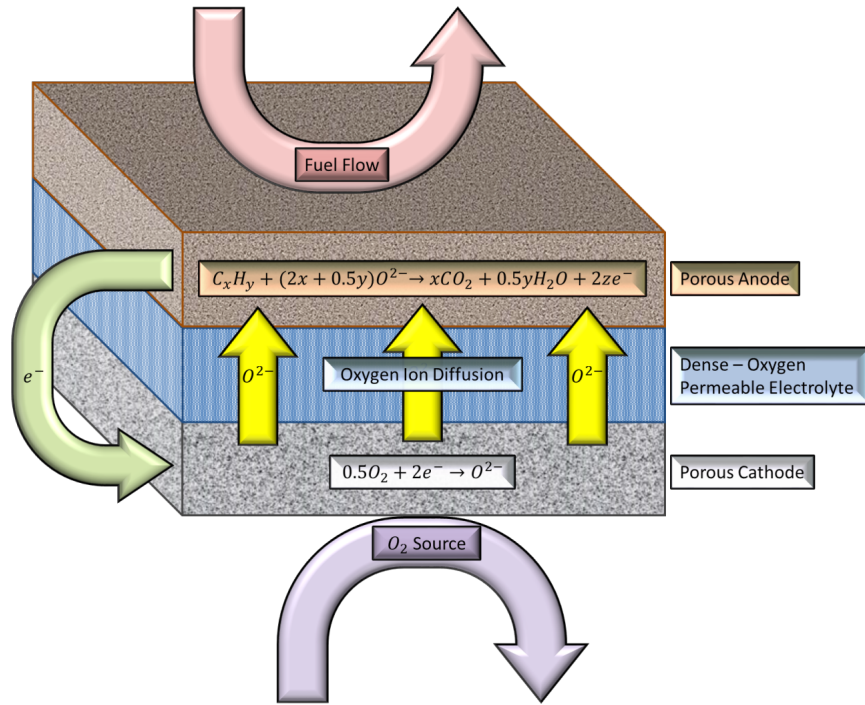
Figure 1.2   A Diagram outlining the major layers of a SOFC. The bottom later is a porous cathode; where oxygen anion initially diffuse into the SOFC and travel towards the electrolyte layer in the middle of the SOFC. Once the oxygen anion reaches the anode, shown at the top of the SOFC, it reacts with the surrounding fuel, releasing electrons. These free electrons travel back toward the cathode through an electronically conductive media, such as a metal wire, completing the electric circuit.

control the operating temperature. Furthermore, the high temperatures cause inter-diffusion and facilitate/accelerate reactions between the different major parts of the SOFC [57]. Inter-diffusion and reaction phenomena lowers the overall SOFC lifetime due to the chemical destruction of the major layers. Lowering the temperature of SOFCs operation would make them more economically competitive with traditional combustion methods, as both the initial capital required to build a SOFC and the operating cost would decrease. In order to lower the operation temperature, the electrolyte material can be replaced with a material that has a higher oxygen conductivity at intermediate temperatures. Multiple studies have been performed in search of a replacement material for YSZ[80, 109, 110, 128], and the results from some of these

studies are shown in Fig. 1.3.
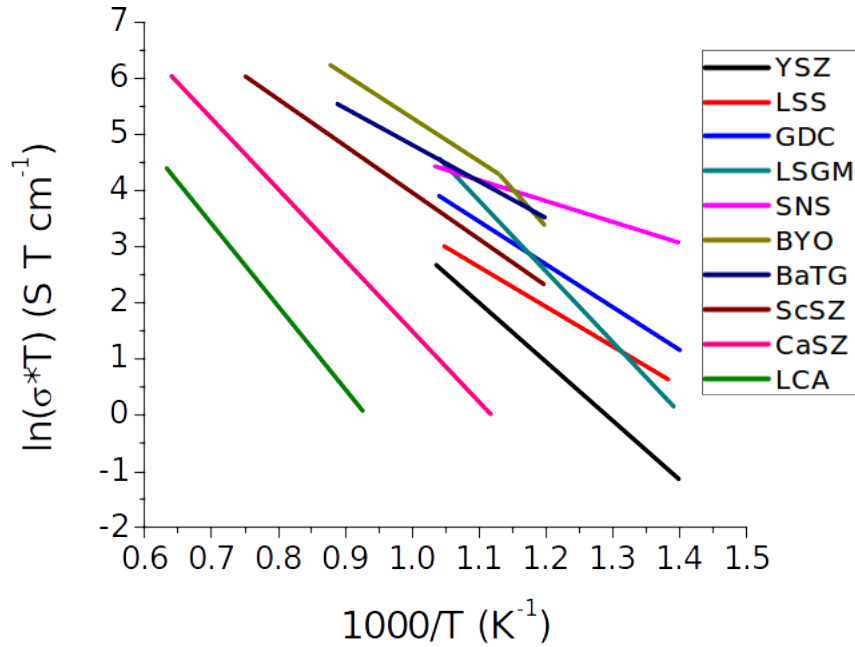
Figure 1.3   A diagram showing the oxygen ion conductivity of many SOFC electrolyte materials as a function of temperature. YSZ - yttria stabilized zirconia, LSS - strontium doped $La_{10}Si_6O_{27}$, GDC - Gadolinium doped Ceria, LSGM - La $_{0.80}Sr_{0.20}Ga_{0.83}Mg_{0.17}O_{3-\delta}$, SNS - strontium sodium silicate[110, 128], BYO - bismuth yttrium oxide, BaTG-barium thorium gadolinia, ScSZ - scandia stabilized zirconia, CaSZ - calcium stabilized zirconia, LCA - lanthanum calcium alumina [1, 54, 112, 113, 135].

Fig. 1.3 shows that bismuth yttrium oxide (BYO) has one of the highest oxygen ion conductivity in the intermediate temperature range. Another material that should be noted in Fig. 1.3 is scandium stabilized zirconium (ScSZ) due to its high oxygen ion conductivity over the high-to-intermediate temperature range.

Bismuth oxides have an oxygen-deficient high temperature fluorite crystal structure called δ-Bi_2O_3. The oxygen-deficient structure allows for fast transfer of oxygen ions through the crystals via lattice hopping, leading to the high oxygen ion conductivity of BYO. The high temperature δ-Bi_2O_3 phase, while stable at >1073 K and meta-stable at room temperature, quickly degrades into a rhombohedral phase when subjected to temperatures between 873 K to 923 K, the temperature range usually

9

considered for intermediate temperature SOFC operation. The rhombohedral phase has a significantly lower oxygen ion conductivity than the δ-Bi_2O_3 phase, as seen by the change in the derivative of the oxygen ion conductivity at 1.13 K^{-1} in the BYO plot of Fig. 1.3.

Investigations into stabilizing the δ-Bi_2O_3 phase at these temperatures has shown that doping small amounts of ZrO_2, ThO_2, or CeO_2 (referred here as BYZ, BYT, and BYC, respectively) suppresses the degradation of the fluorite to rhombohedral structure [30, 53]. Huang *et. al* showed that as little as 5 mol% CeO_2 could stabilize the δ-Bi_2O_3 oxide structure for up to 300 hours at 873 K. They also showed that doping small amounts (less than 10 mol%) CeO_2 in has a negligible effect on the oxygen ion conductivity, essentially preserving the desired properties of BYO. While BYC5 (meaning 5 mol% CeO_2) has shown crystallographic thermal stability and high oxygen ion conductivity, it remains relatively unexplored. In fact, only a very narrow compositional region of the Bi_2O_3-Y_2O_3-CeO_2 phase diagram has been explored, still being constrained to the $(Bi_2O_3)_{0.75}(Y_2O_3)_{0.25}(CeO_2)_x$ psuedo-binary from Huang *et al.*'s previous study.

A material system that has received a substantial attention recently is ScSZ [87, 134, 136]. The mechanism for oxygen transport through ScSZ is the same as YSZ, where the addition of Sc stabilizes the cubic zirconia phase and provides interstitial sites that increase oxygen ion diffusion through the lattice [142]. ScSZ has significantly higher oxygen ion conductivity, as shown in Fig. 1.3. In fact at 1073 K, ScSZ has over twice the oxygen ion conductivity of YSZ [62]. Though the phase diagram for ScSZ is underdeveloped, the material has been shown to have a stable cubic phase from 9 mol% to 13 mol% Sc_2O_3 doping into ZrO_2, when the operating temperature is less than 1273 K [87, 134]. At temperatures above 1273 K, the highly oxygen ion conductive cubic phase degrades into a undesired rhombohedral phase [65]. This degradation is not an issue during intermediate temperature SOFC

10

operating temperatures (less than 1073 K), but may be an issue during the ceramic synthesis of ScSZ based SOFCs. During the ceramic synthesis method, the entire assembly may be exposed to temperatures in excess of 1273 K to densify the various oxides in the SOFC.

Another approach to increasing the performance of a SOFC electrolyte is to make the electrolyte layer of the SOFC thin (<500 nm). By decreasing the electrolyte thickness, there is a reduction in the constriction effect due to the very short diffusion pathways that exist for the oxygen ions. This reduction in the constriction effect lowers the oxygen ion resistance of the total fuel cell and increases the oxygen flux. Jiang studied the effect of different YSZ electrolyte thicknesses on the overall resistance [59]. Jiang determined an Arrhenius-type empirical relationship between the electrolyte thickness and temperature to the SOFC oxygen resistance and a linear linear relationship between the cell resistance and the electrolyte thickness. This trend has also been observed experimentally for ScSZ by Kosacki *et al.* and Zhang *et al.*. Both groups studied the oxygen ion conductivity from sol-gel thin films of ScSZ, and observed a ten-fold increase in the oxygen ion conductivity for 500 nm ScSZ thin-films when compared to bulk ScSZ [61, 145].

Though the traditional ceramic and spin coating methods of synthesizing are inexpensive, they cannot easily create electrolytes that are less than 1 μm without introducing small pinholes or cracks [71]. Due to this issue, research has been performed on synthesizing SOFC materials using alternative methods, such as physical vapor deposition (PVD), chemical vapor deposition (CVD), and solution synthesis techniques [130]. Some examples of such a studies are Yu *et. al* and Sillassen *et. al* investigations of on the performance of ScSZ and YSZ electrolytes that were synthesized via PVD techniques [107, 106, 142]. An alternative method that has been investigated is magnetron sputtering. Magnetron sputtering is a PVD technique that is used on the industrial scale to grow high quality thin films, such as semi-conductors

11

and magnetic media [7, 33, 116]. Furthermore, many different types of materials can be deposited via magnetron sputtering, including metals, oxide, sulfides, and nitrides. The capabilities of magnetron sputtering makes it an ideal candidate as an alternative synthesis technique for controllably depositing SOFC thin-films electrolyte materials, including YSZ, ScSZ, and BYC.

One potential issue with using magnetron sputtering is that, sputtering is an intrinsically high-energy process and can deposit undesired meta-stable high-temperature crystal phases [17]. This is especially a concern for many of the SOFC electrolyte material, where the desired crystal phase only forms and is stable under a very specific temperature window. This potential issue can be addressed through systemic investigations of the effect of the sputtering conditions, *i.e.* sputter gun power, sputter gun tilt, particle throw distance, deposition pressure, ect., on the deposited crystal phase of the material.

1.4 HIGH-THROUGHPUT EXPERIMENTATION

The advancement and exploration of the technologies described in subsections 1.2 and 1.3 have one key similarity; the search space of the number of variables that need to be optimized is very large. For BCs, the effect of composition, temperature, and cyclic heating all need to be fully probed to evaluate potential materials used for turbines. For Fe-Cr-Al oxidation resistant coating for nuclear cladding materials, the potential effects of the meta-stable deposition process, the initial composition of the alloy, and the effect of a large temperature spread need to be investigated prior to full scale evaluation. For ScSZ, little is known about the effect of thin-film processing and synthesis parameters, such as gun power, deposition temperature, oxygen concentration during deposition, and post-deposition annealing on the as-deposited phase from sputtering synthesis of the deposited thin-film electrolyte. Even less is known about BYC thin-films, where full investigations of the combined effect

of deposition parameters, sample processing, and composition are needed.

Using the traditional one-at-a-time method of materials is prohibitive due to the high dimensionality of the search spaces. The time needed to investigate such large search domains can be significantly shortened through the use of a high-throughput Materials Genome Initiative (MGI) based approaches. The Materials Genome Initiative is a government initiative with the goal of expediting materials deployment by a factor of two [83, 84]. In 2011, the National Science and Technology Council (NSTC) and the Office of Science and Technology Policy (OSTP) released Materials Genome Initiative for Global Competitiveness, which outlined the use of integrating computational tools, quicker and more efficient experimental design and measurements, and advanced data science technologies synergistically to expedite materials discovery [83]. This initiative has already been successfully used in the fields of theoretical materials using approaches such as density functional theory (DTF) and calculated phase diagrams (CALPHAD) [23]. To further realize the goals of the MGI, the theoretical-experimental loop must be closed, in which theory and experimental results are used in parallel to more efficiently discover, characterize, and optimize materials. Currently, this closed-loop process is limited by both the lack and availability of high quality experimental data.

A key methodology that has been proposed to generate the large amount of high quality materials data necessary to strengthen the computational aspirations of the MGI is high-throughput experimentation [37, 44, 84]. In the HTE approach, tens to hundreds of samples are synthesized in parallel, processed, and then rapidly characterized via either parallel or serial measurement techniques [72, 104]. This approach to materials exploration started being recognized as a powerful tool in 1995 [133]. Since that time, it has become part of the standard repertoire for both industrial and academic material identification and optimization [43, 48, 60, 95, 102].

HTE techniques have been applied to accelerate thin-film research through the use

13

of parallel synthesis and characterization techniques. In these studies factors, such as sample temperature and composition, are varied across a library. On common approach to creating a library is through the use of continuous-composition-spread (CCS) samples. CCS libraries are samples in which a continuous composition spread is deposited across a substrate, usually using a physical vapor deposition (PVD) technique such as magnetron sputtering. After the library is created; physical locations on the libraries are then correlated to the specific compositions at that location. After this correlation has been determined, the individual locations of the CCS are then characterized using either quick-serial or parallel techniques, allowing for the rapid exploration of the entire library. Due to the large amount of characterization data that is created during this process, automated data analysis algorithms are used. These algorithms usually rely on a combination of data visualization, clustering, and dimensional reduction based tools. HTE tools have significantly reduced the time spent on experiments and have been used explore important aspects of materials, such as composition, crystal phase, pre-processing, etc. [60, 63, 115]. For relatively simple characterization techniques, this type of parallel sample synthesis has been successfully used to create, characterize, and analyze up to 10^3 to 10^5 samples per day [49].

Previous HTE methods for the creation of CCS libraries to investigate substantial portions of the binary, ternary, and quaternary systems have been well documented in the literature [43, 143]. However, to this moment, there are a limited number methodologies for determining the high-temperature oxidation properties or SOFC crystal phase stability of HTE thin-films despite the importance of such materials to a host of energy applications. Furthermore, many of the previously established HTE methodologies only address one or two of the key factors of the MGI. Here, I will describe a novel HTE framework that incorporates all aspects of the MGI to accelerate materials research for high-temperature thin-film materials for energy

14

applications. The framework utilizes a combination of computational-guided combinatorial sample synthesis, high-throughput characterization techniques, and big-data machine-learning based analysis tools, as outlined in Fig. 1.4.
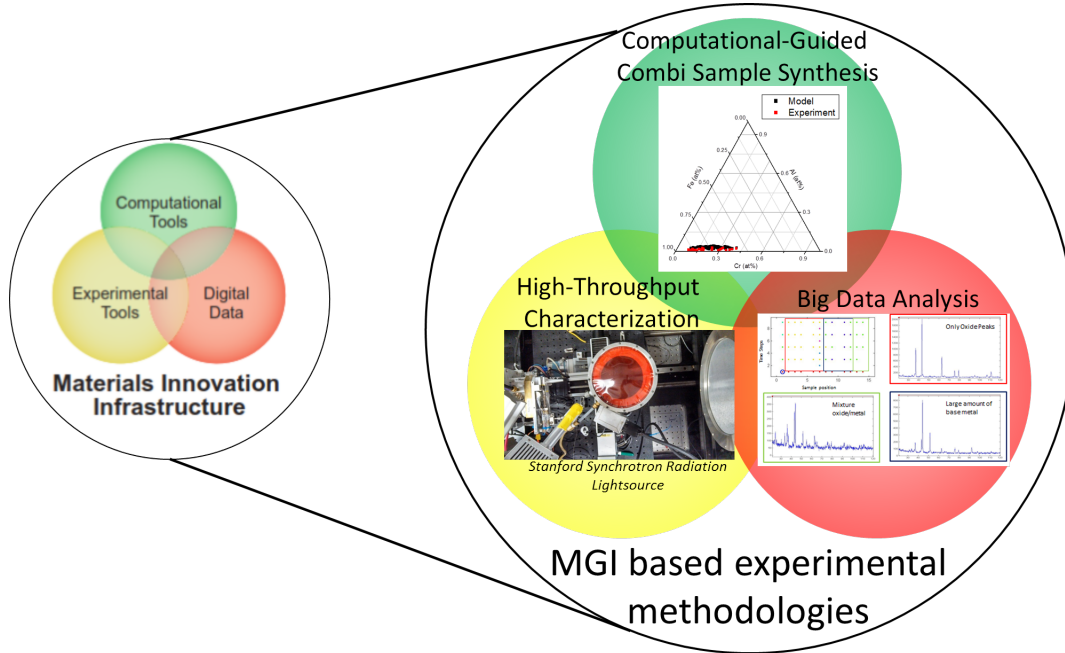
Figure 1.4 (Left) The general infrastructure proposed by MGI for an ideal materials exploration and development path. The infrastructure has a focus on, computational tools, experimental tools, and digital data [83]. (Right) A modified version of the MGI pictograph showing the major parts of the developed MGI based HTE framework. This framework addresses the three main topics by using computational-guided combinatorial sample synthesis, high-throughput characterization techniques, and big data analysis tools.

In Fig. 1.4, the main method of CCS library synthesis is magnetron sputtering. Sputtering is used to deposit a natural composition gradient across a sample. Details of the sputtering process and how it is used to create CCS libraries are given in section 2.1. One issue with sputtering is that there is no obvious relationship between sputtering conditions, like gun tilt, gun power, and throw distance on the composition/thickness that is deposited across a substrate. Traditionally, to deposit a desired composition spread, sputtering conditions are initially calibrated via a set of "calibration" depositions, and then optimized. In this process, a series of calibration

www.manaraa.com

samples are deposited by systemically changing sputtering parameters. The calibration samples are then characterized for thickness and composition using techniques such as: wavelength/energy dispersive spectroscopy (WDS/ EDS), profilometry, or atomic force microscopy (AFM) [16, 21, 78]. The calibration process time consuming, sometimes taking 2 weeks to properly determine an acceptable deposition recipe. An in-house semi-empirical sputter model was created to computationally-guided the sample synthesis process. This model is used to accelerate the process of determining the correct deposition recipe that will result in desired film composition. The details of the sputter model, optimization and validation are given in chapter 3.

Once CCS samples have been synthesized, they need to be characterized. Initially, the lack of reliable and rapid characterization tools was one of the major rate limiting steps for HTE approaches. Since the advent of HTE though, many sub-fields have developed rapid serial or parallel characterization techniques. The field of luminescent materials, magnetostrictive materials, shape memory alloys, and catalysis have all benefited from the advent of such characterization techniques [22, 43, 49, 133]. While these fields have all made great strides in the field of HTE, high-temperature thin-film materials has not received much attention. To overcome this obstacle, we have developed a complete HTE experimental framework that uses a mixture of high-temperature CCS library heating with *ex-situ* and *in-situ* 2D area x-ray diffraction (2D XRD) and Raman/Fluorescence analysis to evaluate the crystallographic dynamics of these materials. Details about 2D XRD, the instruments that were used to take 2D XRD, and how the results of these measurements were analyzed are given in section 2.2, and details about the combination of Raman/Fluorescence spectroscopy are given in section 2.3. To validate the proposed techniques, the well studied NiAl BC system was used. Details of the HTE approach to characterizing and probing thin-films for high-temperature applications are given in chapter 4.

Previously synthesis, processing, and characterization were the rate-limiting fac-

16

tors for HTE; this is no longer the case. Currently, due to the acceleration of sample synthesis and characterization, data-sets containing 100s-10000s of samples are created in relatively short time-scales. This generation of large data-sets has shifted the rate limiting step from sample synthesis and characterization to data analysis. Simplistic computational algorithms have been used in many fields, such as photocatalysis screening, to perform rapid analysis on large data sets. These simplistic approaches are not suited for more complex characterization techniques, such as XRD analysis or spectral analysis, where more complex methods of data analysis, such as peak identification and labeling, are needed. Analysis of such data sets is still performed by human experts who use variety of heuristics, such as peak location and peak shape to identify what potential crystals exist in each diffraction/spectral pattern. The complexity associated with this analysis has made it an open problem in the field that has been approached from many different potential solution pathways, such as machine learning [104]. Most of these solutions rely on the use of unsupervised clustering algorithms. In this approach, large data sets are grouped together based on a similarity metric, such as a 2-norm or a Pearson weighting coefficient [70]. While these techniques have shown great potential for reducing overall analysis time, they tend to mis-classify data sets in the presence of crystals dynamics or alloying, resulting in peak shift and peak shape change. Here, we created a semi-supervised algorithm, SS-AutoPhase, which uses a mixture of K-means clustering and a trained adaptive boosting (AdaBoost) classifier to accurately and automatically perform crystal identification analysis. The details of the general adaptive boosting classifier algorithm are given in sections 2.4. Details about the development, application, and validation of the SS-AutoPhase algorithm is given in chapter 5. The performance of SS-AutoPhase is based on a specialized set of metrics, explained in section 2.5.

The developed HTE methods were used to investigate oxidation resistant alloy Fe-Cr-Al as a nuclear fuel cladding material. Initially in this investigation, the effect

of composition of the alloy on oxide growth was determined at temperatures ranging from 556 K to 690 K. The results from this initial study were used to perform a more focused study on the long term oxidation behavior of select compositions of Fe-Cr-Al over time-scales relevant to nuclear reactor incidents. The details of this study are given in chapter 1. The HTE framework was also used to investigate the crystallographic stability of two solid oxide fuel cell electrolyte materials, ScSZ and BYC. The investigation of ScSZ used a 3^4 design of experiments to determine the effect of sputtering conditions and post deposition processing had on the stability and crystal structure. The effect of composition on the as-deposited crystal phase and crystallographic stability at 773 and 873 K of BYC was investigated. These SOFC electrolyte investigations are discussed in detail in chapter 7

CHAPTER 2

METHODS

In this chapter, the major techniques that were used in this work are outlined. First, a short description of the magnetron sputtering process and some of the fundamental mechanism behind sputtering will be discussed. Then, a description of the sputtering chamber used to create the thin-film libraries in this work will be described and how the natural composition gradient across these films were designed and created. After that, a description of the major characterization techniques, x-ray diffraction (XRD) and Raman spectroscopy will be explained and their application to each investigation in this work will be highlighted. Finally, the last sections will be dedicated to explaining two machine learning techniques, adaptive boosting (AdaBoost) and k-means clustering will be discussed and the general metrics by which classification algorithms are quantified will be explained.

2.1 MAGNETRON SPUTTERING

Principles

Magnetron sputtering is a physical vapor deposition technique (PVD) that has been employed in the industrial synthesis of microelectronics, low friction coating, corrosion-resistant coating, and optical materials. The sputtering process was discovered in the 1850s, when it was observed that cathodes in a electric gas discharge tube were being eroded [31, 39]. It was not until the 1940s, with the creation of the process of "diode" sputtering that the sputtering process was used industrially to create metallic

19

materials [114]. Thirty years later in the 1970s, a magnetically enhanced sputtering process, called magnetron sputtering, was developed [75, 127]. The development of magnetron sputtering, which has a much faster deposition rate than diode sputtering and causes less damage to the deposited film, greatly enhanced the use of sputtering as an industrial synthesis technique. In the 1990s, the application of radio frequency (RF) and pulsed direct current power sources for sputter sources overcame the classical issue of sputtering insulating materials, such as oxides, further expanding the use of sputtering in both academia and industry [100].

Sputtering chambers are ultra-high-vacuum (UHV) chambers that are comprised of two major pieces: a substrate/substrate holder and a sputtering source (also known as a sputter gun), as shown in Fig. 2.1 A). In modern sputtering chambers, the throw distance between the sputtering source and the substrate can be adjusted by moving the substrate holder closer or further from the source. The sputtering sources can also be tilted to adjust the direction and focus of the resulting sputtering plume during deposition.

A)

B)
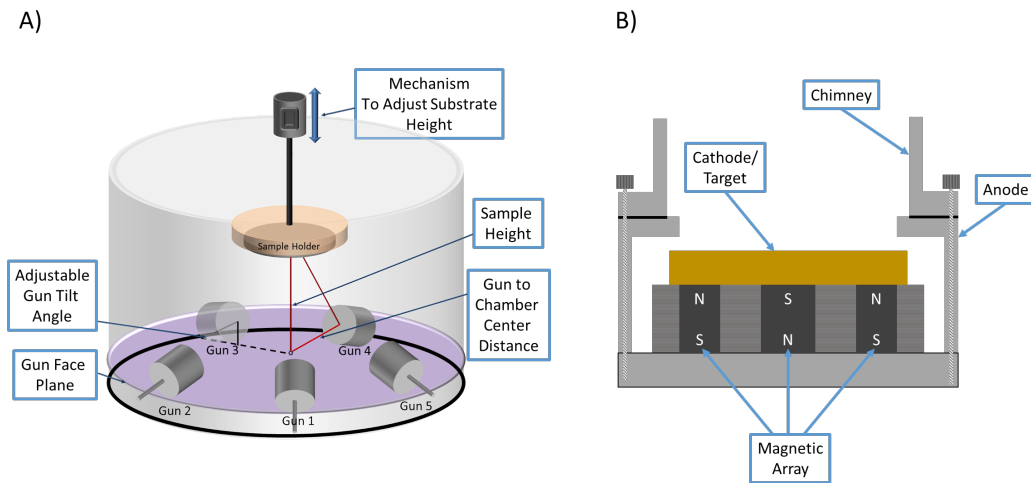
Figure 2.1   A) A schematic of the inside of a sputtering chamber that highlights the important pieces and dimensions of a sputtering chamber. B) A cross-section of a magnetron sputter gun that is equipped with a chimney.

Magnetron sputtering sources are comprised of four major pieces, an anode, a

20

cathode/target material, a magnetic array, and a chimney, as shown in Fig. 2.1 B). The chimney is optional, but is usually included on sputtering guns in modern systems, to reduce cross-contamination between multiple sputtering sources inside of a chamber. It does this by having a movable shutter attached to the chimney (not shown in Fig. 2.1) that can cover the target face while the gun is not sputtering, or expose the target face to allow for deposition on a substrate. The fundamental process of sputtering can be described as occurring in four steps, as shown in Fig. 2.2.

During the first step, the sputtering chamber is backfilled with sputtering gas, usually a noble gas such as argon. After the chamber has reached the desired sputtering pressure, the glow discharge is created out of the sputtering gas. This glow discharge is created by turning on a high voltage power supply that is connected to a cathode/target material placed on the source [125]. The power supply creates a strong electromagnetic field close to the face of the sputtering source. Once the neutral sputtering gas enters this field, it loses an electron, and becomes positively ionized and enters a plasma state. These plasma state sputtering gas ions (here referred to as sputtering ions) are accelerated towards the negatively charged cathode/target during the second step. These ions have large kinetic energies, typically ranging from the 10s-1000s of eV.

The third step occurs once a sputter ion collides with an atom of the target. When this collision occurs, two separate events occur. The first event is that the sputtering ion can collide with sufficient enough energy to cause secondary electron emission. The second event is that a collision cascade is induced inside of the target due to the collision between the sputtering ion and the target atom that it hit. During the collision cascade the atom that the sputtering ion initially hit moves into the surface of the target and collides with another atom. This atom then moves and collides with another atom, continuing the chain reaction of collisions. During this collision

21
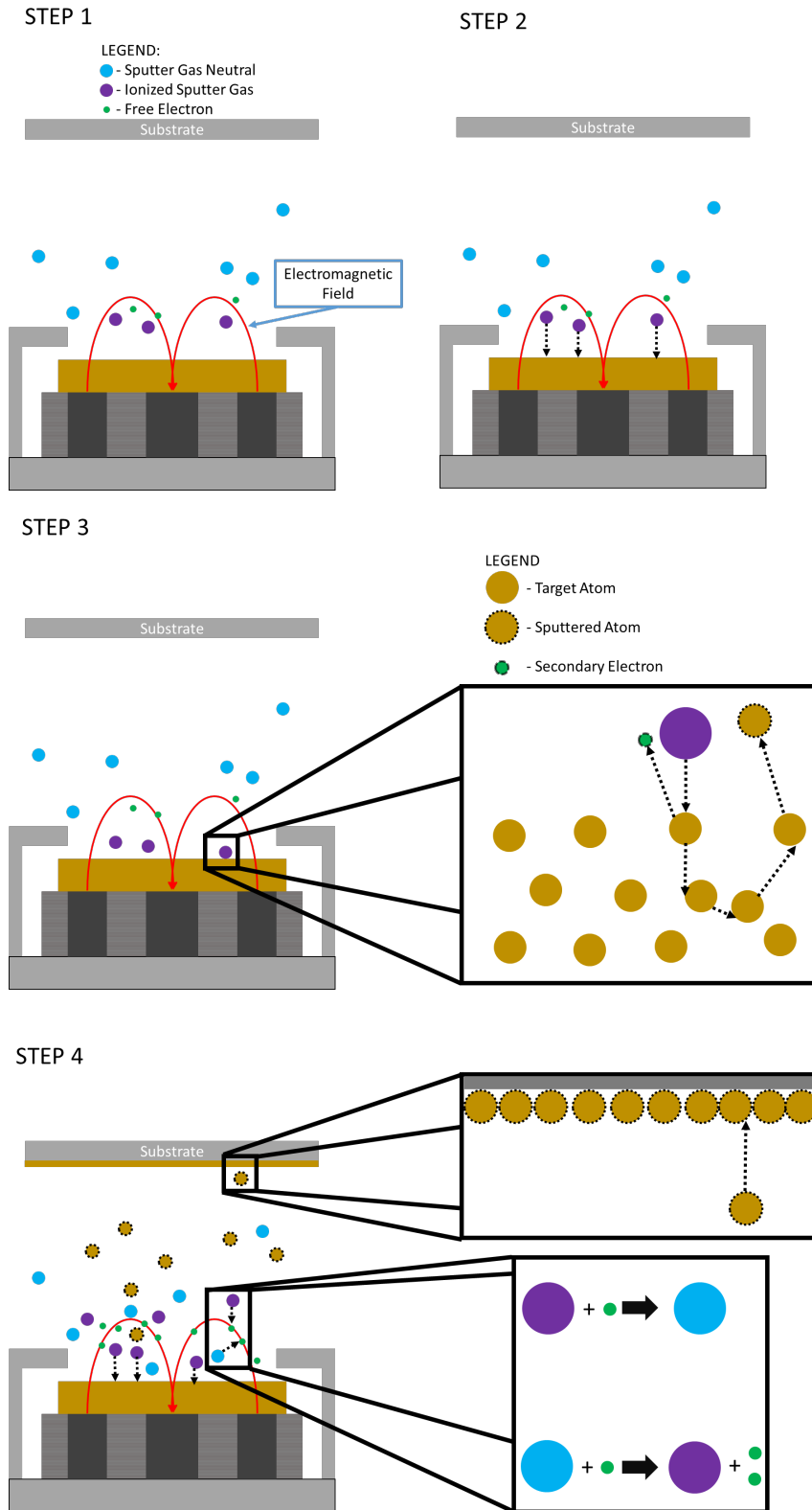
Figure 2.2   A pictorial representation outlining the general steps that occur during sputter deposition.

www.manaraa.com

cascade, it is possible for a target atom to be forced out of the surface of the target. This ejected atom is referred to as a sputtered atom. An example a collision cascade which results in a sputtered atom is shown on the right of Fig. 2.2 Step 3. It should be noted that only a small part of the total collision cascade in Fig. 2.2 is shown for clarity.

During the final steps of sputtering, two separate sets of events occur. The first step is the flight of the sputtered atom, show in the top inset of Fig. 2.2, Step 4. After the sputtered atom leaves the target, it continues its flight until it either collides with a gas atom in the chamber, another sputtered atom, or a surface. If the sputtered atom interacts with a surface, it will either deflect off the surface, knock an atom off the surface (in an event called resputtering), or it will deposit on the surface. It has been shown that for magnetron sputtering, the frequency of resputtering is very low compared to deposition frequency [38]. In this manner, a film of sputtered atoms will be deposited onto a surface, whether it be the sputtering chamber walls or a substrate. The second set of events focuses on the secondary electron that was emitted, and is shown in the bottom inset of Fig. 2.2 Step 4. After the secondary electron is emitted from the target surface, it becomes constrained in the electromagnetic field that is created by the magnetron. These electrons move throughout electromagnetic field until they escape and accelerate and collide with the anode, or they are hit by a sputter gas atom/ion. If the electron collides with a sputtering ion, it can recombine with the sputtering ion, neutralizing the ion to make a sputtering gas atom and a photon. If the electron collides with a sputter gas atom, it can knock an electron from the atom, creating an ion and another electron. This constant cycle of ion creation and elimination keeps the concentration of sputtering ions near the sputtering source approximately constant, yielding a constant deposition rate.
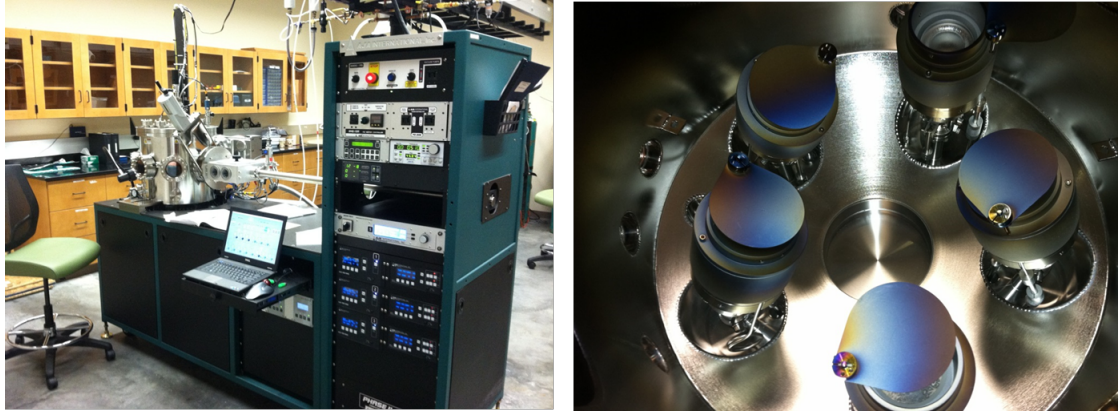
Figure 2.3   A picture of the 5-gun AJA Orion class sputtering chamber used in the current work to deposit thin-films. (Left) A picture of the outside of the sputtering chamber. (Right) A picture showing the 5-gun assembly.

Experimental Methodology

For the current work, a 5-gun AJA Orion class sputtering chamber was used for all depositions, as shown in Fig. 2.3. The guns of this chamber of equip with *in-situ* tilting capabilities, removable gas chimneys, and can be sputtered with an RF or DC power supply. The substrate holder has a an adjustable height, allowing for the average throw distance from the gun to the substrate to be controlled, and is attached to a radiation heater to allow for heating of the substrate during or after deposition. Prior to deposition, the chamber pressure is less than $6.6 * 10^{-6}$ Pa to reduce the concentration of latent containments from the air and from previous depositions.

Continuous-composition-spread thin-films can be produced in this chamber by co-depositing multiple target materials simultaneously, as shown in the theoretical ternary sample deposited in Fig. 2.4. The composition gradient of a CCS thin-film is measured by measuring the composition at multiple points on the substrate using methods such as wavelength/energy dispersive spectroscopy (WDS/ EDS) or x-ray fluorescence spectroscopy. The composition at each of these points can then be directly related from position on the sample to the composition of the thin-film.

24
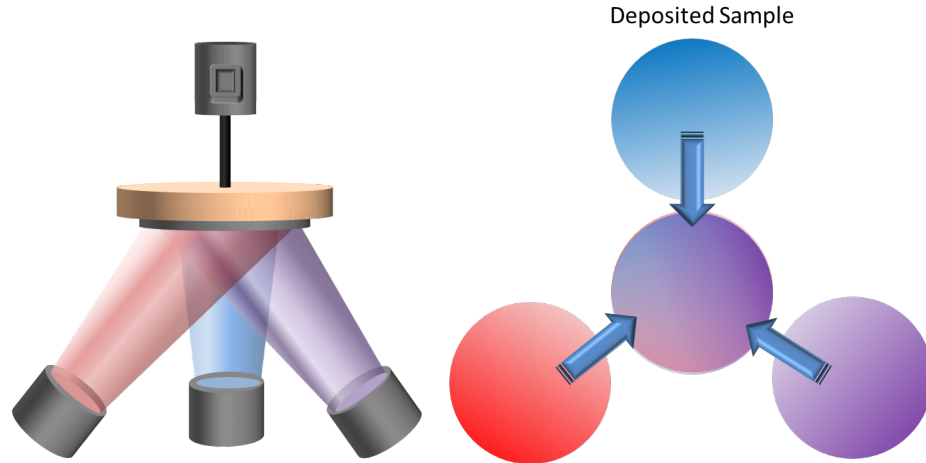
Figure 2.4 A pictorial representation showing how (left) three guns can be co-sputtered to created a (right) continuous-composition-spread thin-film.

While most of the investigations in this work utilized CCS thin-films, a single composition/thickness sample can be deposited with the current sputtering system by rotating the sample during deposition.

2.2 X-Ray Diffraction

Principles

Crystal phase identification was performed through the use of X-ray diffraction (XRD). XRD is an elastic scattering technique in which x-rays are directed toward a crystalline sample. The x-rays scatter primarily off of the electrons of the crystalline materials. The scattered x-rays cancel out in most directions due to destructive interference, but will create constructive interference at specific angles based on Bragg's law. Bragg's law states that diffracted x-rays will constructively interfere based on the following expression:

$$2 * d * \sin\left(\theta\right) = n * \lambda \tag{2.1}$$

25

where d is the spacing between the diffracting planes of the crystal, θ is the incident angle of the x-rays, n is any integer, and λ is the wavelength of the x-rays. Due to the fact that the diffraction phenomena is elastic, the angle that the x-rays diffract out of the crystal is equal to the angle that the diffracted x-rays will exit the crystal, as shown in Fig. 2.5.
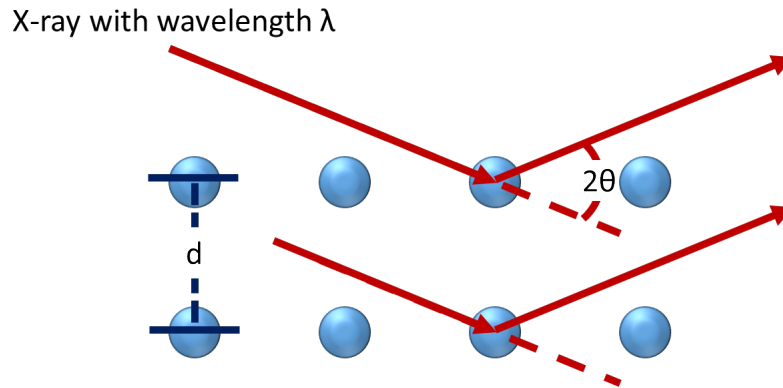
Figure 2.5   A pictorial representation of x-rays diffracting from a crystal.

The above equation can be directly applied to diffraction taken from diffractometers that utilize a θ-2θ geometry and a point detector. Alternatively, diffraction can be measured through the use of stationary 2D detectors. The use of a 2D detector, allows for measurement of diffracted x-rays at a range of θ values simultaneously as well as information about the diffraction in the χ direction, as shown in the top images of Fig. 2.6. The χ diffraction direction can analyzed to learn about the degree of texturing of a sample.

While 2D area detectors have the advantage of being able to rapidly obtain a diffraction response over a wide range of θ-χ, additional data processing is needed to transform the diffraction patterns into the traditional θ vs. intensity (here referred to as I) line plots [42]. An outline of the data processing is given in Fig. 2.6. The first step in this data processing is to convert the raw x-y-I detector image to a χ-θ-I diffraction pattern. This conversion step involves performing multiple

26
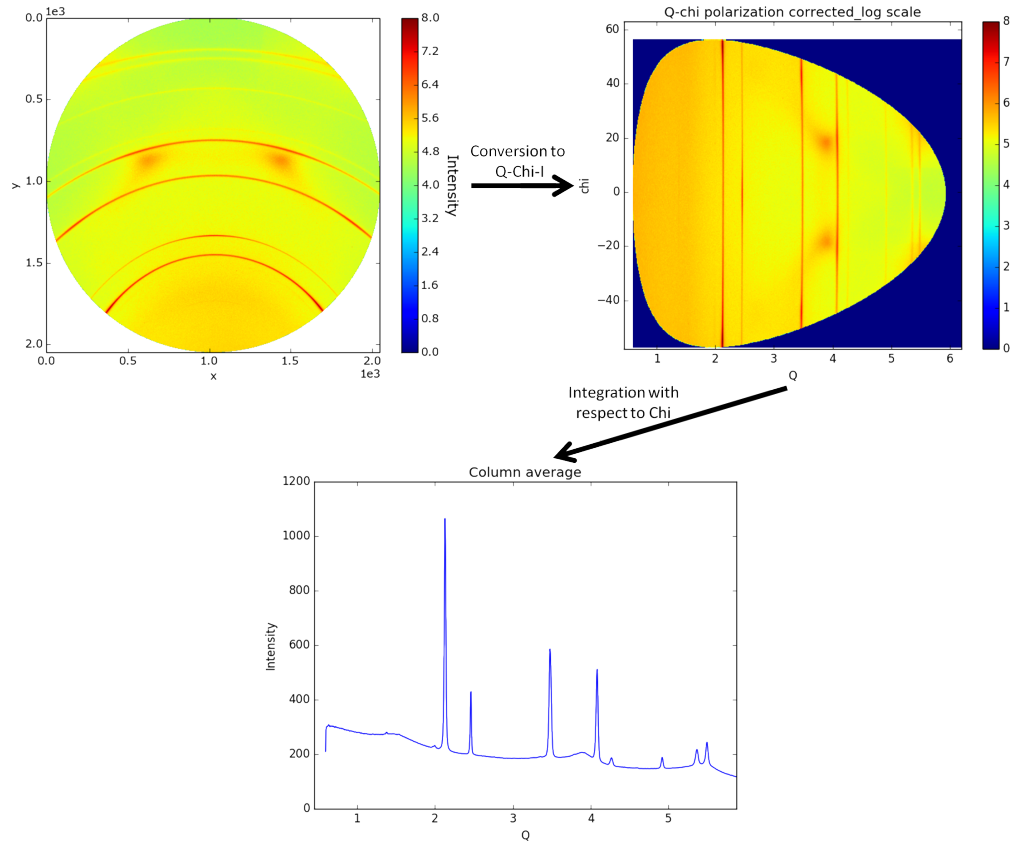
Figure 2.6 A general schematic of how to convert from the raw 2D area diffraction pattern (Top Left) to q-χ-I (Top Right). The q-χ-I plot can be integrated with respect to χ to generate the traditional q-I plot (Bottom)

geometric corrections which can be found in Ref. [46]. It should be noted that when performing this step, it is conventional to convert to χ-q-I instead of χ-θ-I. q describes the change in principal momentum vector of the diffracted x-ray, and are the basic unit of diffraction. q is related to θ by: n

$$q = 4 * \pi * \frac{\sin(\theta)}{\lambda} \tag{2.2}$$

Reporting in q has the additional advantage that the wavelength of the x-ray is not necessary for the information to be transfered, as the q that yields coherent diffraction does not depend on the wavelength of the x-ray but θ does. A traditional q-I diffraction line plot can generated from the be the χ-q-I plot by integrating with respect to χ. Due to the discrete nature of the positions on the 2D detector, this

27

integration is performed numerically. After this integration, the resulting diffraction pattern can be analyzed for peak location, peak intensity, and peak width.

Diffraction peak locations give information about what crystal phases exists in the material. Each crystal phase has a lattice and a set of crystal planes, which will yield diffraction peaks at a set of q location governed by Bragg's law. Once the location of the diffraction peaks have been identified, the peak locations can be compared to previously reported diffraction patterns in literature or in databases such as the Inorganic Crystal Structure Database (ICSD) [47]. An important aspect of this step is to identify potential crystal phases, based on the composition of elements in the sample, as the diffraction peak locations are not unique for each crystal phase. The fact that different crystals/crystal phases can have the same inter-atomic spacing, diffraction peaks are non-unique for a given crystal. Alloying, vacancies, and crystal stresses/strains all effect the diffraction peak location because these factors effect atomic spacing of the crystal lattice. These additional effects complications of uncertain peak location and potential peak aliasing (i.e. multiple crystal species having the same diffraction peaks) add complexity to XRD analysis.

Diffraction peak widths are quantified by the full-width at half-max (FWHM) of the peak. Diffraction peak widths are governed by many factors, including inhomogeneous defects in the crystal, temperature of the crystals, and crystal grain size [108]. Inhomogeneous defects in crystals can cause local variations in inter-atomic distances, which broadens the diffraction based on Bragg's law. The peak width is proportional to the temperature of the crystal, as the vibration of the atoms in a crystal increase with temperature. Similar to the local defects, this increase in atomic vibration effectively cause variations in inter-atomic distances when the x-rays diffract off the lattice. Peak broadening from crystallite size originates partially from imperfections at the grain boundaries of these crystals and a weakening of the assumption that a crystal is infinitely repeating when considering Bragg's law. For an unstrained crystal

28

with randomly oriented spherical grains, the peak broadening can be related to the grain size by Scherrer's equation [89]. Scherrer's equation states that:

$$\tau = \frac{K * \lambda}{\beta * \cos(\theta)} \tag{2.3}$$

Where τ is the mean size of the crystalline domains, K is a dimensionless shape factor for a given crystal shape, and β s the FWHM of a diffraction peak.

Peak intensities of each individual plane of crystals are governed by a mixture of parameters, such as the structure factor, plane multiplicity, and Lorentz factor, temperature, and the volume of a crystal plane that is scanned. For thin-film materials, texturing of the film can lead to the absence of diffraction peaks during a measurement due to the fact that the plane was not scanned during the measurement. The relative intensity of specific crystal planes is related to the amount of that plane that is scanned in the sample due to the relationship between the diffraction peak intensity and the volume of scanned crystal planes. The relative intensities of different species across a library can be analyzed to reveal qualitative changes in the amount of the different crystal structures across the library.

Experimental Methodology

In the current work, x-ray diffraction was performed either at beam line 1-5 of the Stanford Linear Accelerator Center (SLAC) or with a SAXSLAB Ganesha 200 XL small angle/wide angle diffraction system. Fig. 2.7 shows a labeled diagram of the SLAC diffraction assembly. Both the SLAC system and the SAXSLAB system are equip with 2D area detectors, shown on the right of Fig. 2.7, and an x-y stage. The x-y stage assembly of the SLAC sample stage is equipped with a substrate heater, allowing for *in-situ* heating of thin film samples during measurement. Additionally, an air-tight Kapton dome can be placed over the SLAC sample stage and gases can

29

be plumbed into the dome. This allows for controlled atmosphere studies during a diffraction experiment.
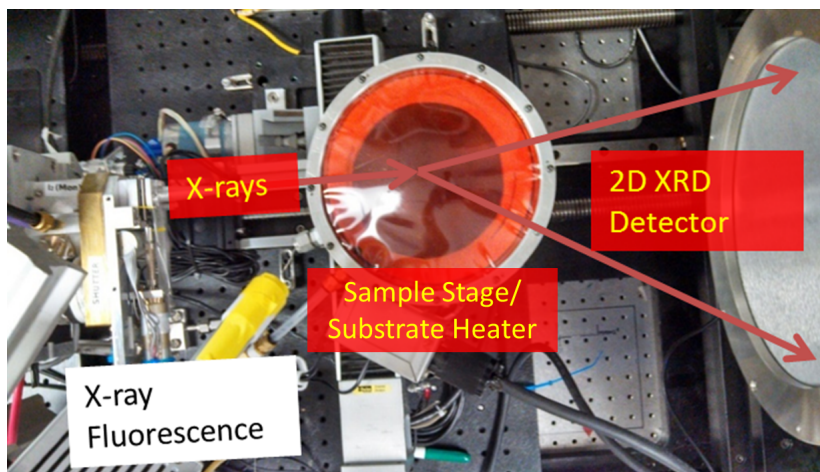
Figure 2.7   A top-view picture XRD assembly that was used at SLAC. The x-ray source is positioned to the left of the image. The x-rays from the source collide with the sample on the sample stage, then the diffracted x-rays are measured by the 2D area detector, shown on the right of the image.

The x-y stage, the stage that the sample is placed on in Fig. 2.7 was used to move the sample and perform crystallographic screening across CCS library samples. The ability to move the sample between each XRD measurement significantly reduced diffraction allocation time by minimizing sample handling and allowed for accurate sampling meshes across CCS library samples. The incidence angle of the beam can be adjusted by changing the tilt of the sample holder with respect to the x-ray source.

2.3   RAMAN SPECTROSCOPY AND FLUORESCENCE SPECTROSCOPY

Principles

Raman spectroscopy is an inelastic scattering technique that provides information relating to the chemical and structural state of a material. During a typical Raman spectroscopy measurement, a sample is illuminated with monochromatic light, usually

www.manaraa.com

from a laser. The photons of the light cause a collective excitation of the vibrations of atoms or of the electron's spin in a crystal lattice, called phonon excitation or magnon excitation, respectively. These excited states, called virtual energy state, are not stable, and so a phonon or magnon relaxation occurs, releasing a photon. During this relaxation, the crystal lattice does not have to relax back to the original energy state, causing the released photon to be of lower or higher energy than the original light used to induce the excitation, called Stokes and anti-Stokes scattering, respectively [40]. Fig. 2.8 shows an energy diagram, with an of the excitation/relaxation from Stokes and an anti-Stokes scattering. The change in the energy state between the light used to cause the phonon/magnon excitation is called Raman shift of the light. The shift in the energy of the incoming light depends on the bond type, bond symmetry, electronic environment, and crystal structure of the specific probed material. Due to the specificity of these energetic excitations in relation to the chemical and bonding structure of species, Raman can be used to "finger-print" the compounds of a sample. For a species to be Raman active, the polarizability of the chemical bonds must change during bond vibration.
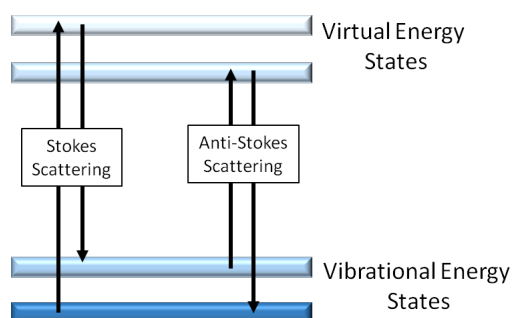
Figure 2.8   A pictorial representation of Stokes and Anti-Stokes scattering. During Stokes scattering (Left) a vibrational state is excited to a higher virtual energy state, and upon relaxation, returns to a higher vibrational energy state than the initial state. During Anti-Stokes scattering (right) a vibrational state is excited to a higher virtual energy state, and upon relaxation, returns to a lower vibrational energy state than the initial state

Fluorescence is also an inelastic scattering phenomena where light is emitted from

www.manaraa.com

a sample due to electron excitation and relaxation by a specific energy of light. It can be measured in a similar manner to Raman spectroscopy, where a monochromatic light is exposed to a material and the energy of the light emitted by the material is measured. The energy of the incoming light is absorbed by the material, which excites an electron in the material to a higher electronic energy state. From this excited state, the electron will relax back to its original energy state either directly or indirectly by passing through intermediate energy states. If the electron relaxes directly, a photon with the same energy as the photon used to excite the material will be released. Indirect relaxation occurs when the electron first undergoes a quantized transition to an intermediate energy state, such as transitioning to a state with a different spin mutliplicity. When the electron then relax back to its initial energy state, the released photon will be of different energy then the original excitation light [56]. A Jablonski diagram showing both a direct and an indirect relaxation is shown in Fig. 2.9. For a material to fluoresce in the described manner, the energy of the incoming light has to be equivalent to the electronic band gap of the probed material. The combination of what wavelength of light that for electron excitation and the quantized pathways for indirect relaxation to occur is material specific. Like Raman spectroscopy, this specificity can be used to identify the presence of specific materials. Unlike Raman spectroscopy, the excitation of a material only occurs when using a specific wavelength of light.

Experimental Methodology

In the current work, Raman spectroscopy and fluorescence were measured simultaneously during the oxidation resistance coating studies (see chapters 4 and 6). During these studies Raman was used to identify the presence of various oxides, such as NiO, Fe_2O_3, and Fe_3O_4, and fluorescence was used to identify the presence of specifically θ- and α-Al_2O_3. While florescence is traditionally measured through the use of
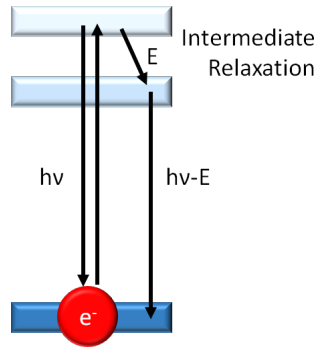
Figure 2.9   A pictorial representation of the energy states of an electron that undergoes a direct or indirect relaxation during a fluorescence event.

techniques such as excitation-emission matrix spectroscopy (EEMS), such techniques were not needed as all other oxides except θ- and α-Al_2O_3 have strong Raman active responses. Instead, to shorten materials characterization time, these two responses were measured simultaneously by selecting the wavelength of light (632.8 nm red laser) used by the Raman spectrometer to cause fluorescence of α-Al_2O_3 if it was present. In the study of NiAl bond coats, a 441.6 nm blue laser was also used to ensure that the Al_2O_3 was not obscuring the Raman signal of the oxides. All of these measurements were taken with a Horiba Olympus spectroscopy system using a 50X objective lense and a spot size of 1.03 μm. The system was equipped with both the red and blue laser, which can easily be switched between measurements.

2.4   Adaptive Boosting (AdaBoost) Classification

AdaBoost is an ensemble supervised machine learning algorithm that was first proposed by Yoav Freund and Robert Schapire [29]. A supervised machine learning algorithm is one in which a set of training data, i.e. data analyzed by a human expert, is used to train an the algorithm to emulate the data analysis of the human expert. In the case of HTE x-ray diffraction analysis, this means that a subset of diffraction data from an HTE diffraction study is analyzed by a human expert. The

33

human "label", identifies and documents, the existence/non-existence of each crystal phase in the diffraction patterns. The supervised algorithms then analyzes the labeled data and adapts its method of analysis to maximize the agreement between the human labeled patterns with the algorithmically predicted labels. The exact method of adaptation is different for each supervised classification algorithm.

The AdaBoost feature selection and classification algorithm combines a set of weak classifiers into a strong classifier by taking a weighted sum of all of the weak classifiers' predictions. These weak classifiers are other classification algorithms, such as decision trees in current work, that have been individually trained on different features of the data, i.e. the intensity of a diffraction pattern at a specific 2θ or d location. Once each of these weak classifiers have been trained; AdaBoost provides each weak classifier with a weight that represents the relative importance of the weak classifiers. Most commonly, the initial weights given to each weak classifier is the same, so that no specific learner is more important than any other. Then for each data set, the weak classifiers all perform independent analysis of the data to decide what the identity of the data set is based on their previous training. If a weak classifier identifies that a data set should be given a specific label, then the weight associated with that weak classifier is assigned to be positive; otherwise the weight associated with the classifier is assigned to be negative. AdaBoost then takes a sum of all the weights. If the overall sum is positive, AdaBoost assigns the data set with the specific label; otherwise it does not assign the specific label. This process can be seen as:

$$
C = \begin{cases} 1 & \text{; if } \sum_i \omega_i \geq 0 \\ 0 & \text{; if } \sum_i \omega_i < 0 \end{cases} \tag{2.4}
$$

Where C is the overall classification from the AdaBoost classifier amd ω_i is the weight of the ith weak learner. If $C = 1$, the specific label is assigned, otherwise it is not. AdaBoost then uses a greedy optimization procedure on the absolute value of

34

the weights associated with each weak classifier to maximize the agreement between the human labeled patterns and the AdaBoost predicted labels. Once the AdaBoost classifier has been trained, it can be used to predict the identity of unlabeled data.

2.5 Classification Algorithm Metrics

Receiver operating characteristics (ROCs) are a set of metrics that give insight into the performance of binary classification systems. While these ROC metrics were first used during World War II to assist in the analysis of radar; they have been successfully adapted to describe the expected performance of classification algorithms. To use these metrics; an algorithmic classification is performed on a set of data that has been labeled and the results are tabulated through the use of a confusion matrix. An general confusion matrix is given in Table 2.1.

Table 2.1 A general confusion matrix from a classification problem. In this matrix S_P and S_N sample population that are labeled as positive and negative, respectively. I_P and I_N are also known as Type I and Type II errors respectively.

	Predicted Positive	Predicted Negative	Total
Identified Positive	True Positive (C_P)	False Positive (I_P)	S_P
Identified Negative	False Negative (I_N)	True Negative (C_N)	S_N

The results from a confusion matrix can be used to calculate ROC metrics. Three ROC metrics that are used in the current work are true positive rate (R_{TP}), true negative rate (R_{TN}), and accuracy (R_{Ac}). These metrics can be calculated via:

$$R_{TP} = \frac{C_P}{S_P} \tag{2.5}$$

$$R_{NP} = \frac{C_N}{S_N} \tag{2.6}$$

$$R_{Ac} = \frac{C_P + C_N}{S_{total}} = \frac{C_P + C_N}{S_P + S_N} \tag{2.7}$$

The true negative and true positive rates represent the confidence one can have in any given prediction of a dataset is predicted with a negative and positive label. The accuracy represents the percentage of datasets that were labeled correctly. The reason that all three of these metrics are used is to more aptly describe dataset that are biased, having a majority of positive labeled data and a minority of negative labeled data or vice-versa. If a dataset is extremely biased, the accuracy of a classifier can be inflated, as can be see by analyzing the results of the confusion matrix in Table 2.2.

Table 2.2   An example of a confusion matrix from a classification problem with 100 reference data sets. In this matrix, the reference data sets are positively biased. Due to this bias, the overall accuracy of the classification is 90%, but the classification algorithm did not identify a single negative data set correctly.

	Predicted Positive	Predicted Negative	Total
Identified Positive	90	0	90
Identified Negative	10	0	10

The accuracy Table 2.2 is 90%, but the true negative rate is 0%. This shows that even though the accuracy seems high, the classification algorithm was not able to correctly distinguish between datasets that should be labeled with a positive and a negative.

As shown, due to the binary nature of the metrics; the labels of the dataset must be limited to "positive" and "negative". The physical meaning of what a "positive" or "negative" label represents does not matter for the calculation of the metrics. If more than two categories exist in the dataset then a method for finding a meaningful binary representation has to be determined. An example of how to overcome this issue can be shown by the current work. In the current work, multiple crystal phases were identified by the AutoPhase algorithm, as will be discussed in chapter 5. During these studies, each crystal phase was labeled and predicted as existing ("positive" label) or not existing ("negative" label) in a specific xrd patterns. Using this labeling

36

system for the multiple category problem overcame the issue of binary representations and allowed for application of ROC metrics.

Chapter 3

Semi-Empirical Sputter Model

3.1 Model Development

Motivation and Experimental

As stated in chapter 1, one of the major rate limiting steps for thin-film synthesis via sputtering for HTE is the initial calibration of the composition spread for each sputtered material. The issue of understanding and modeling different aspects of the sputtering deposition plume has been a research focus of many previous studies. One of the first modeling studied in this field was by Sigmund, who developed a mathematic treatment to determine the sputtering yield. The sputtering yield is a dimensionless number that relates the number of atoms that are sputtered from a target per incident sputter-gas ion impinging into the target [105]. In the 1980s, Matsunami furthered Sigmund's original calculations to more properly describe the sputtering yield for low energy and light-ion sputtering by accounting for the effects of the threshold energy [74]. This work lead to Yamamura's development of a differential form of the angular distribution of the sputtering yield, also known as

---

Parts of chapter adapted from: J. K. Bunn, C. J. Metting, and J. R. Hattrick-Simpers, (2015). A Semi-Empirical Model for Tilted-Gun Planer Magnetron Sputtering Accounting for Chimney Shadowing. JOM, 67(1), 154-163, with permission from Springer. See Fig. C.1 for copyright permission.

Parts of chapter adapted from: J. K. Bunn, R. Z. Voepel, Z. Wang, E. P. Gatzke, J. A. Lauterbach, and J. R. Hattrick-Simpers, (2016). Development of an Optimization Procedure for Magnetron-Sputtered Thin Films to Facilitate Combinatorial Materials Research. Industrial and Engineering Chemistry Research, 55(5), 1236-1242, with permission from the American Chemical Society. See Fig. C.2 for copyright permission.

the differential angular sputtering yield [137, 139]. These advancements have been used as the basis for many other developments, including MC/MD modeling of the target, particle thermalization predictions, resputter modeling at the substrate, and deposition modeling for specific sputtering geometries [36, 38, 76, 120, 138].

While all of these predictive models have advanced the understanding of the sputtering process, the main focus of the field has been the prediction of sputtering yields. The calculation of the sputtering yields by itself does lead to predictions of film thickness/composition. Such a prediction would not only need calculations of sputtering yields, but would also need to account for geometric effects of the chamber, such as relative placement of the guns and substrate, tilting of the guns, and possible shadowing effects. The theoretical and geometric constraints of previous treatments have hindered their application to modern sputtering systems, especially for chambers with off-center, tilted-gun geometries. Here a semi-empirical model that can predict film thickness distributions and take into account materials sputtered from an off-centered, tilted, and chimneyed sputtering gun assemblies will be described and validated [13].

The model utilizes Yamamura's formalism for the differential angular distribution and an assumption of a straight-line particle path to predict the relative concentration of particles within a deposition plume at the surface of the substrate. The straight line path of sputtering particles is additionally used to determine the effect of shadowing by gun chimneys used in modern sputtering; allowing for a more accurate description of the relative concentration of particles in the plume. The relative particle concentration is then converted to absolute concentration through the use of an experimentally obtained calibration curve (deposition rate versus power curve) at a single chamber geometry. The developed model uses these three principles and a single calibration curve to predict deposition profiles from a wide range of gun-tilts, chimney assemblies, chamber geometries, target materials, and deposition powers. Validation of the

39

model was performed by measuring DC sputtered copper deposition rates at varying gun-tilts and chimney sizes with a crystal monitor and comparing the experimental deposition rates with predicted deposition rates from the model. To understand how the chimney geometry was changed between depositions, it is important to know that the chimney of the sputtering gun was comprised of two pieces, a ground shield and a gas chimney. When just the ground shield was installed, the experiments will be referred to as "short chimney" and when both the ground shield and the gas chimney were installed, the experiments will be referred to as "tall chimney".

Prior to the validation depositions, the base pressure of the system was less than 7.0 e-8 Torr. The depositions were carried out under 30 sccm of argon (99.9999% purity) at a pressure of 5.0 mTorr at ambient temperature. Initially, the target was pre-sputtered for 10 minutes before any measurements were made to remove residual oxide and organics from the target surface. Two sets of experiments were carried out during the validation. The first set was carried out from 50 W to 200 W with gun-tilts between 17.7° to 31.3° from vertical with the tall chimney. Then, the same sputtering powers were used to sputter copper from gun-tilts varying from 0° to 31.3° with the short chimney. During each deposition the DC voltage of the gun was recorded and an Inficon SQM-160 crystal monitor was used to measure deposition rates. The reported values from the crystal monitor were verified previously with an Alpha Step 200 profilometer from Tencor Instruments. A summary of all experimental results are shown in the Table A.1 in section A.1 of the appendix.

Theory

During the sputtering process, particles travel away from the target in all directions. A description of the angular distribution of sputtered particles per incident ion, S, was given by Yamamura[139] as:

40

$$S(E, \theta, \theta_1) = 0.042 \frac{\alpha(M_2/M_1, \theta)S_n(E)}{U_s} cos(\theta_1) \times \left[1 - \frac{1}{2} (E_{th}/E)^{\frac{1}{2}} \left\{ cos(\theta)\gamma(\theta_1) + \right. \right.$$
$$\left. \left. \frac{3}{4}\pi sin(\theta)sin(\theta_1)cos(\phi) \right\} \right] \quad (3.1)$$

Where E is the energy of the incidence ion, θ_1 is the projection angle of the particle from the target surface normal, α is a dimensionless function of both the ratio of the molecular weights of the sputter gas material, M_1 to the target material, M_2, and the incidence angle θ, S_n is the nuclear stopping power per atom, U_s is the surface binding energy per atom of the target material, E_{th} is the threshold energy. E_{th} can be empirically related to U_s [74, 101, 137]. $\gamma(\theta_1)$ is the function:

$$\gamma(\theta_1) = \frac{3sin^2(\theta_1) - 1}{sin^2(\theta_1)} + \frac{cos^2(\theta_1)\left[3sin^2(\theta_1) + 1\right]}{2sin^3(\theta_1)} \times ln\left(\frac{1 + sin(\theta_1)}{1 - sin(\theta_1)}\right) \quad (3.2)$$

If the incidence angle of the sputter gas is assumed to be normal to the target surface, $\theta = 0$, then Eqn. (3.1) can be approximated as:

$$S(E, 0, \theta_1) = 0.042 \frac{\alpha(M_2/M_1)S_n(E)}{U_s} cos(\theta_1)$$
$$\times \left[1 - \frac{1}{2} (E_{th}/E)^{\frac{1}{2}} \left\{ 1 + \frac{5}{3}cos^2(\theta_1) \right\} \right] \quad (3.3)$$

To calculate the total dimensionless atomic flux from the target that reaches a point on the substrate, $\mathfrak{S}$, two separate assumptions are made. These assumptions are that the particles follow a straight-line path and the target face is sputtered uniformly. A discussion and defense of the validity of the straight-line path assumption is given in section A.2 of the appendix. An examination of the uniform sputtering assumption will be discussed later in this section. With these two assumptions, $\mathfrak{S}$ can be calculated by integrating $S(E, \theta, \theta_1)$ over the solid angle between the surface of the target subtended to a point on the substrate, Ω. This is shown by:

$$\mathfrak{S}(E, \theta_1) = \Psi S_n(E) \int \Xi(E, 0, \theta_1) d\Omega \tag{3.4}$$

$$\Psi = 0.042 \frac{\alpha(M_2/M_1)}{U_s} \tag{3.5}$$

$$\Xi(E, \theta_1) = cos(\theta_1) \left[1 - \frac{1}{2}(E_{th}/E)^{\frac{1}{2}} \left\{ 1 + \frac{5}{3} cos^2(\theta_1) \right\} \right] \tag{3.6}$$

Where Ψ and $\Xi(E, \theta_1)$ are non-integral and integral dependent pieces of Eqn. (3.3), respectively. Ψ can be taken out of the integral because it is independent of θ_1, and is only dependent on the material properties of the sputtering gas and the target material.

Before integrating Eqn. (3.4) a frame rotation transformation of the sputtering geometry is performed to simplify the integration of Eqn. (3.4) and to ensure that the solid angle calculation will be the same for different gun-tilts. This transformation consists of rotating the gun-substrate frame by $90° - \omega$, where ω is the tilt angle of the gun in degrees. After the rotation, the coordinate system is aligned to the gun face as opposed to the plane of the substrate, as shown in Fig. 3.1. After the frame rotation was performed, the transformed values for the vertical distance between the target and substrate , Z_T, and the horizontal distance between the center of the target to the center of the gun, ρ_T°, were determined.

After this transformation, equation 3.4 is expressed as:

$$\mathfrak{S}(E, \rho) = \Psi S_n(E) \int_{\rho^{min}}^{\rho^{max}} \int_{\phi^{min}(\rho)}^{\phi^{max}(\rho)} \left(\Xi(E, \rho) \times \frac{Z_T \rho}{(\rho^2 + Z_T^2)^{3/2}} \right) d\phi d\rho \tag{3.7}$$

Where ρ^{min} and ρ^{max} are the minimum and maximum ρ values of the target from a given point on the substrate, respectively, and $\phi^{min}(\rho)$ and $\phi^{max}(\rho)$ are the minimum and maximum angles on the target for a given ρ, respectively. In Eqn. (3.7), the variable θ_1 from $S(E, \theta_1)$ and $\Xi(E, \theta_1)$ in Eqn. (3.4) were transformed into a function of ρ because Yamamura's original formulism of the dimensionless atomic flux was written in spherical coordinates and Eqn. (3.7) is written in cylindrical coordinates.

42
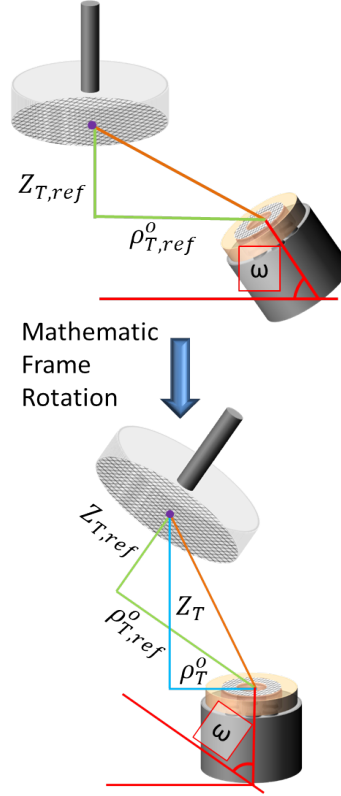
Figure 3.1 (Top) The substrate-gun geometry arrangement before the frame correction. (Bottom) The substrate-gun geometric arrangement after the frame correction. ω is the gun-tilt angle from the vertical, $Z_{T,ref}$ and Z_T are the vertical length between a substrate point and target before and after the frame correction, respectively, and $\rho_{T,ref}^\circ$ and ρ_T° are the horizontal length between a substrate point and the center of the target before and after the frame correction, respectively.

Eqn. (3.7) can be simplified by using the symmetry of the target to change the ϕ limits of integration. The integration over ϕ can be carried out without further analysis because none of the parameters in the integral depend on ϕ. This integration yields:

$$\mathfrak{S}(E,\rho) = 2\Psi S_n(E) \int_{\rho^{min}}^{\rho^{max}} \left(\Xi(E,\rho)\phi^{max}(\rho) \times \frac{Z_T\rho}{(\rho^2 + Z_T^2)^{3/2}} \right) d\rho \qquad (3.8)$$

Expressions for ρ^{min}, ρ^{max}, and $\phi^{max}(\rho)$ depend on the geometry of the sputtering area of the target and how the target is shadowed by the chimney. Eqn. (3.8) can be rewritten in a general form:

$$\mathfrak{S}(E,\rho) = 2\Psi S_n(E) \int_{\rho^{min}}^{\rho^{max}} \Xi(E,\rho)\phi^{max}(\rho)F(\rho)d\rho \qquad (3.9)$$

Where $F(\rho)$ replaced the final term in Eqn. (3.8). This expression is valid for the case where a target is sputtered uniformly, but this is not the case during magnetron sputtering. For the case of magnetron sputtering, the geometry of the underlying magnetron cause sputtering targets to exhibit a circular "racetrack" shaped erosion ring [66]. A set of two concentric circles whose origins are at $(\rho_T^\circ, 0, Z_T)$ can be used to approximate the same of the racetrack. The inner circle has a radius $R_{T,In}$ and outer circle has a radius, $R_{T,Out}$. It is assumed here that the area between $R_{T,In}$ and $R_{T,Out}$ is uniformly sputtered, and that all other regions of the target do not sputter. The racetrack geometry alters Eqn. (3.9), since the center area of the racetrack does not contribute to the dimensionless flux of the sputtered atoms. This approximation is accounted for by the following equation:

$$\mathfrak{S}(E,\rho) = 2\Psi S_n(E)\Bigg(\int_{\rho_{Out}^{min}}^{\rho_{Out}^{max}} \Xi(E,\rho)\phi_{T,Out}^{max}(\rho)F(\rho)d\rho$$
$$- \int_{\rho_{In}^{min}}^{\rho_{In}^{max}} \Xi(E,\rho)\phi_{T,In}^{max}(\rho)F(\rho)d\rho \Bigg) \quad (3.10)$$

In Eqn. (3.10), the first integral term accounts for the dimensionless flux coming from the entire target without considering the non-sputtered inner region (NSIR) the second integral term is a correction term that accounts for the NSIR. The maximum ϕ value is defined by the intersection of the target outline and a line of constant ρ on the surface of the target and can be found by solving the equation for a circle.

To find an expression describing the shape of the shadow cast from a circular chimney, it is assumed that particles do not deposit onto the substrate if the chimney wall intercepts the straight-line path from the target to the substrate.

From the chimney geometry shown in Fig. 3.2, the shape of the shadow as observed from any point on the substrate on the plane of the target is a circle with

44

radius R_S and origin ρ_S°. The geometry of the gun and the chimney can be used to define ρ_S° and R_S:

$$\rho_S^\circ = \Psi \rho_T^\circ \tag{3.11}$$

$$R_S = \Psi R_C \tag{3.12}$$

$$\Psi = \frac{L_C}{Z_C} + 1 \tag{3.13}$$

$$Z_C = Z_T - L_C \tag{3.14}$$

Where Ψ is defined by Eqn. (3.13) and is a factor that accounts for the projection
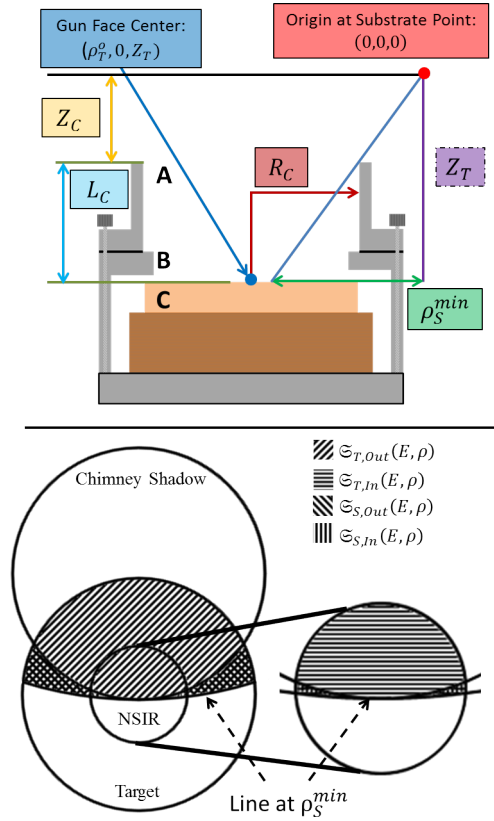
Figure 3.2 (Top) The substrate-gun assembly configuration. (A) represents a removable gas chimney on the gun, (B) represents the ground shield on the gun, and (C) represents the target. (Bottom) A 2-D projection in the $\rho - \phi$ plane of the substrate-gun assembly geometry with the chimney shadow. The bottom left and the bottom right image highlight the physical area that each of the flux variables for Eqns. (3.16) and (3.17) account for, respectively.

45

of the chimney on the target surface , R_C is the chimney radius, L_C is the chimney length, and Z_C and Z_T are the z-values of the top of the chimney and the target respectively. A new formulation of Eqn. (3.10) is needed to account for shadow coverage of the inner and outer areas of the target racetrack. For any given point on the substrate, the area of the target not shadowed by the chimney is contained within the circle-shaped shadow projected onto the target, so that $\mathfrak{S}$ takes the form of:

$$\mathfrak{S}(E,\rho) = \begin{cases} 0 & ; \rho^2 - 2\rho\rho_S^o cos(\phi) + (\rho_S^o)^2 \geq (R_S)^2 \\ \mathfrak{S}_{Out}(E,\rho) - \mathfrak{S}_{In}(E,\rho) & ; \rho^2 - 2\rho\rho_S^o cos(\phi) + (\rho_S^o)^2 < (R_S)^2 \end{cases} \quad (3.15)$$

Where $\mathfrak{S}_{Out}(E,\rho)$ is the dimensionless flux coming from the non-shadowed portion without considering the NSIR and $\mathfrak{S}_{In}(E,\rho)$ corrects for effect of the non-shadowed NSIR. $\mathfrak{S}_{Out}(E,\rho)$ and $\mathfrak{S}_{In}(E,\rho)$ are determined by:

$$\mathfrak{S}_{Out}(E,\rho) = \mathfrak{S}_{T,Out}(E,\rho) - \mathfrak{S}_{S,Out}(E,\rho) \quad (3.16)$$

$$\mathfrak{S}_{In}(E,\rho) = \mathfrak{S}_{T,In}(E,\rho) - \mathfrak{S}_{S,In}(E,\rho) \quad (3.17)$$

Where $\mathfrak{S}_{S,Out}(E,\rho)$ and $\mathfrak{S}_{S,In}(E,\rho)$ are correction terms that account for the fluxes from the entire shadowed region of the target in the absence of the NSIR and the shadowed NSIR of the target, respectively, and $\mathfrak{S}_{T,Out}(E,\rho)$ and $\mathfrak{S}_{T,In}(E,\rho)$ are the first and second integrals in Eqn. (3.10), respectively. The physical area of target that these four flux variables account for is shown in Fig 3.2. The specific form of the parameters for Eqns. (3.16) and (3.17) depends on the degree to which the target is shadowed by the chimney. These different degrees of shadowing will be referred to as chimney shadowing cases. There are many chimney shadowing cases that may occur. Fig. 3.3 illustrates the applicable cases for this study.

Depending on the chamber, target, and chimney geometry there are multiple possible shadowing cases. For the situation where $R_S \geq R_{T,Out}$, which is true for the
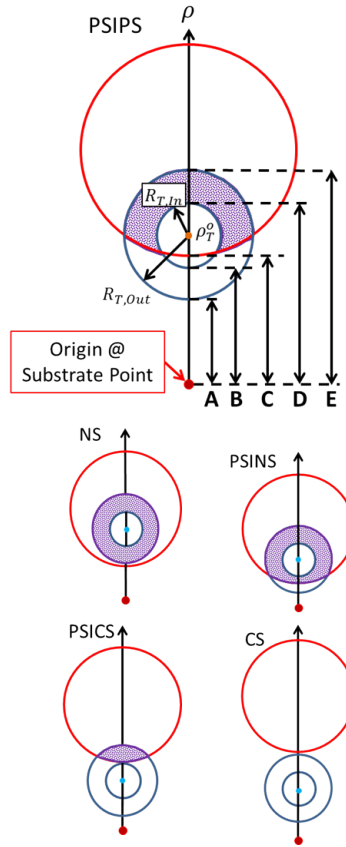
Figure 3.3   A 2-D projection in the $\rho - \phi$ plane of the substrate-gun assembly geometry. Each diagram represents a different shadowing situation. In the top figure (A), (B), and (C) represent $\rho_{T,Out}^{min}$, $\rho_{T,In}^{min}$, and ρ_S^{min} respectively, which are the minimum in-plane ρ lengths between the substrate point and the corresponding feature, and (D) and (E) represent $\rho_{T,In}^{max}$ and $\rho_{T,Out}^{max}$ respectively, which are the maximum in-plane ρ lengths between the substrate point and the corresponding feature.

deposition environment used in this work, only five different shadowing cases will exists. These cases are highlighted in Fig. 3.3 and Table 3.1. The shadowing case for a specific point on a substrate is determined by comparing the minimum ρ-value of the non-shadowed portion of the target, ρ_S^{min}, to the minimum and maximum ρ values of the inner and outer regions of the target, $\rho_{T,In}^{min}$, $\rho_{T,In}^{max}$, $\rho_{T,Out}^{min}$ and $\rho_{T,Out}^{max}$, respectively as shown in Table 3.1. If substrate point projected onto the Z_T plane does not fall within the area of the target, which is always true for the current sputtering geometry,

47

the minimum and maximum ρ values are defined by:

$$\rho_S^{min} = \rho_S^{\circ} - R_S \tag{3.18}$$

$$\rho_{T,i}^{min} = \rho_T^{\circ} - R_{T,i} \tag{3.19}$$

$$\rho_{T,i}^{max} = \rho_T^{\circ} + R_{T,i} \tag{3.20}$$

Where the subscripted i in Eqns. (3.19) and (3.20) represents either the inner or outer region of the target.

Table 3.1 A list of the different types of chimney shadowing that can occur in the current study, and the relevant ranges of ρ_S^{min} that each case is applicable.

Gun Shadowing Type	Abbreviation	Applicable Region
No shadowing	NS	$\rho_S^{min} \leq \rho_{T,Out}^{min}$
Partial shadowing: Inner racetrack not shadowed	PSINS	$\rho_{T,Out}^{min} < \rho_S^{min} \leq \rho_{T,In}^{min}$
Partial shadowing: Inner racetrack partially shadowed	PSIPS	$\rho_{T,In}^{min} < \rho_S^{min} \leq \rho_{T,In}^{max}$
Partial shadowing: Inner racetrack completely shadowed	PSICS	$\rho_{T,In}^{max} < \rho_S^{min} \leq \rho_{T,Out}^{max}$
Complete shadowing	CS	$\rho_{T,Out}^{max} \leq \rho_S^{min}$

Fig. 3.3 shows that the lower ϕ limits of $\mathfrak{S}_{S,Out}(E,\rho)$ and $\mathfrak{S}_{S,In}(E,\rho)$ are not $0°$, unlike the lower ϕ limit of the not shadowed flux equations, but are described by the region between ϕ_S^{max} and the corresponding maximum target ϕ value. To account for this, the term ϕ_S^q is used in place of ϕ^{max} in the expressions of $\mathfrak{S}_{S,Out}(E,\rho)$ and $\mathfrak{S}_{S,In}(E,\rho)$, as shown below:

$$\phi_{S,i}^q(\rho) = \phi_{T,i}^{max}(\rho) - \phi_S^{max}(\rho) \tag{3.21}$$

$$\mathfrak{S}_{S,i}(E,\rho) = 2\Psi S_n(E) \int_{\rho_{S,i}^{min}}^{\rho_{S,i}^{max}} \Xi(E,\rho)\phi_{S,i}^q(\rho)F(\rho)d\rho \tag{3.22}$$

48

Where the the subscripted i in Eqns. 3.21 and 3.22 represents either the inner or outer region of the target, and the ρ limits of integration; $\rho_{S,Out}^{min}$, $\rho_{S,Out}^{max}$, $\rho_{S,In}^{min}$, and $\rho_{S,In}^{max}$ depend on the shadowing case. $\mathfrak{S}(E,\rho)$ for each gun shadowing geometry can be determined by evaluating the parameters in Eqn. (3.22) for both the inner and outer regions of the target. Once the appropriate form of $\mathfrak{S}(E,\rho)$ is found, the total dimensionless atomic flux from the target to a point on the substrate can be evaluated by integrating the general flux equation given below:

$$
\begin{aligned}
\mathfrak{S}(E,\rho) = 2\Psi S_n(E)\bigg(&\int_{\rho_{T,Out}^{min}}^{\rho_{T,Out}^{max}} \Xi(E,\rho)\phi_{T,Out}^{max}(\rho)F(\rho)d\rho \\
&- \int_{\rho_{S,Out}^{min}}^{\rho_{S,Out}^{max}} \Xi(E,\rho)\phi_{S,Out}^{q}(\rho)F(\rho)d\rho - \int_{\rho_{T,In}^{min}}^{\rho_{T,In}^{max}} \Xi(E,\rho)\phi_{T,In}^{max}(\rho)F(\rho)d\rho \\
&+ \int_{\rho_{S,In}^{min}}^{\rho_{S,In}^{max}} \Xi(E,\rho)\phi_{S,In}^{q}(\rho)F(\rho)d\rho \bigg) \quad (3.23)
\end{aligned}
$$

Table 3.2 below gives expression for the ρ limits of integration given in Eqn. (3.23) for each shadowing case.

Table 3.2   The expressions for the ρ limits of integration used in Eqn. (3.23) for each shadowing case. When a field contains NA the corresponding integral in Eqn. (3.23) that the specific field applies to is equal to 0.

	NS	PSINS	PSIPS	PSICS	CS
$\rho_{T,Out}^{min}$	$\rho_T^\circ - R_{T,Out}$		$\rho_S^\circ - R_S$		NA
$\rho_{T,Out}^{max}$		$\rho_T^\circ + R_{T,Out}$			NA
$\rho_{S,Out}^{min}$	NA		$\rho_S^\circ - R_S$		NA
$\rho_{S,Out}^{max}$	NA		Eqn. (3.24), $i = Out^*$		NA
$\rho_{T,In}^{min}$	$\rho_T^\circ - R_{T,In}$		$\rho_S^\circ - R_S$	NA	NA
$\rho_{T,In}^{max}$		$\rho_T^\circ + R_{T,In}$		NA	NA
$\rho_{S,In}^{min}$	NA	NA	$\rho_S^\circ - R_S$	NA	NA
$\rho_{S,In}^{max}$	NA	NA	Eqn. (3.24), $i = In^*$	NA	NA

49

For the * expressions in Table 3.2, the following equation is used:

$$\rho_{S,i}^{max} = \sqrt{\frac{\left[(\rho_T^\circ)^2 - (R_{T,i})^2\right]\rho_S^\circ - \left[(\rho_S^\circ)^2 - (R_S)^2\right]\rho_T^\circ}{\rho_T^\circ - \rho_S^\circ}} \qquad (3.24)$$

Where i is the index shown in Table 3.2.

The dimensionless atomic deposition rate, $\mathfrak{S}(E, \rho)$, can be converted to a real atomic deposition rate for any point in the chamber by taking a reference deposition rate at a given position in the chamber with a specific gun tilt and power. This can be achieved by determining the ratio of an experimentally measured atomic flux at a point on the substrate, $\mathfrak{F}_{exp}$, to the calculated $\mathfrak{S}(E, \rho)$ at the same point under identical experimental conditions, $\mathfrak{S}_{exp}(E, \rho)$. That quantity is then set equal to the ratio of the predicted atomic flux at any point on the substrate under a desired experimental condition, $\mathfrak{F}_{pred}$, and the corresponding calculated $\mathfrak{S}_{pred}(E, \rho)$. This equality is represented by:

$$\frac{\mathfrak{F}_{exp}}{\mathfrak{S}_{exp}(E, \rho)} = \frac{\mathfrak{F}_{pred}}{\mathfrak{S}_{pred}(E, \rho)} \qquad (3.25)$$

Eqn. (3.25) can be altered to consider the thickness or atomic deposition rates rather than the atomic fluxes if it is advantageous to do so. In this study, a crystal monitor was used to measure deposition rates at a given point in the sputtering chamber for Cu deposited by a DC power source with various gun powers. The crystal monitor measures the average thickness over the entire sensor area which can then be converted into a thickness deposition rate, Υ. The real atomic flux rates in Eqn. (3.25) can be converted to Υ by using the molecular weight and density of the target material and assuming that the surface area of the measurements and the calculations are infinitely small in the $\rho - \phi$ plane. In this fashion, Eqn. (3.25) can be used to determine Υ_{pred} at any point on the substrate given Υ_{exp}. Eqn. (3.25) can then be written as:

50

$$\Upsilon_{pred} = \frac{\Upsilon_{exp} \mathfrak{S}_{pred}(E, \rho)}{\mathfrak{S}_{exp}(E, \rho)} \tag{3.26}$$

For a chimney with multiple pieces that contribute to the shadowing effect, such as the chimney in this study, Υ_{pred} can be approximated by calculating $\mathfrak{S}_{pred}(E, \rho)$ and $\mathfrak{S}_{exp}(E, \rho)$ with the R_C and L_C of each chimney piece, as shown in Fig. 3.2, and accepting the lowest value of $\mathfrak{S}_{pred}(E, \rho)$ and $\mathfrak{S}_{exp}(E, \rho)$. This process can be shown as:

$$\mathfrak{S}^i_{exp}(E, \rho) = [\mathfrak{S}_{exp}(E, \rho)]_{R_C=R_C^i; L_C=L_C^i} \tag{3.27}$$

$$\mathfrak{S}^i_{pred}(E, \rho) = [\mathfrak{S}_{pred}(E, \rho)]_{R_C=R_C^i; L_C=L_C^i} \tag{3.28}$$

$$\mathfrak{S}_{exp}(E, \rho) = \min\left(\mathfrak{S}^i_{exp}(E, \rho)\right) \tag{3.29}$$

$$\mathfrak{S}_{pred}(E, \rho) = \min\left(\mathfrak{S}^i_{pred}(E, \rho)\right) \tag{3.30}$$

Where i represents each chimney piece. This analysis assumes that the shadowed area of the target can be approximated by a single chimney piece. The approximation is valid for the current study because a single chimney piece will cast the majority or entirety of the shadow.

Results And Discussion

Model validation was performed by comparing the experimentally measured deposition rates with multiple model predictions. Before model calculations were performed, the inner and outer racetrack radii were measured. During this measurement it was observed that evidence of deposition in the inner-most region of the target existed, even though racetrack profile varied in depth along the radius, with a clear maximum near the gun-magnet cluster. The results of this measurement were that, $R_{T,In}$ and $R_{T,Out}$ of the Cu target were 0 cm and 2.2 cm, respectively. With an inner radius of 0 cm only the NS, PSICS, and CS cases for the model.

51

To ensure that accounting for chimney shadowing would significantly improve model performance, predictions that did and did not correct for chimney shadowing were performed, as shown in Figs. 3.4 and 3.5, respectively. The modeled data were produced by taking each experimental measurement of Υ_{exp} at a given power, chimney geometry, and gun-tilt and then calculating Υ_{pred} at all other gun-tilts using the same power and chimney geometry as the experimental reference. To determine the error of the calculation as well as an ideal gun tilt for calibrations in future studies, this process was repeated for each experimental result. Relative errors were calculated and compared for all test cases. A prediction that did not account for chimney shadowing was performed with the 50 W tall chimney data. The predictions accounting for chimney shadowing made using 50 W and 150 W data are shown in Fig. 3.5, and the data for the 100 W and 200 W are contained within section A.3 of the appendix. The correlation between the predicted and experimental angular dependence of the sputtering deposition rate was found by taking the absolute values of the relative errors (magnitude of the relative error) and calculating the average relative error for all predictions.
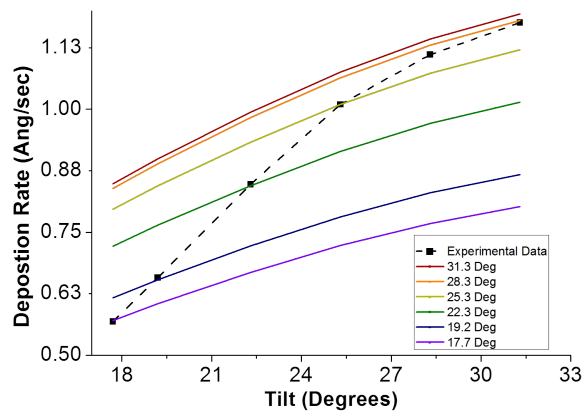
Figure 3.4   The experimental (black points) and predicted deposition rates (lines) over the entire gun-tilt range for tall chimney data for the 50 W experimental data. These prediction were made without accounting for chimney shadowing.

Fig. 3.4 shows that the deposition rate prediction that did not consider chimney

www.manaraa.com

shadowing was only in high agreement with the 50 W tall chimney experimentally measured deposition rates at the calibration point. The average magnitude of the relative error of the prediction was 11.78% ± 9.42% and the maximum magnitude of the relative error was 31.80%. This indicates that a model that does not consider chimney shadowing will not accurately predict the deposition rates for guns with a chimney installed.
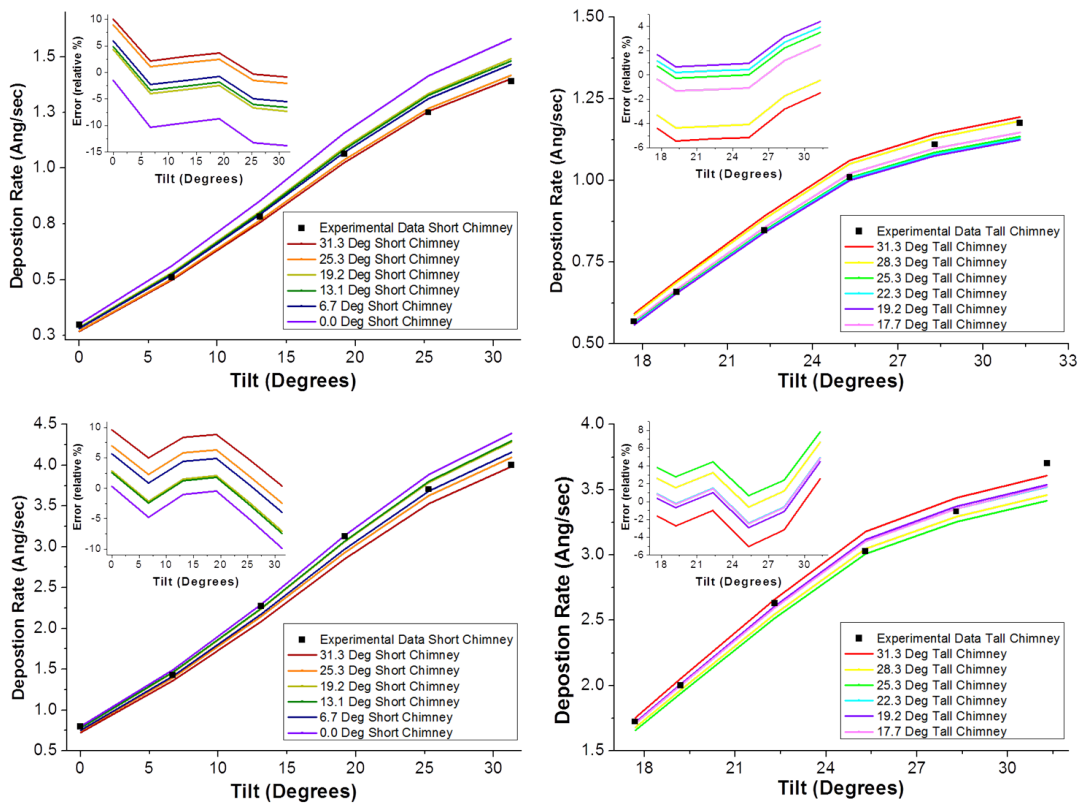
Figure 3.5 The experimental (black points) and predicted deposition rates (lines) over the entire gun-tilt range for the short (Left) and tall (Right) chimney data for the 50 W (Top) and 150 W (Bottom) model predictions. The inset plot is the relative error of the each model prediction. Each data set uses a different reference gun tilt. The figure shows that the models using a gun-tilt of 19.2° give the most accurate results when compared to the experimental data.

Model predictions that accounted for chimney shadowing were performed, and are shown in Fig. 3.5. The predictions were calculated to have an average magnitude of the relative error of 4.14% ± 3.02% for a 0° to 31.3° gun tilt range without the gas

53

chimney and $2.12\% \pm 1.71\%$ for a 17.7° to 31.3° gun tilt range with the gas chimney. To check the worst case scenario of the model, a maximum error analysis was also performed.

The maximum relative error of all models was 13.8% for the calibration taken at 50 W at a gun-tilt of 0° for the short chimney model. The other short chimney models had maximum relative errors between 5.90% to 10.02% for the full tilt range and maximum relative errors between 5.46% to 8.89% for the tilt range that was investigated with the tall chimney models. The tall chimney models had maximum relative errors between 4.48% to 7.80%. This analysis shows that both the short and tall chimney models exhibited similar maximum errors over their common range (31.3° to 17.7°).

The lowest relative error as a function of the gun-tilt range is observed at a gun-tilt of 19.2° for both the short and tall chimneys. For this gun-tilt the maximum relative error is 7.28% over the entire range of tilts and powers. Therefore, predictions for subsequent experiments using an initial tilt of 19.2° should be more accurate.

As stated, the model that did not consider chimney shadowing, shown in Fig. 3.4, had an average relative error of $11.78\% \pm 9.42\%$ and the maximum relative error of 31.80%, while the models that did consider chimney shadowing had an average relative error of $2.15\% \pm 1.71\%$ and the maximum relative error of 5.42%. This shows that by accounting for chimney shadowing, the average accuracy of the prediction improves by 5.47 times and that the maximum relative error decreases by 5.87 times the prediction that does not account for chimney shadowing. This analysis indicates that accounting for chimney shadowing is an important aspect of these model and can significantly improve the predictive capabilities when guns are installed with chimneys. Due to the non-linear nature of the model equations, relative errors of the predictions can be highly sensitive to the accuracy of the measurements used to define the system geometry. A complete input sensitivity analysis was performed, and is given in section

A.4 of the appendix.

3.2   Sputter Parameter Optimization

Motivation and Experimental

In the previous section, a semi-empirical model that accurately predicts the deposition rate from sputtered materials was developed and validated [13]. While the model was successful at computing the deposition rate of materials given specific deposition conditions, the true purpose of the model is to solve the reverse problem. Ideally, the model would assist in the determination of deposition conditions to create a desired composition/thickness spread. One approach to attaining such a goal would be to reorganize the model equations to directly predict sputtering conditions for a given deposition rate spread if it was possible to do so. Currently, there is no clear pathway to perform such a rearrangement because of the non-linear nature of the model equations. Another solution would be to implement an optimization procedure of the sputtering conditions. This solution is viable due to the relatively short calculation time of the model (usually less than 1 sec per model). Implementing such a optimization procedure would reduce the time and effort of determining experimental sputtering conditions.

To implement such a procedure, the specific variable that are to be optimized, the optimization method, and an appropriate objective function were determined, as outlined in section 3.2. A 2-tier validation of the optimization using experimentally measured thickness spreads from a sputtered copper gun was performed. Finally, the associated response surfaces of the model were analyzed. This analysis is important, so that obstacles such as existence of multiple local minima could be identified and proper methods of handling these obstacles could be implemented, and further validation was performed [9].

The performance of the optimization procedure was validated by using measured thickness profiles from three DC sputtered copper thin-films on 7.62 cm circular Si wafers. Table 3.3 shows the sputter conditions for each of these thin-films. After deposition, profilometer measurements of the thickness of the films were taken at 24 points across the wafer. These thickness measurements were then converted to deposition rates by dividing them by the deposition time. After the deposition rates were determined, they were used in the 2-tier validation of the optimization procedure.

Table 3.3   The experimental conditions used to sputter the Cu films to validate the optimization procedure. In the last two rows c^{min} and c^{max} show the minimum and maximum allowable value for the parameter of the corresponding column. *The gun tilts are stated with respect to the vertical direction between the sputter gun face and the substrate.

	Deposition Pressure (Pa)	Sputter Gun Power (W)	Sputter Gun Tilt (Degrees)*	Sputter Gun to Substrate (mm)	Deposition Time (sec)
Condition 1	0.667	75	62.0	101	2177
Condition 2	0.667	70	62.0	111	2188
Condition 3	0.933	100	59.0	101	1424
c^{min}	NA	25	52.4	81	NA
c^{max}	NA	500	88.0	121	NA

The first evaluation tested the performance of the optimization procedure against simulated deposition rate spreads. The goal of this evaluation was to compare the optimization results to an idealized case, where effects from model error and measurement uncertainty would not bias the results. In this evaluation, the measured deposition rates were used to calibrate the sputter model. The calibrated model was then used to predict the deposition rates across a 7.62 cm circular wafer. The optimization procedure was then used to determine sputtering conditions that would yield the simulated results without being given any information about the deposition conditions used to simulate the film. The resulting optimization predicted deposition conditions were compared to the experimental conditions.

The second evaluation method used the optimization procedure to identify the deposition condition directly from the experimentally measured deposition-rate spreads. The general procedure for this evaluation is exactly the same as the first evaluation method, expect the experimentally measured deposition-rate spreads were used instead of a modeled spread. In this evaluation, model errors as well as non-idealities of the experimentally measured deposition rate, such as noise in the measurements, are present in the desired spread. The effects of such factors render perfect agreement between the experimentally deposition rate distribution and the predicted distribution from the optimization unlikely. This evaluation tests the ability and sensitivity of the algorithm to determine sputtering conditions for non-ideal deposition rate distributions. The details and results of this 2nd validation are given in section A.5 of the appendix. This validation was left out of this chapter because the 2nd validation was only used to test the sensitivity of the optimization to potential measurements errors, and does not assist in the validation of the optimization procedure.

A full analysis of the results and performance of the optimization for experimental condition 1 will be given in section 3.2, and analysis of conditions 2 and 3 are in ref. [9].

Theory

A Nelder-Mead optimization routine was implemented [85]. Nelder-Mead was chosen due to it is a derivative-free optimization technique that performs well for multi-dimensional optimization. This routine was used to determine the sputter-gun tilt, gun power, and distance between the sputter gun and substrate, referred to here as the substrate height, for the deposition of a desired thickness gradient of copper. These three parameters were chosen to be optimized because they are the commonly changed experimentally to tune the deposition rate spread across samples. Copper was chosen because is it a well studied system, and because it was the material used

57

to validate the sputter model, as shown in section 3.1. The objective function for the optimization was the Frobenius-norm between the desired deposition rates, $T_{desired}$, and the predicted deposition rates, $T_{predicted}$. For the calculation of the objective function, the deposition rates were used to populate matrices. With these matrices, objective function was calculated as:

$$O\left(p,t,h\right) = ||T_{desired} - T_{predicted}\left(p,t,h\right)||_F \tag{3.31}$$

Where $O\left(p,t,h\right)$ is the objective function evaluated at the gun power, p, gun tilt, t, and substrate height, h. Soft constraints, through the use of penalty functions, were added to the calculation of the objective function to account for physical constraints of the deposition parameters. The resulting soft-constraints objective function, $O_{constrained}\left(p,t,h\right)$ was calculated with:

$$O_{constrained}\left(p,t,h\right) = O\left(p,t,h\right) + P\left(p\right) + P\left(t\right) + P\left(h\right) \tag{3.32}$$

Where $P\left(p\right)$, $P\left(t\right)$, and $P\left(h\right)$ are the penalty functions associated with the gun power, gun tilt and substrate height, respectively. The general form of the penalty function for a sputtering variable c was be calculated by:

$$P\left(c\right) = \begin{cases} 0 & ; \text{ if } c^{min} \leq c \leq c^{max} \\ \sqrt{\left(c^{min} - c\right)^2} & ; \text{ if } c < c^{min} \\ \sqrt{\left(c^{max} - c\right)^2} & ; \text{ if } c^{max} < c \end{cases} \tag{3.33}$$

Where c^{min} and c^{max} are the minimum and maximum allowable value of the sputtering variable c.

Analysis of Response Surface Plots

The input response surfaces were evaluated to identify potential obstacles that could exists during optimization. Fig. 3.6 shows an example response plot which was

58

used during this analysis. As shown in Fig. 3.6 B)-D), 2 dimensional sections of the 3 dimensional contour plots were used to simplify analysis and to overcome data presentation issues. During this analysis, multiple local minima were observed with respect to the sputter-gun tilt versus substrate height, shown in the bottom right corner of Fig. 3.6 D). Furthermore, the gradient of the objective function around the minimum becomes very small in all of the response plots. These two issues could lead the optimization procedure to terminate at non-optimal solutions.
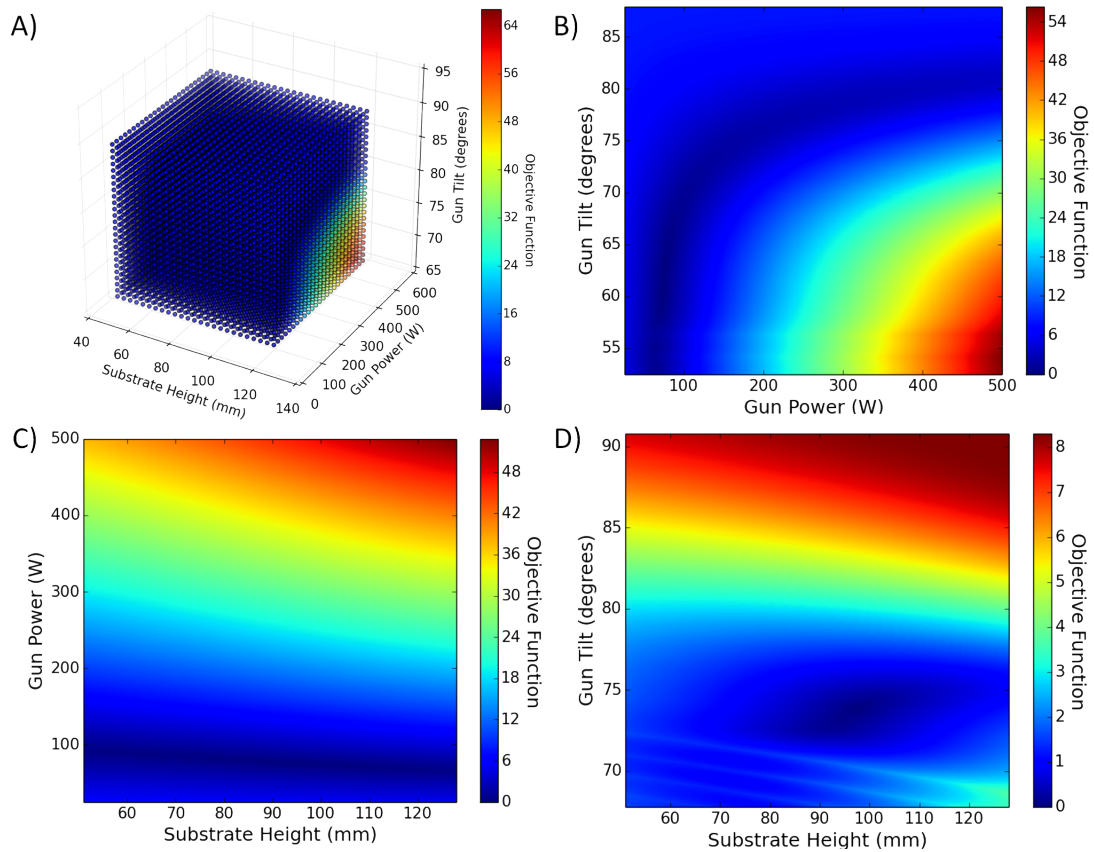
Figure 3.6   Contour plots of the objective function with respect to the optimized sputtering variables, substrate height, gun power, and gun tilt. (B-D) 2D slices of the full contour plot shown in (A). The substrate height was set to 101 mm (B), the gun tilt was set to 62° (C), and the gun power was set to 75 W (D).

To overcome these potential issues, a "seeded" multi-start optimization method was devised. Fig. 3.7 shows a general outline of the procedure on a simplified response

surface. During the initialization of the optimization procedure, n_{seed} randomly selected values were used to populate the search domain. The values of each n_{seed} variable was constrained to be within the physically constrained limit of the optimized variables, i.e. the gun power, gun tilt, and substrate height. The value of the objective function, referred to as the objective value, for each n_{seed} point was calculated, as shown in Fig. 3.7, Step 1. After all objective values were calculated, the point with the minimum objective value was chosen to be the initial location for full optimization, as shown in Fig. 3.7 Step 2. The rest of the objective values were then reweighed by harshly penalizing objective values from numerically similar sputtering conditions, shown in Fig. 3.7 Step 3. This process was repeated until an n_{start} number of points were selected for a multi-start optimization. For the multi-start optimization, the condition from each n_{start} was used to perform a full optimization. The results from each of these optimizations were then analyzed, and the optimizations with the lowest objective values were used for further analysis.

Optimization of a Model Thickness Gradient

First, the performance of the optimization procedure to determine the sputtering conditions from an ideal sample was evaluated. For this evaluation the sputter model was used to simulate the deposition rate distribution using the experimental deposition conditions shown in Table 3.3, Condition 1. The effect of the number of n_{seed} and n_{start} points for optimization performance was evaluated. For this evaluation, 5, 20, 40, 60, 80, and 100 n_{seed} points for 1, 2, 3, 4, and 5 n_{start} points multi-start optimizations were performed. The procedure using each n_{seed} and n_{start} combination was repeated 300 times. The calculations were repeated due to the randomness associated with the selection of the n_{seed} parameter values. This results from these repetitions were used to evaluate the average performance of the algorithm. From each optimization, the predicted deposition parameters and calculation time were
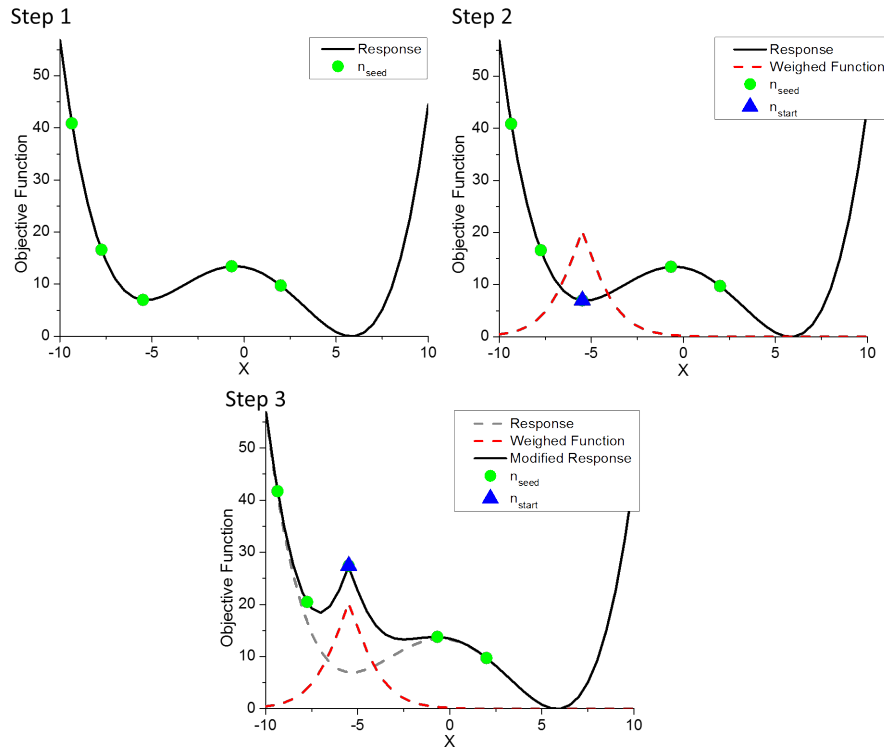
Figure 3.7 A diagram outlining the steps for the seeded multistart algorithm that was used for the optimization procedure. Due to the complexity of the response plots in this study, a representative response function is shown instead of a true response plot for the sake of clarity.

recorded. The predicted deposition parameters were compared to the initial experimental conditions, and the relative error, RE_c, of each sputtering variable, c, was calculated:

$$RE_c = \frac{c_{opt} - c_{des}}{c_{des}} \times 100\% \qquad (3.34)$$

Where c_{opt} was the value of the sputtering variable c that the optimization algorithm determined and c_{des} was the value of the sputtering variable c used to create the desired deposition rate profile.

A unified binary metric was created to determine if an optimization was successful. For this binary metric an optimization passed if all sputtering variables were within 1 relative percent error of the experimental sputtering parameters, otherwise the

61

optimization failed. Using this metric, the pass rate, $PR\left(n_{seed}, n_{start}\right)$, was calculated using:

$$PR\left(n_{seed}, n_{start}\right) = \frac{t_{passed}\left(n_{seed}, n_{start}\right)}{t_{total}\left(n_{seed}, n_{start}\right)} \qquad (3.35)$$

Where $t_{passed}\left(n_{seed}, n_{start}\right)$ and $t_{total}\left(n_{seed}, n_{start}\right)$ were the number of passed trails and total trails for a of n_{seed} and n_{start}, respectively. The average calculation time from each optimization trails was also determined. Fig. 3.8 shows the results of these calculations
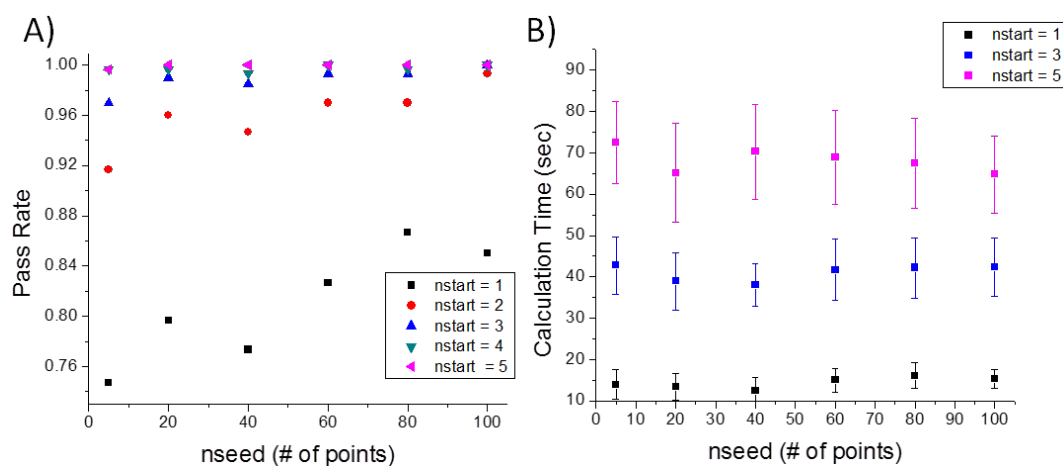
Figure 3.8   (A) The calculated pass rate of the optimization algorithm using different values of n_{start} and n_{seed}. (B) The average calculation time of the optimization algorithm using different values of n_{start} and n_{seed}. In (B) the lines associated with the average calculation time using n_{start} of 2 and 4 are not shown for clarity.

Fig. 3.8 A) shows that the pass rate for $n_{start} \geq 3$ was greater than 97% for all values of n_{seed}; reaching a pass rate of greater than 99 % when $n_{seed} = 100$. It also shows that pass rate for $n_{start} = 2$ and a $n_{seed} = 5$ yielded a pass rate of 92%. As the n_{seed} value was increased from 5 to 100, the pass rate increased to 99%. The set of single-start optimizations, $n_{start} = 1$, have significantly lower performance than the multi-start optimization. The single-start optimizations have a pass rate of 75% when $n_{seed} = 5$. This pass rate only raises to 85-87% as n_{seed} was increased to 80-100 points.

62

This shows that that the issue of multiple minima and a variable gradient response surface probably detrimentally affected the single-start optimizations. Additionally due to the relatively high pass-rate from all of the multi-start optimizations, it shows the seeded multi-start procedure that was used overcame these issues. It should be noted that while several conditions resulted in reported pass rates of 100%; it should not be concluded that those conditions will always yield a pass. Instead, a 100% pass rate indicates that to find the true pass rate more than 300 trails would need to be performed.

The average calculation times for the optimizations using n_{start} of 1, 3, and 5 are shown in Fig. 3.8 B). This figure shows that the calculation time increases as n_{start} increases, but the calculation time is relatively constant as a function of n_{seed}. The reason that the optimization is relatively constant with n_{seed} is due to the fact that as n_{seed} is increased the initial conditions for each n_{start} optimizations are likely closer to a minimum. Therefore, the average time for each optimization is lowered because iterations of the optimization are needed before terminating on a solution.

From this stage of the validation, it can be concluded that by performing the optimization procedure with $n_{start} = 2$ and $n_{seed} = 100$ or $n_{start} \geq 3$, there is a 99% confidence that a passable sputtering condition will be determined. Furthermore, this optimized sputter conditions will be determined within 29.8 seconds - 72.5 seconds, which is 3-4 orders of magnitude faster than determining the sputter conditions without the optimization.

3.3 Conclusions

An accurate semi-empirical sputter model that can predict the deposition rate of materials deposited by DC magnetron sputtering has been developed. The model reduces the number of calibration depositions that need to be performed to determine the final deposition conditions, expediting experimental work. This model accounts

63

for off-center, tilted DC sputtering sources as well as shadowing effects from the gun chimneys, and was validated through a series of experimentally measured deposition rates of Cu deposited at gun-tilts varying from 0° to 31.3° and DC powers varying from 50 W to 200 W. The model predictions had a 2.12% ± 1.71% average relative error for the tall chimney predictions over a gun tilt range of 17.7° - 31.3°, and 4.14% ± 3.02% for a 0° - 31.3° gun tilt range for the short chimney model predictions. The model had a maximum error of 13.8% for the 50-W model without the gas chimney. Comparison model that accounted for chimney shadowing and a model that did not account for chimney shadowing showed that accounting for chimney shadowing significantly increased model performance. The average accuracy of the prediction improved by 5.47 times and the maximum relative error decreases by 5.87 times the prediction that does not account for chimney shadowing.

The semi-empirical sputter model was further improved by using a Nelder-Mead optimization procedure to intelligently identify deposition conditions for sputtered HTE thin films. The optimization employed soft constraints, as well as a multiple stage multi-start method. The optimization procedure was validated for predictive capabilities in the absence of experimental errors. A strict definition of a successful optimization was defined as optimization results that were within 1% of the synthesis condition. The optimization procedure had an average calculation time of 29.8 seconds and a pass rate >99%. Overall, the combination of the semi-empirical model and the optimization procedure represents a 3-4 order of magnitude acceleration in the rate at which HTE samples can be designed and deposited.

CHAPTER 4

HTE METHODOLOGY TO INVESTIGATE

HIGH-TEMPERATURE THIN-FILM MATERIALS

4.1 MOTIVATION AND EXPERIMENTAL

As stated in section 1.4; many HTE methods have been developed to study material systems, no such method has been developed prior to our work to investigate crystallographic dynamics of high temperature materials. In this section, a HTE experimental methodology that we developed will be discussed [78]. The developed methodology addressing this problem was validated through a compositional investigation of NiAl Bond Coat thin-film system. The NiAl BC system was chosen for a 2-fold reason. First, the NiAl BC system has been studied in detail. The results of these previous were used for benchmark comparison of the results from the HTE investigation, giving insight into the validity and pit-falls of such techniques. Second, it was chosen due to the dynamic nature of NiAl BCs, where potential metallographic phase changes can occur while the thin-film is being oxidized. During the design of the HTE investigation of NiAl BCs, it was determined that it was important to capture the aspects of the metallographic phase changes and oxidation during the initial stages of heat treating. It is important that α-Al$_2$O$_3$ rapidly form on the surface of the metal as the baseline figure of merit for these BC materials is resistance to

---

Parts of chapter adapted from: C. J. Metting, J. K. Bunn, E. Underwood, S. Smoak, J. R. Hattrick-Simpers, (2013). Combinatorial Approach to Turbine Bond Coat Discovery. ACS Combinatorial Science, 15(8), 419-424, with permission from the American Chemical Society. See Fig. C.3 for copyright permission.

continual oxidation. These phase dynamics were investigated by following the general procedure outlined in Fig. 4.1.
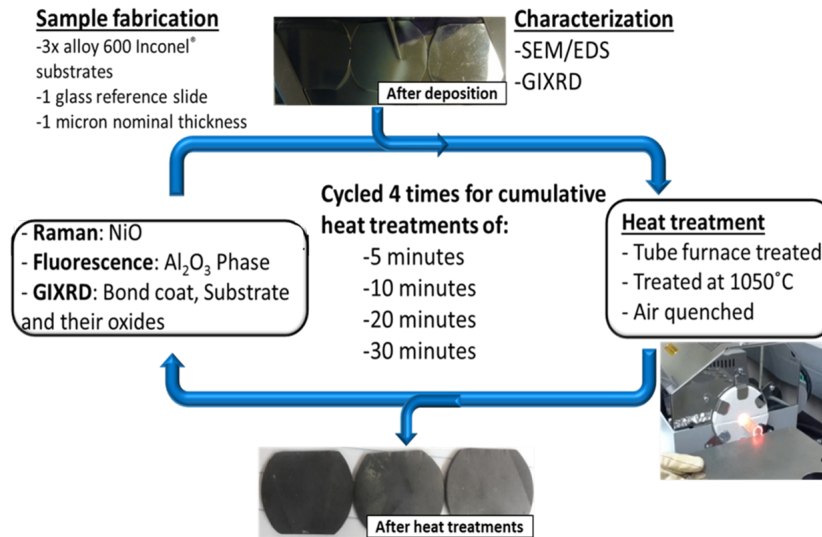
Figure 4.1   A pictorial representation of the HTE experimental procedure that was used to investigate high temperature phase dynamics of a set of CCS NiAl BCs samples.

During this investigation, 1 μm thick CCS NiAl BC thin films were sputtered on polished polycrystalline Inconel 600 alloy tokens. Inconel token were chosen as the substrate because Inconel is a representative material for the super alloys used in turbine blades. Details of substrate cleaning and processing as well as the sputter deposition procedure that was used can be found in Ref. [78]. The CCS was also deposited on a glass slide so that the as-deposited crystal phase of the Ni-Al films could be determined without interference from the substrate diffraction peaks. The glass reference sample was also used to measure the film composition with energy dispersive spectroscopy (EDS) using an FEI Quanta 200 SEM/EDS. The results of the EDS are shown in Fig. 4.2 A).

After synthesis, each of the tokens were cyclically heat treated in a Carbolite 2.54 cm diameter quartz tube furnace in air at 1323 K. The tokens were heated for cumulative times of 5 mins, 10 mins, 20 mins, and 30 mins. After each heating cycle

66

the tokens were quickly transferred to a perforated Inconel sheet and air quenched to room temperature. Between each heating cycle, four separate compositions from each tokens were characterized points with XRD, Raman spectroscopy, fluorescence. Raman/fluorescence measurements were taken at three separate points for each of the compositions studied to ensure that the results from these measurements were reproducible, shown by the yellow circles in Fig. 4.2 A). Only one XRD measurement was taken at each studied composition, shown by the blue lines in Fig. 4.2 A).
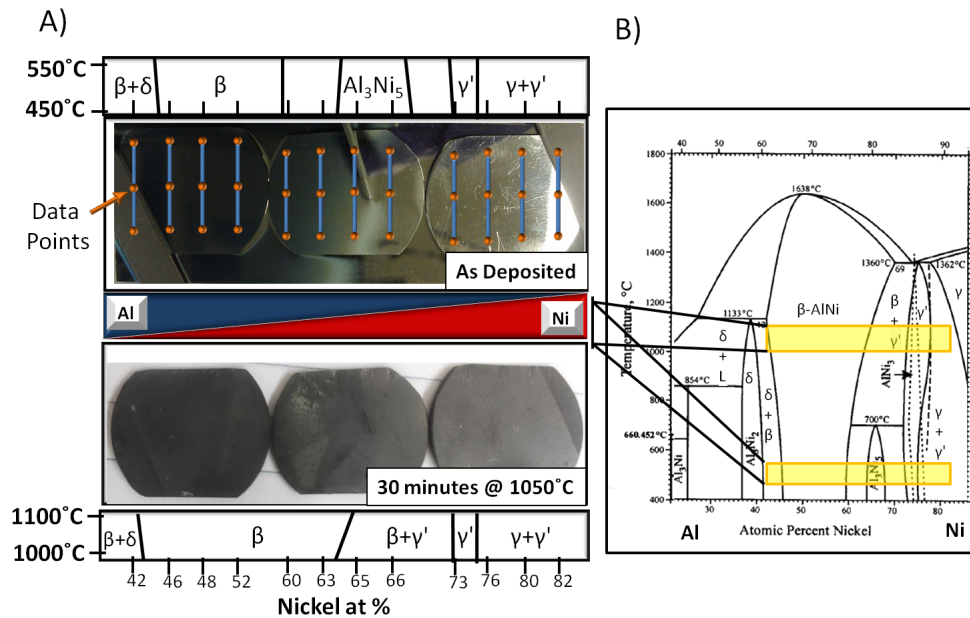
Figure 4.2 Pictures of the samples along with the the composition gradient of the film and the expected crystal phases. A) Top: Pictures of the samples as-deposited and A) Bottom: Pictures of the samples after 30 minutes of heat treatment. B) The NiAl Phase diagram highlighted with the temperatures of the expected phases of the samples. In A) top yellow circles were where Raman/fluorescence measurements were taken and blue lines were where XRD measurements were taken.

After the 30 minutes heat treatment, the samples were visually inspected for changes from the as-deposited samples. Fig. 4.1 shows visible regional differences in the oxidized film, especially around the sample with 65 at.% Ni that has been annealed for 30 mins. This transition was credited to an expected phase transform from the pure β to a mixed β/γ' phase, as predicted by the NiAl phase diagram

67

shown in Fig. 4.2 B).

4.2 RESULTS AND DISCUSSION

The as-deposited NiAl CCS tokens on Inconel and on the glass slide were characterized with XRD. The XRD from these sample showed that areas of the sample which contained 46%-63% Ni had diffraction peaks association with the β and γ' NiAl phases. It also showed that the area of the sample which contained 76%-82% Ni exhibited diffraction peaks associated with a pure γ'-NiAl phase. These results differ from the expected room temperature phase that are shown in the phase diagram in Fig. 4.2 B). Thus, either sample processing during the sample deposition or the high energy deposition process resulted in the formation of meta-stable nonequilibrated NiAl structures across the CCS. The deposition of meta-stable phases is known to occur when sputter deposition is used [17].

Once the as-deposited samples were characterized, the tokens were heat cyclically heat treated and characterized. For the sake of brevity, a full discussion of the oxidation behavior after a 5 minute heat treatment will be given here, and a detailed discussion of the other heat treatment times are given in Ref [78].

Fig. 4.3 A) and B) show the fluorescence and Raman results for the 5 minute heat. Details of how these measurements were taken can be found in the experimental methodology subsection of section 2.3. Fig. 4.3 A) is given in the absolute wave number and Fig. 4.3 B) is given in Raman shift. The figure is presented this way because fluorescence responses have a defined absolute wavenumber and Raman excitations occur relative to the wavelength of light used to induce excitations.

In Fig. 4.3 A) two distinct Al_2O_3 phases were observed; α-Al_2O_3 and θ-Al_2O_3. The peaks located at 14400 cm^{-1} are attributed to $^2E \rightarrow ^4A_2$ energy transition in the α-Al_2O_3 phase, labeled with R in the figure [15, 86]. This peak is shifted from the typical peak corresponding a $^2E \rightarrow ^4A_2$ which common for scale forming Al-containing

68
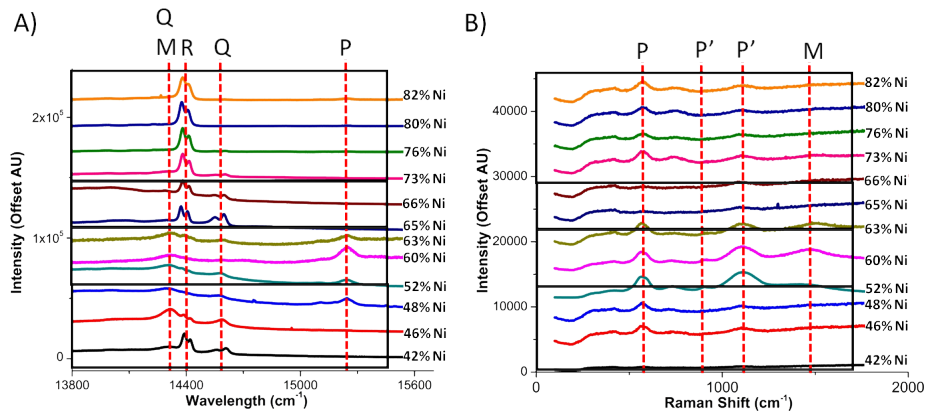
Figure 4.3   A) and B) The fluorescence and Raman spectroscopy response from the NiAl BCs after 5 minutes of heat treatment, respectively. A 632.8 nm red laser was used during the measurements of A) and a 441.6 nm blue laser was used during the measurements of B). In the figure R: R1, R2 α-Al$_2$O$_3$ Fluorescence, Q: Q1,Q2 θ-Al$_2$O$_3$ Fluorescence, M: NiO 1-Magnon Raman, P: NiO 1-Phonon Raman, and P': NiO 2- Phonon Raman.

alloys. In such alloys effects from residual stresses, concentration of Cr and other contaminants, and temperature can change the location of this peak [67, 73, 141]. The peaks located at 14550 cm^{-1} and 14500 cm-1 were attributed to the θ-Al$_2$O$_3$ phase, labeled with Q in Fig. 4.3 A) [129]. The peaks located at 14000 cm^{-1} and a peak at 14300 cm^{-1}, were contributed to a strained θ-Al$_2$O$_3$ phase. The strained θ-Al$_2$O$_3$ phase has been shown to exist in samples where a γ-Al$_2$O$_3$$\rightarrow$$\theta$-Al$_2O_3$ phase transformation occurs [129]. These peaks were are labeled as θ-Al$_2$O$_3$ in Fig. 4.3 A).

In Fig 4.3 B), multiple different Raman excitation modes of NiO were observed. The NiO 1-phonon excitation mode is located at 566 cm^{-1}, the NiO 2-phonon excitation modes are located at 733 cm^{-1}, 920 cm^{-1}, and 1109 cm^{-1}, and the NiO 2-magnon mode is located at 1500 cm^{-1} [81]. No Raman active modes for the Al$_2$O$_3$ peaks were observed in either of these measurements.

The XRD analysis, shown in Fig. 4.4 for the 5 minute heat treatment, of this system was non-trivial due to the similarities in composition and crystal structure between the bond coat, the Inconel substrate, and the surface oxides. These sim-

69
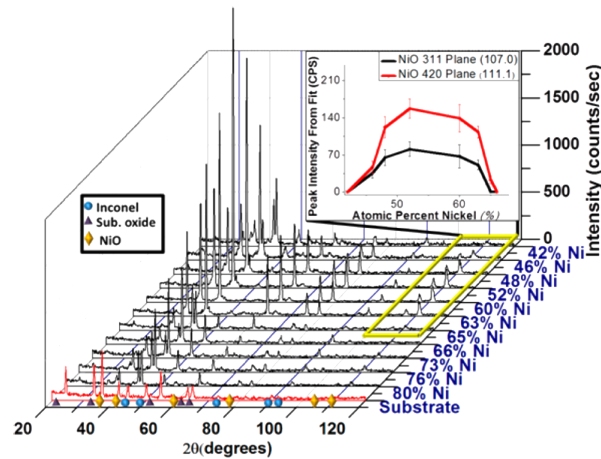
Figure 4.4 XRD results from the NiAl BC samples after 5 minutes of heat treatment. Inset) Peak intensity of two NiO diffraction peaks compared to the sample compositions.

ilarities made conclusive attribution difficult as many of the major peaks could be associated with multiple components of the system 4.4. Still, important information on the growth of NiO was determined from these results. The relative intensities of peaks uniquely attributed to NiO have been plotted in the inset of Fig. 4.4.

Combined analysis of the fluorescence, Raman, and XRD results lead to a comprehensive understanding of the oxidation of the NiAl BCs. Fig. 4.3 and Fig. 4.4 shows the combined spectroscopic and diffraction results for a 5 min heat treatment. Fig. 4.3 was partitioned into four sections of similar oxidation characteristics, as shown by the bold black lines. These four partitions correspond to the Ni atomic percentages of 42%-48%, 52%-63%, 65%-66%, and 73%-82%.

Comparison of these partitions to the XRD results of the as-deposited samples show that the 42 at.%-48 at.% Ni and the 52 at.%-63 at.% Ni region, which corresponds to a meta-stable β-NiAl/γ'-NiAl phase, exhibited primarily NiO. This results was is further supported by the high relative intensities of the NiO diffraction peaks, shown in the inset of Fig. 4.4. Previous studies have shown that the 52 at.%-63 at.% Ni region grew pure Al_2O_3. The disagreement between the oxidation results displayed

70

here and in previous literature could be due to the meta-stable as-deposited phase which contained significant amounts of the β/γ'-NiAl phase. The β/γ'-NiAl phase has been shown to promote the nucleation of NiO in previous studies [122].

The 65 at.%-66 at.% and the 73 at.%-82 at.% Ni regions, exhibited strong Al$_2$O$_3$ oxide growth, as shown by strong fluorescence peaks in Fig. 4.3 A). The 65 at.%-66 at.% Ni regime showed suppressed Ni oxidation, shown by the lack of discernible NiO diffraction in Fig. 4.4 and with small NiO Raman peaks in Fig. 4.3 B). This is in contrast to the 73 at.%-82 at.% Ni, which exhibited moderate NiO growth, as shown by the short Raman peaks and the small diffraction peaks. While NiO was observed in this region, the combination of the small NiO signal and the strong α-Al$_2$O$_3$ signal indicates that α-Al$_2$O$_3$ is the primary oxide that is formed.
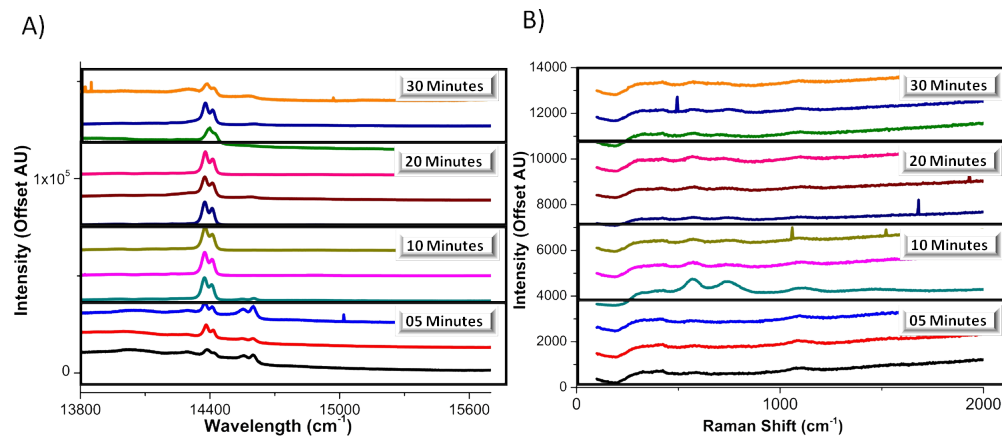
Figure 4.5 The fluorescence, A), and Raman spectroscopy measurements of the 66 at.% Ni sample for all of the cyclic heating times.

The results from all of the NiAl BC compositions showed that the 66 at.% Ni sample exhibited the most desired oxide growth, having the lowest NiO Raman and XRD signal while having the most intense Al$_2$O$_3$ signal. An in depth analysis of the oxidation dynamics of this sample with respect to the heating time was performed. All of the Raman/fluorescence measurements of this sample with respect to heating time are shown in Fig. 4.5. The fluorescence signal after minutes of heat treatment

71

exhibit strong α-Al_2O_3 and θ-Al_2O_3 peak.

After 10 minutes of heat treatment, the intensity of the θ-Al_2O_3 fluorescence peak significantly decreased, the intensity of the α-Al_2O_3 increased, and small NiO Raman peaks start to form. The transitions in the Al_2O_3 indicates that initially the sample formed a θ-Al_2O_3 which phase transformed to α-Al_2O_3 as the heating time was increased.
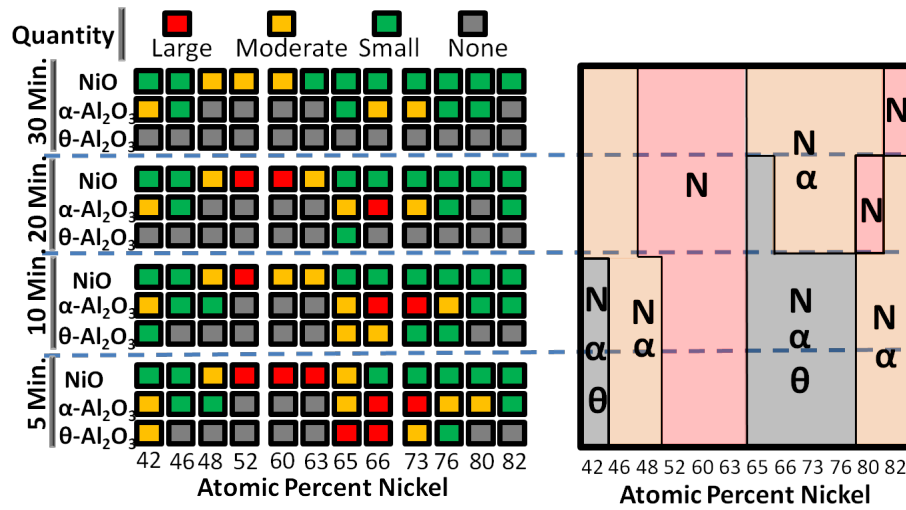
Figure 4.6   Schematic summarizing the oxide formation trends based on the combined results of the Raman, fluorescence, and XRD measurement. 'α' is α-Al_2O_3, 'θ' is θ-Al_2O_3, and 'N' is NiO. The right diagram shows the general oxidation trends, while the left shows is a detailed representation of these trends.

As the heating time was increased to 20 minutes, the α-Al_2O_3 continues to grow in intensity while the intensity of the NiO Raman peaks continue to remain relatively unchanged. This indicates that the α-Al_2O_3 continues to form. The formation of a strong α-Al_2O_3 scale protects the NiAl BC from NiO oxidation.

The α-Al_2O_3 peak intensity significantly decreases as the heating time is increased to 30 minutes and a small θ-Al_2O_3 fluorescence peak reappeared. This change in intensity of the Al_2O_3 fluorescence peaks was attributed to oxide spallation due to the stresses formed in the films from the cyclic heating. The spallation caused some of the α-Al_2O_3 to fall off the samples, exposing the NiAl BC to the atmosphere.

72

The exposed NiAl BC then oxidized to form more θ-Al$_2$O$_3$. Interestingly, the NiO Raman peak intensities still remained relatively constant. This indicates that the newly formed θ-Al$_2$O$_3$/α-Al$_2$O$_3$ continued to suppress the formation of NiO.

With all three characterization techniques, surface averaged information about NiO and the Al$_2$O$_3$ phases present during oxidation was obtained. The results of this combined analysis are summarized in Fig. 4.6. The left diagram of Fig. 4.6 shows a qualitative analysis of the amount of each oxide phases for each f the samples, while the right diagram represents a simplified oxide "phase diagram". The results of the different characterization measurements are in agreement with each other. Overall, these results indicate that alloys containing higher amounts of Ni preferentially formed Al$_2$O$_3$. Furthermore, the rapid Al$_2$O$_3$ formation 73 at.%-82 at.% Ni is commensurate to previous studies which showed desirable oxidation of γ/γ'-NiAl alloys [34, 45, 50, 144].

4.3 Conclusions

A HTE experimental methodology to evaluate phase dynamics of high-temperature CCS thin-film samples was developed. The methodology uses a sputter deposition method to create natural composition gradient thin-films. The oxidation dynamics of the CCS thin-film was analyzed via a suite of characterization techniques including XRD, Raman spectroscopy, and fluorescence. A validation study on the well known NiAl bond coat system was performed. The oxidation of the NiAl BCs was monitored in samples that were cyclically heat treated at 1323 K. The results agreed with the previously reported trends that alloys containing higher amounts of Ni preferentially formed Al$_2$O$_3$ was observed. The ability to accurately monitor the oxidation of the NiAl samples at various compositions and the agreement of oxidation trends with previous literature displayed the validity of the proposed HTE methodology.

It should be noted that one difference in the current study and previous litera-

73

ture was observed in samples containing 52 at.%-63 at.% Ni. Previous reports state that these samples should grow pure Al_2O_3, but in the current study they grew a significant amount of NiO. The disagreement was attributed to the deposition of a meta-stable β/γ'-NiAl phase in these samples. The β/γ'-NiAl phase has been shown to promote the nucleation of NiO, which was observed here. The deposition of meta-stable crystal phases is a known issue when using sputter deposition. In the future, the deposition meta-stable crystal phases needs to be monitored carefully when using this methodology.

CHAPTER 5

SS-AUTOPHASE

5.1 MOTIVATION AND EXPERIMENTAL

As stated in section 1.4, automated analysis and identification of diffraction patterns and spectrographs are open problems in the field due to the complexity of performing such an analysis. In previous studies, assisted or unassisted clustering analysis tools have been developed to automate the classification of different diffractograms [4, 5, 27, 63, 64, 70, 69]. In these techniques, similar diffraction patterns are partitioned into distinct clusters. The identity of each cluster is then be quickly analyzed, minimizing the amount of human analysis that is needed.

Some examples techniques that have been used for this purpose are hierarchal clustering analysis (HCA), constrained reasoning clustering analysis (CR), mean shift theory (MST), dynamic time warping (DTW), and non-negative matrix factorization (NMF). HCA is an unassisted clustering approach that determines the similarity of each dataset to each other through the use of a similarity metric", such as the Pearson weighing coefficient. Once the similarity of each dataset has been determined, a human expert sets a threshold value of similarity to cluster the data [70]. CR analysis uses a graph theory approach to perform diffraction clustering analysis. In this approach, constrained programming is used to determine unique basis sets. Combinations of basis sets are then used to cluster the data [27, 64]. MST is a versatile

---

Parts of chapter adapted from: J. K. Bunn, J. Hu, and J. R. Hattrick-Simpers, (2016). Semi-Supervised Approach to Phase Identification from Combinatorial Sample Diffraction Patterns. JOM, 68(8), 2116-2125, with permission from Springer. See Fig. C.4 for copyright permission.

clustering approach that can be performed in a semi-supervised "guided" mode or an unsupervised "fast" mode. In this approach, each diffraction pattern is transformed into a complex feature vector. The density of these feature vectors are then compared to underlying probability density functions to determine the clusters of the datasets [63]. The determination of the underlying probability density functions can either be determined from the data sets themselves or can be determined through the use of reference diffraction patterns. DTW is similar to guided MST, as it uses knowledge about the diffraction patterns of possible pure phases. The patterns of pure phases are used to determine how similar each new diffraction pattern is to the pure phases, and decides what phase/combination of phases exist in the pattern [5]. NMF is also similar to MST. NMF uses linear algebra to decompose sets of diffraction data into underlying basis patterns. These basis patterns are then linearly super-positioned in a weighted manner to recreate the experimental patterns from the data. The weight associated with each basis pattern is then used to determine the identity of the diffraction patterns [69]. Although it has been demonstrated that these approaches can reduce the time needed to analyze large sets of XRD data, a significant amount of manual expert analysis is still needed to guide the clustering algorithms.

Most of the manual analysis for evaluating clustering techniques comes in the form of ensuring that each cluster is homogeneous. This confirmation involves manually ensuring that the intra-cluster diffraction patterns are similar and that the inter-cluster diffraction patterns are dissimilar. Due to the fact that clustering analysis is most likely to fail at the boundaries between clusters, this process becomes very arduous when a dataset has a large number of clusters.

An alternative to clustering algorithms is supervised classification algorithms, referred to here as classification algorithms. For classification algorithms, training data set is created by analyzing and labeling a subset of the total number of diffraction

patterns. The classification algorithm learns from these training data sets. The trained classifier is then used to phase map the remaining diffraction patterns. The accuracy of these approaches is intimately related to the quality of the training data. A human expert has to ensure that representative samples of each phase are included in the training set for the classifier to have high accuracy. Selection of representative datasets is performed by having an expert examine each pattern in the sample collection. The expert chooses data sets that are dissimilar to all other selected datasets and ensure that they contain each crystal phase. The process of presorting the data by hand is time consuming and highly susceptible to error as it is easy to be overwhelmed by the complexity of the data or miss low-intensity peaks.

Here the details of a demonstrated a semi-supervised approach to automated phase attribution called SS-AutoPhase will be given [12]. In this approach, representative datasets are algorithmically determined from a K-means clustering algorithm. The algorithmically selected datasets were then labeled by a human expert who identified the existence or absence of phases in each dataset. The labeled training dataset was then used to train an AdaBoost classifier. The trained AdaBoost classifier was used to automatically determine the phases present for every pattern in the library. See section 2.4 for details about how AdaBoost classifiers are trained and are used to classify new datasets.

SS-AutoPhase was validated using two different approaches. In the first approach, the performance of the AdaBoost classifier (referred to here as AutoPhase) and the effect of data preprocessing were investigated. For this investigation, AutoPhase classified the NiAl datasets described in chapter 4. This sample was selected due to the wide variety of characterization techniques that were used and the moderate complexity of the data. The results of this study showed that AutoPhase had an accuracy of greater than 98.4 % when labeling all crystalline phases if the data was background subtracted and a representative training set was used. More details of

77

this validation can be found in Ref. [11].

The focus of this chapter is on the second validation study, which evaluated the overall performance of SS-AutoPhase and its ability to select representative datasets via clustering. Furthermore, the performance of SS-AutoPhase was compared to common clustering techniques used in the field. In this investigation, SS-AutoPhase was bench marked on 278 diffractograms from a FeGaPd "open-data" combinatorial thin-film library [55, 70]. This dataset of was selected because of its complexity, containing seven previously identified phases, and its previous use as a baseline data set for new knowledge extraction algorithms such as HCA, MST, and NMF.

5.2 Theory

Feature Selection and Creation

The performance of SS-AutoPhase strongly depends on a set of features extracted from the sample. For general spectroscopic data, such as Raman and fluorescence and diffraction data, such as XRD, the presence of peaks and peak shape are the most important aspects of the data when performing human analysis. This was emulated in the feature extraction algorithm of SS-AutoPhase, which uses the peaks and the slopes (down, up, or flat) to describe the data sets. Before SS-AutoPhase determines the values of these features, it first smooths the data by calculating a moving average. This smoothing acts as a noise reduction filter and was applied to the entirety of the data sets. The number of data points that the moving average filter used, referred to here as the smoothing window data points, is a tunable parameter that is an input for SS-AutoPhase. After all of the data is smoothed, a sliding "trend" window is used to determine the values of the peaks and slope features. The sliding trend window is similar to the smoothing window, and is the number of data points around a central data point for which the trends will be evaluated. For peak features values, F_{peak},

the following equation was used:

$$F_{peak}(x_c) = \begin{cases} I(x_c) & ; I(x_c) - I(x_c + \Delta x) > T \text{ and } I(x_c) - I(x_c - \Delta x) > T \\ 0 & ; \text{otherwise} \end{cases}$$

$$(5.1)$$

Where x_c is the central x-value of the sliding window, $I(x_c)$ is the intensity value at the point x_c, Δx is half of the x-range of the sliding window, and T is a threshold feature value. The value of T should be set to the average noise value of the smoothed data. Unlike the calculated peak feature values, the slope feature values are calculated in two steps. In the first step, a point-wise value at every data point is evaluated. This point-wise value is then used to decide if the slope-trend, S, is "up", "flat", or "down" using the following expression:

$$S(x_j) = \begin{cases} \text{up} & ; I(x_{j+1}) - I(x_{j-1}) > T \\ \text{flat} & ; I(x_{j+1}) - I(x_{j-1}) \leq |T| \\ \text{down} & ; I(x_{j+1}) - I(x_{j-1}) < -T \end{cases} \quad (5.2)$$

Where x_j and $I(x_j)$ are the x-value and intensity value at a point j, respectively. In the second step, the slope feature values, F_{up}, F_{flat}, and F_{down} are calculated by counting the number of similar slope trends exists within the sliding window. The calculation of a slope feature F_k is given by:

$$f_k(x_j) = \begin{cases} 1 & ; S(x_j) = k \\ 0 & ; S(x_j) \neq k \end{cases} \quad (5.3)$$

$$F_k(x_c) = \sum_{x_j = x_c - \Delta x}^{x_c + \Delta x} f_k(x_j) \quad (5.4)$$

Where $k = $ up, flat, or down and $f_k(x_j)$ is variable used to transform the value of $S(x_j)$ to a numeric value for the calculation of $F_k(x_c)$.

79

Once all of the feature values have been calculated, SS-AutoPhase uses an AdaBoost classifier to select the most distinguishing features from the training data and uses these weighed features to produce the final phase classifier. The details of how this process is performed is outlined in section 2.4.

Representative Training Data Selection Via K-Means Clustering

K-means clustering analysis was used to determine what subset of the diffraction patterns would be included in the training set [41, 90]. This type of clustering was selected due to its relative simplicity and because it is able to generate clusters without human assistance. For this clustering analysis, the intensity values from all XRD patterns were used as a feature vector and the Euclidean distance between the samples was used as a measure of similarity for clustering.

The initial cluster positions were generated pseudo-randomly to limit the amount of human input required to execute the algorithm, and were updated as the clustering process progressed [3]. While the placement and clustering process is autonomous, the number of clusters does need to be defined. The cluster number was defined as the number of datasets that should be selected to be in the training set. Previously, we determined that 13%-20% of the entire dataset was sufficient to train AutoPhase [11]. The previous study did not use the k-means clustering approach, so an investigation into the effect of training set size on classification accuracy was performed. The results of this study are given in section 5.3. Once all diffraction patterns were clustered, the sample closest to the centroid of each cluster was selected to be labeled and placed in the training set.

The implemented clustering algorithm will "over-cluster" the data. Traditionally, over-clustering is avoided due to the creation of redundant clusters, which can complicate analysis of each cluster. In SS-AutoPhase, the formation of redundant clusters

is desirable, as it select multiple copies of the same phases to be labeled and to be used for training. Furthermore, each copy of the phases will contain slightly different features, selecting datasets with representative variations of each phase and thus strengthening the predictive power of the AdaBoost classifier.

5.3 RESULTS AND DISCUSSION

Manual and Automated Phase Identification of FeGaPd Diffraction Patterns

After the SS-AutoPhase identified training datasets via k-means clustering, a human expert labeled these samples with the existence or absence of each crystal phase. The expert used the peak identities shown in Fig. 5.1. During the labeling process, the range of the diffraction patterns was constrained to the same 2-θ range reported in Fig. 2 of Ref. [63], 37°-48° 2-θ. Based on the patterns selected by k-means clustering, it was determined that the previously identified phases; Pd_9Si, Fe_3Si, FCC FePd, BCC Fe, FCC Fe, FeGa, Unknown 1, and Unknown 2, did not describe all the observed peaks. Further analysis of the diffraction patterns indicated that a new unidentified phase existed, referred to here as Unknown 3. The Unknown 3 phase was included in the phase labeling and was associated with peaks at 39.9° and 41.7° 2-θ. The discovery of a new phase in a previously studied open-dataset by itself is an example of one major advantage of SS-AutoPhase. A discussion of the potential identity and importance of the Unknown 3 phase is given in Ref. [12].

The AdaBoost classifier performed feature extraction on all samples in the FeGaPd sample and was trained with the labeled training data. The threshold value, T from Eqns. 5.1 and 5.2 associated with feature extraction was set equal to 5% of the maximum value of each diffraction. This threshold value is a naive approximation of the noise value in the data, but will still filter out most of the insignificant features.

81
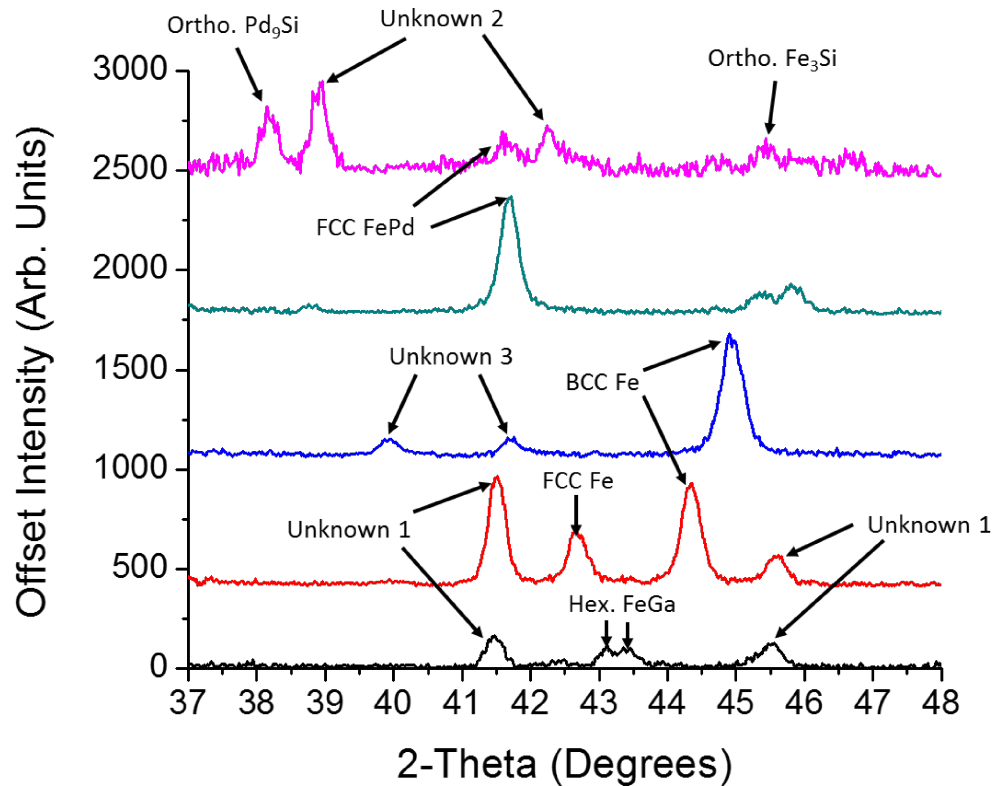
Figure 5.1   Representative XRD patterns for all of the crystal phases identified in this study. The Inorganic Crystal Structure Database, the NIST Structural Database, and Ref. [69] were used to identify locations of the diffraction peaks except for the Unknown 3 phase, which were determined from expert analysis.

The entire FeGaPd sample was then phase mapped with the AdaBoost classifier. Manual expert phase mapping analysis (MEPMA) was performed on all diffraction patterns to evaluate the validity of the phase mapping from SS-AutoPhase. The results from the MEPMA were considered to be the true phase identity of each sample. This true identity was used in the calculation of the accuracy, true positive rate, and true negative rate for the SS-AutoPhase predictions (See Eqns. 2.5, 2.6, and 2.7 for mathematic description calculations).

Investigation of Training Sample Size and Clustering

An evaluation of the effect of training set size was performed by evaluating the performance of SS-AutoPhase trained with training sets containing 5%, 10%, 15%, 20%, 25%, 30%, 35%, and 45% of the entire data set. During this evaluation, all of the diffraction patterns were clustered via k-means clustering. The training datasets were then selected via the procedure outline in section 5.2. This means that if 5% of the data was used for training then the number of clusters was equal to the number of patterns that representative that percentage (i.e. there are 278 samples in total so for a 5% training set size for 14 clusters were created). SS-AutoPhase was then trained with the selected training set samples and was used to predict the phase identity of all other samples.

The process of training set selection, SS-AutoPhase training, and algorithmic phase mapping was repeated 25 times for each training set size. These calculations were repeated to mitigate sampling errors associated with the pseudo-random initialization of the centroids for the k-means clustering algorithm. Once all predictions were performed, the standard deviation and average true negative rate, true positive rate, and accuracy were calculated. The results of these calculations are shown in Fig. 5.2. Before an analysis of these trends is given, it should be noted that when the trends were analyzed, changes in average data points were only considered statistically significant if it moved the average value outside of the standard deviation of the prediction.

Fig. 5.2 A) shows that the average true negative rate R_{TN} is above or statistically equal to 90% for the BCC Fe, FCC FePd, Pd_9Si/Fe_3Si, and Unknown 2 phases for all training set sizes. This indicates that SS-AutoPhase classifier has reached a maximum of negative prediction capability for these phases when using 5% or more of the total data for training. R_{TN} of the FCC Fe, Hexagonal FeGa, Unknown 3 phases initially increases to statistically within 90% when the training set size was increased from
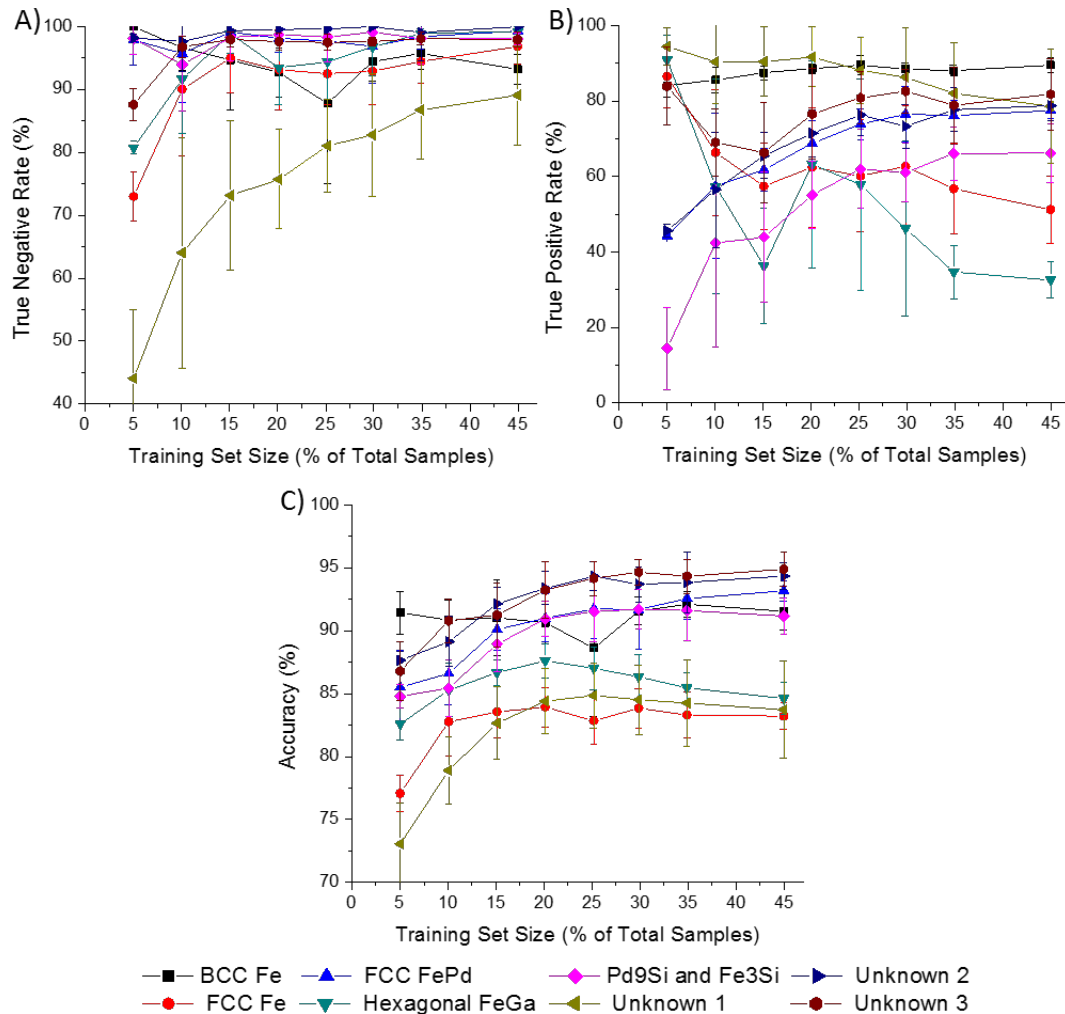
Figure 5.2 The A) true negative rate, B) true positive rate, and B) accuracy of SS-AutoPhase using different training set sizes. The predictions using each training set size were repeated 25 times, and the error bars are standard deviation in these repeated predictions.

5% to 10% of the total dataset. After this initial increase, R_{TN} does not significantly increase as the training set size increases. The initial increase followed by a constant R_{TN} for these phases indicates that the SS-AutoPhase is under trained for these phase when the training set consists of 5% of the total data, but has reached a maximum once 10% of the total data is used for training. R_{TN} of the Unknown 1 phase generally increases as the training set size increases, indicating that the training set size needs to contain many samples for SS-AutoPhase to properly exclude this

84

phase in patterns. Another significant feature of the R_{TN} phase is the large standard deviation in the classifier's negative predictive power for all training set sizes, being as large as $\pm\ 18\%$ when 10% of the data was used for training. This indicates that R_{TN} is highly sensitive to the K-means clustering selection of training data, which will strongly effect SS-AutoPhase's predictive power of this phase each time the classifier is trained.

Fig. 5.2 B) shows that there are three general trends in the average true positive rate R_{TP} for each crystal phase. The first trend is seen in the R_{TP} for the BCC Fe and Unknown 1 crystal phases, which stayed the statisticaly the same within 87.5% and 91.6%, respectively. This trend indicates that the classifier has reached a likely maximum of positive prediction capability for these phases even with a small training set size. The second trend is general increase in the R_{TP} as the training set size increases, seen by the increase from 44.2%-77.5% for FCC FePd, 14.4%-66.3% for Pd_9Si/Fe_3Si, and 45.6%-78.8% for Unknown 2. This trend shows that positive predictive capability (i.e. ability to correctly identify when a phase exists) becomes better trained as the training set size increases. In the last general is seen in seen in FCC Fe, Hexagonal FeGa, and Unknown 3. For these phases, R_{TP} decreases as the training set size increases from 5% to 15%, and then increases as training set increases from 15%-20%. After this initial common trend; FCC Fe and Hexagonal FeGa follow the second trend type where R_{TP} decreases from 62.5%-51.2% and 63.3%-32.6%, respectively. Unknown 3 is unlike FCC Fe and Hexagonal FeGa, it follows the first trend type after the initial common trend, with R_{TP} increasing from 76.6%-81.8%.

A combined analysis of R_{TP} and R_{TN} is needed to explain this last trend. All of these phases share a stark initial increase in R_{TP}; which mirrors the stark initial decrease in R_{TN} of these phases. The combination of these trends indicates that when the training set size is small, SS-AutoPhase is too liberal when identifying that these phases are present in a diffraction pattern. This causes the R_{TP} to initially be high at

85

the cost of a low R_{TN} value. As the training set size is increased from 5% to 15%, the SS-AutoPhase classifier learns to be more restrictive when identifying the existence of these phases in the diffraction patterns, causing an increase in R_{TN} and a decrease R_{TP}. As the training set size grows past 15%, the classifier starts to represent the true performance of the classifier using the current training set selection method.

Fig. 5.2 C) shows that the average accuracy, R_{Ac}, ranged from 73.0% for the Unknown 1 phase to 91.5% for BCC Fe when the training set size was 5%. As the training set size was increased from 5% to 15%, the R_{Ac} of all phases either stayed statistically the same or showed an increase. When the training set size was 15% of the total data set, the minimum R_{Ac} increased to 82.6%, associated with the Unknown 1 phase, and the maximum R_{Ac} did not change significantly. As the number of training data sets increased from 15% to 45%, R_{Ac} did not significantly change for any of the phases. The overall trend in R_{Ac} shows that SS-AutoPhase is properly trained when the training set size is $\geq$ 15% of the total data set. The general R_{AC} more closely mirror the trends seen in R_{TN} than R_{TP}, showing that the dataset itself is negatively biased for most of the crystal phases. This negative bias is expected, as multiple minor species do not exists in the majority of data sets. A potential method of overcoming dataset bias when using SS-AutoPhase will be discussed in section 8.2 of the future works.

This analysis shows that SS-Autophase has the most difficulty identifying which patterns do not contain the Unknown 1 phase and when the patterns do contain the FCC Fe and Hexagonal FeGa phases. SS-AutoPhase had likely had difficulty identifying the patterns that did not contain the Unknown 1 phase because the major Unknown 1 peak at 41.48 2-θ aliases with a FCC FePd peak and a Unknown 3 peak and the minor 45.55 2-θ Unknown 1 peak aliases with the characteristic peak of Fe$_3$Si. The aliased peaks can be misinterpreted by the AdaBoost classifier, biasing it to label a pattern with the existence of Unknown 1, especially in patterns which contain both

86

FCC FePd and Fe$_3$Si. In fact, this double aliasing and a lack of distinct features previously caused phase misidentification during MST analysis and when performing MEPMA [63]. SS-AutoPhase had difficulty identifying patterns which contained the FCC Fe and Hexagonal FeGa phases because of large variations in the peak characteristics of these phase. In a significant number of diffraction patterns, the FCC peak has a very low intensity and the characteristic peak doublet of the Hexagonal FeGa appeared as a singular peak. The atypical appearance of the diffraction peaks in some of the diffraction patterns caused the AdaBoost classifier to not identify the presence of the phases in the patterns.

From the trends of R_{TP}, R_{TN}, R_{Ac}, it was determined that SS-AutPhase was sufficiently trained when the training set size was $\geq 15\%$ of the total data set. It should be noted that even though this training set size was adequate for both the current study and the previous NiAl BC study, a larger training set size may be necessary if a more complex data set is analyzed. Based on the trend analysis, it was determined that the number of repeats for each prediction would be increased from 25 to 100 and the training data set would contain 15% of the total data for the detailed investigation of the predicted phase diagram investigation. The number of repeats was increased because of the large standard deviations seen when only using 25 repeats, indicating that potential sampling errors would affect the results. A training data set size of 15% of the total data was chosen because this was the smallest training set when R_{Ac} of all the phases did not significantly change.

Evaluation of Predicted Most Probable Phase Diagram

SS-AutoPhase predictions using a training set size of 15% of the total times were repeated 100 times. The results of these calculations were tabulated, and the number of times each phase was identified at each composition was determined. Fig. 5.3 shows the results for the Unknown 1 and Unknown 3 phases, and the rest are given in section

B.1 of the appendix. These two phases are shown here because they represent had the smallest and largest calculated accuracy during the training set size investigation.
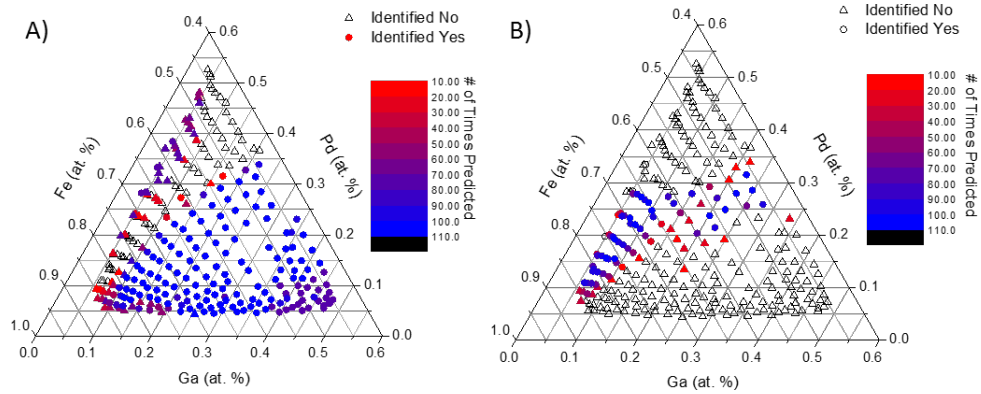
Figure 5.3 A) Unknown 1 phase predictions and B) Unknown 3 phase predictions. The data point shape indicates what the result from the MEPMA was; circle-identified as present, triangle-identified as not present. The data point color indicates the number of repeats that labeled a data point as containing the phase.

Fig. 5.3 A) shows that the existence of the Unknown 1 phase was correctly identified by SS-AutoPhase for the majority of the samples. The main area of the phase diagram where SS-AutoPhase identified the Unknown 1 phase and the MEPMA did not was in samples with <9.00 at.% Ga and between 25.0 at.% and 50.0 at.% Pd. Furthermore, SS-AutoPhase identified the existence of the Unknown 1 phase in samples surrounding the MEPMA Unknown 1 phase identification 10%-20% of the time, shown in red Fig. 5.3 A). As stated in the previous section, the presence of both FCC FePd and Fe_3Si phases in these samples mislead the AdaBoost classifier to identify this composition regime as containing the Unknown 1 phase. In contrast, the Unknown 3 phase was in very high agreement with the MEPMA throughout the entire phase diagram, as shown in Fig. 5.3 B).

A most probable phase diagram was created from the collection of all phase predictions. This diagram was constructed from a set of binary decisions of the likely phase predictions. For these binary decisions, it was determined that a pattern was most likely labeled with a phase if it was predicted for 50 or more of the repeats.

88

This process was performed for each phase, and was compared to the phase diagram created by the MEPMA, as shown in Fig. 5.4.
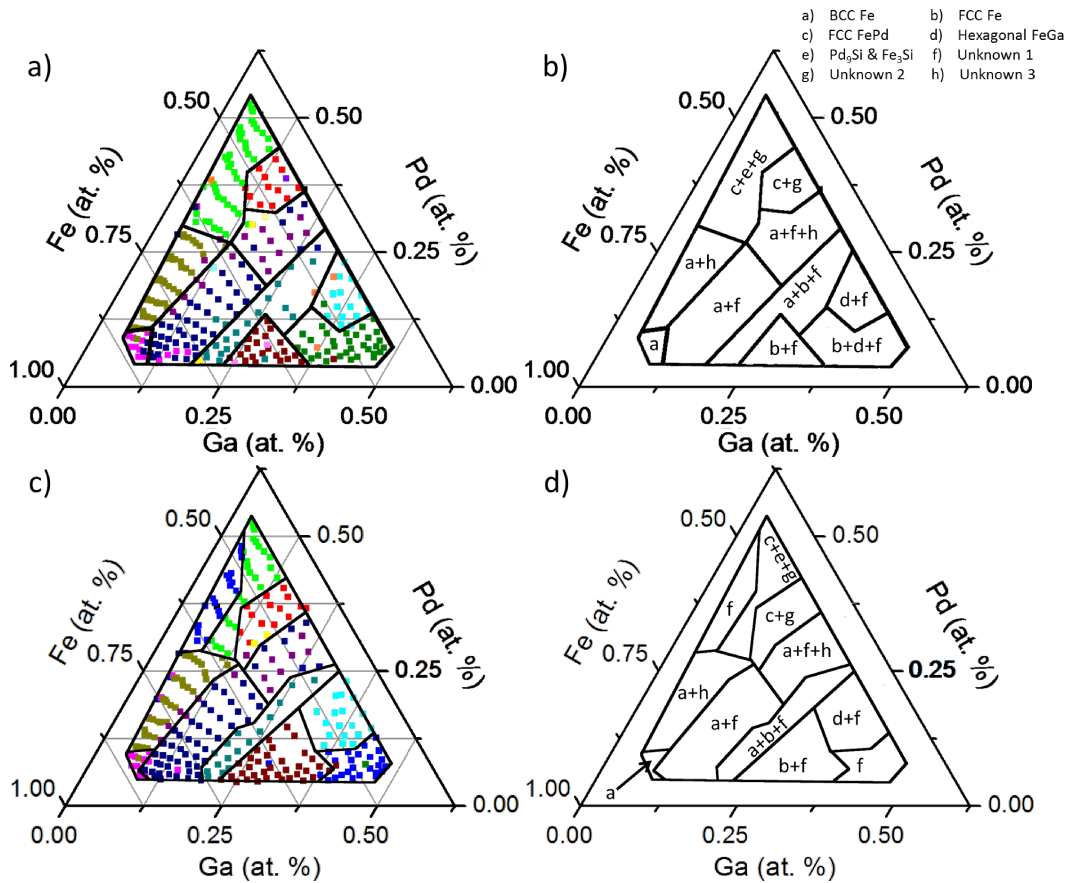
Figure 5.4   The phase diagram constructed from manual expert phase mapping analysis, shown in A) and B), and the selection of the most probable predicted phases from SS-AutoPhase, shown in C) and D). The phase diagrams shown in A) and C) are the full phase predictions of each point, legend not included due to complexity. The phase diagrams of B) and D) are simplified representations of A) and C) for clarity.

Fig. 5.4 B) and D) indicate that SS-AutoPhase made accurate phase predictions for the majority of the phase diagram. The area of the phase diagrams where SS-AutoPhase and MEPMA disagree are for the previously stated samples with <9.00 at.% Ga and between 25.0 at.% and 50.0 at.% Pd, and for samples with ≥ 35.7 at.% Ga. SS-AutoPhase failed to predict the presence of the FCC Fe and Hexagonal FeGa phases. As stated in the previous section, the appearance atypical low intensity FCC

peaks and singular peak Hexagonal FeGa peaks caused SS-AutoPhase to not label
samples in this composition regime with either of these phases.

Comparative Analysis of SS-AutoPhase to Common Clustering Techniques

A complete cross-comparison of the performance of SS-AutoPhase, HCA, MST, and
NMF to MEPMA was performed. The phase predictions of HCA and MST are given
in Fig. 5.5, and the NMF predictions can be found in Ref. [69].
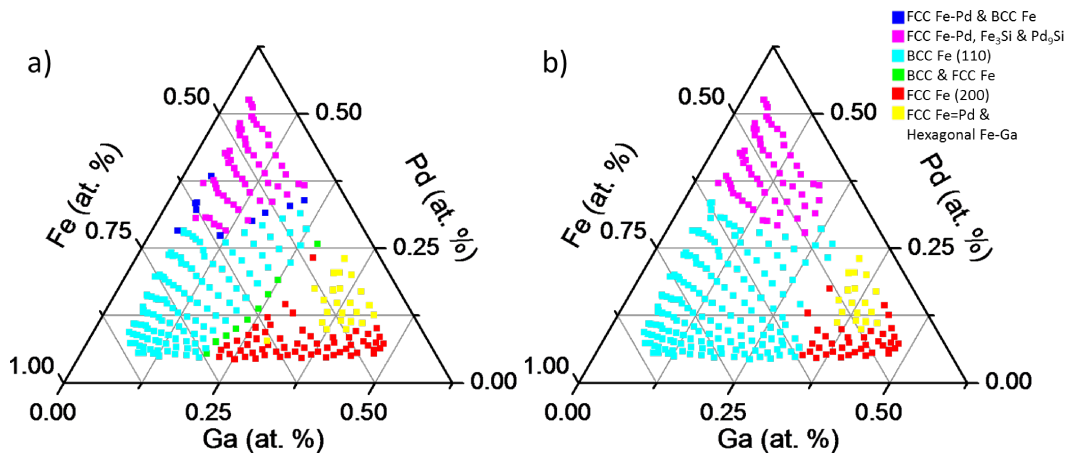
Figure 5.5   The phase diagram constructed from HCA, shown in A), and guided
MST, shown in B). The guided MST used known binary phases to assist in cluster,
not shown. Results were recreated from Refs. [70] and [63].

One major difference between SS-AutoPhase and HCA, MST, and NMF is that
the presence of the Unknown 1, Unknown 2, and Unknown 3 phases were not reported
by the HCA and MST analysis, and that the Unknown 3 phase was not reported by
NMF. Although the specific crystal structures associated with the peaks of these
three phases have not yet been identified, the peaks from these phases cannot be
described by the other crystal species. Given that new phase discovery is a focus
of many HTE studies, the ability of SS-AutoPhase to discover all of these phases is
one of its major strengths. Another major difference between predictions from HCA

and MST to SS-AutoPhase and MEPMA is the extent of the composition region that contain Fe_3Si and Pd_9Si. Fig. 5.4 B) and D) show that both SS-AutoPhase and MEPMA has significantly smaller composition regime that contain Fe_3Si and Pd_9Si than the predictions of MST and HCA, shown in Fig. 5.5 A) and B). The cause of this difference is probably MST and HCA under-clustered the data, and limited assigning the Fe_3Si and Pd_9Si phases to a single cluster. MST differs from the other techniques in that it does not predict a phase region where both BCC and FCC Fe exists, and constrains the existence of the FCC Fe phase sample containing 30 at% Ga. All other techniques agree that FCC Fe exists in samples that have > 20 at.% Ga and < 13 at.% Pd. An overall analysis of these techniques shows that NMF and SS-AutoPhase have the fewest dissimilarities with the MEPMA.

Comparison between NMF, SS-AutoPhase, and MEPM shows that the phase maps from these three techniques are in very high agreement, barring he absence of the Unknown 3 phase in the NMF predictions. Two slight differences between the predictions of NMF and predictions from SS-AutoPhase and the MEPMA is the location of Fe_3Si and Pd_9Si phases, and the extent of samples containing the Unknown 1 phase. Unlike MST and HCA, NMF predicted a much more constrained composition regime for the existence of the Fe_3Si and Pd_9Si phase, limiting these phases to only exist in samples with < 5 at.% Ga. NMF also identified that the Unknown 1 phase existed almost exclusively in samples with > 25 at.% Ga. These differences could be due to NMF's inability to handle major peak shifting properly if a unique peak-shifted basis set is not determined [69].

5.4 Conclusions

A semi-supervised version machine learning algorithm, SS-AutoPhase, that is capable of performing automated phase mapping of diffraction and spectroscopic data was developed and validated on a "open" FeGaPd CCS thin-film sample dataset. SS-

91

AutoPhase uses a two stage approach to minimize the amount of human analysis and input required. In the first stage, representative datasets were selected via k-means clustering analysis; which were labeled by a human expert to create a training dataset. In the second stage, an AdaBoost classifier was trained using the labeled training dataset. The AdaBoost classifier evaluated the slope and peaks features of the datasets, and created an ensemble of weak classifiers based on these features. The trained AdaBoost classifier was then used to phase label the rest of the XRD samples. The effect of training set size and a detailed comparative analysis of the phase map produced by SS-AutoPhase, MST, HCA, and NMF was performed. The results from manual human phase mapping analysis of all of the XRD patterns was used as a base truth for these analyses.

The investigation of the effect of training data set size revealed that the training dataset should contain $\geq 15\%$ of the total dataset to properly train SS-AutoPhase, having a minimum accuracy of 82.6% when 15% of the data was used for training. A most probable predicted phase diagram was then created by using 15% of the total data for training and repeating SS-AutoPhase predictions 100 times. The predicted most probable phase diagram was compared with the phase labels from HCA, MST, NMF, and the human expert. Overall, the comparison showed that NMF, SS-AutoPhase, and MEPMA were all in higher agreement with each other than with HCA and MST. One major difference between SS-AutoPhase and the other algorithmic approaches was the existence of an new unknown phase. The combination of high agreement between SS-AutoPhase and MEPMA and the identification of a previously unknown phase exhibited the robust nature of SS-AutoPhase to perform automatic phase labeling.

CHAPTER 6

FE-CR-AL AS AN OXIDATION RESISTANT NUCLEAR CLADDING COATING

6.1 MOTIVATION AND EXPERIMENTAL

Section 1.2 outlined how the oxidation of Zircaloy cladding materials from high temperature steam in nuclear reactors during a nuclear core meltdown, such as a cooling system failure, can lead to a disastrous hydrogen explosion in the reactor. This explosion can cause extensive structure damage to the nuclear containment structure, releasing radioactive materials to the surrounding environment, as was seen during the Fukushima Daiichi disaster. Two methods for mitigating the risks of such events is to either replace the current Zircaloy cladding with a high-temperature (1173 K) oxidation resistance material or to deposit a oxidation resistant layer on top of the current nuclear cladding assembly. Currently, many studies have focused on replacing Zircaloy with bulk Fe-Cr-Al, due to its ability to grow a passivating α-Al2O$_3$ layer [19, 24, 117].

While these Fe-Cr-Al materials have shown promise as a replacement material, the certification process for a complete replacement of current cladding is a lengthy process [32]. Such a process would ne shorter for the addition of oxidation resistant coatings. Successful application of such coatings rely on thorough investigations of the

---

Parts of chapter adapted from: J. K. Bunn, R. L. Fang, M. R. Albing, A. Mehta, M. J. Kramer, M. F. Besser, and J. R. Hattrick-Simpers, (2015). A high-throughput investigation of Fe-Cr-Al as a novel high-temperature coating for nuclear cladding materials. Nanotechnology, 26(27), 274003, with permission from ©IOP Publishing. See Fig. C.5 for copyright permission.

difference between the oxidation behavior of the Fe-Cr-Al in bulk versus thin-film. Such an investigation would need to cover potential meta-stable phase formation during synthesis, effect of alloy composition on corrosion behavior, and the effect of a large range of temperatures.

In this chapter, the details and results from a HTE investigation of CCS Fe-Cr-Al thin-film samples during high-temperature oxidation will be given [10]. Each part of the HTE framework described in chapters 3, 4, and 5 were used to rapidly synthesize, characterize, and analyze the samples. During this study, a two stage investigation of Fe-Cr-Al oxidation dynamics was performed. In the first stage, CCS Fe-Cr-Al samples are characterized with *in-situ* XRD at intermediate temperatures (420 K-690 K). In the second stage, the results from this first stage were used to deposit 8 compositionally focused samples. The oxidation dynamics of the 8 samples were characterized as the samples were cyclically heat treated at 1323 K for cumulative times of 5 min, 10 min, 30 min, 60 min, 120 min, 180 min, and 360 min.

In-Situ Intermediate Temperature Diffraction Studies

In the first stage of the investigation, *in-situ* diffraction intermediate temperature measurements of a Fe-Cr-Al CCS were taken to identify sample compositions that form a passivating α-Al_2O_3 layer. Compositions selected were based on previous studies of bulk Fe-Cr-Al alloys, which showed that alloys with 15 at.% - 23 at.% Cr, 3 at.% - 10 at.% Al, and balance Fe preferential oxidize to form a passivating α-Al_2O_3 [24, 26, 35, 77, 94, 103]. A series of power versus deposition rate calibration depositions were performed for DC sputtered Fe and RF sputtered Al and Cr. The sputter model described in chapter 3 determined a set of sputtering conditions that yielded the desired composition spread.

Before sputtering the CCS onto the 7.62 cm diameter Si wafer, a uniform 100 nm Ti film was deposited by rotating the substrate at 40 rpm during the deposition.
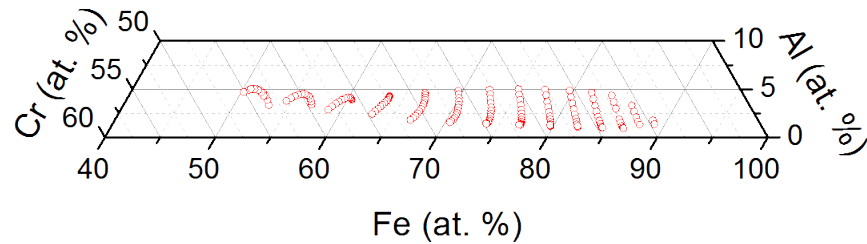
Figure 6.1   The compositions of the diffraction 178 points that were used throughout the *in-situ* intermediate temperature oxidation investigations of Fe-Cr-Al.

This Ti film was deposited to ensure that reaction between the substrate and the Fe-Cr-Al film would not occur during the intermediate temperature heat treatment of the film. After the Ti barrier layer deposition, elemental Fe, Al, and Cr were co-sputtered at 115 W DC, 25 W RF, and 85 W RF, respectively for 85 min in a 0.667 Pa Ar atmosphere. The resulting film was 500 nm thick and covered the composition spread from 0 at.% - 5 at.% Al, 10 at.% - 45 at.% Cr, and balance Fe, shown in Fig. 6.1. The composition of the film was validated using energy dispersive spectroscopy. The sample underwent a deposition anneal in the vacuum chamber at 572 K for 180 min to equilibrate the metallic phases in the film.

After the Fe-Cr-Al CCS sample was deposited on Si, a modified form of the HTE experimental methodology outlined in chapter 4 was performed. The sample was mounted to the sample holder/substrate heater at beam line 1-5 of the Stanford Linear Accelerator Center (SLAC). Details of the diffraction assembly at SLAC can be found in section 2.2. The x-ray source had a wavelength of 0.826 57 Å and was set to have an incident angle of 8° with respect to the sample. Before the sample was heated, diffraction patterns from 178 different points on the composition spread were taken to determine the as-deposited metallic phases. After the initial diffraction scan was completed, the Kapton dome discussed in section 2.2 was installed and industrial grade He (0.158 Pa O_2 partial pressure) was flown through the dome. The Kapton dome and He were used to prevent damage via oxidation failure of the

heating elements. Diffraction measurements at the previously stated 178 points were then taken as the sample was heated to 420 K, 483 K, 556 K, 626 K, and 690 K. Prior to each scan, the heater was ramped over 20 minutes and then the sample was held at temperature for 10 minutes to allow the sample to equilibrate before diffraction measurements began. After the sample equilibrated, the substrate stage was realigned to account for sample thermal expansion. Each set of diffraction scans, i.e. all 178 points, were taken over a 1 hour period. The set of diffraction measurements at 690 K were repeated over a second hour to investigate the temporal oxidation dynamics of the sample.

The 2D diffractions patterns were processed using the procedure outlined in section 2.2 with the WxDiff software package and a LaB_6 NIST standard. The resulting Q-I diffraction patterns were converted to 2-θ-I diffraction patterns using the wavelength of Cu K_α. A cubic-spline background subtraction was then performed on all the diffraction patterns, and the diffraction peaks were fitted using Voigt profiles to extract precise values of the relative intensities of the peaks.

Accelerated diffraction analysis was performed using both the HCA package of CombiView as well as the SS-AutoPhase semi-supervised algorithm outlined in chapter 5 [70]. The phase analysis from these diffraction measurements was used to identify compositional regions of the sample that showed similar oxidation behavior. Four different compositional regions with unique oxidation behavior were identified. The results from the oxidation region analysis was used to guide the second stage of the Fe-Cr-Al thin-film investigation.

Focused Cyclic High Temperature Raman Studies

During the second stage of the investigation, compositionally focused samples were deposited and charactered with Raman spectroscopy during cyclic heat treatments at 1323 K, referred to here as high temperature. In this stage of the investigation,

the same sputtering conditions used in the first stage of the investigation was also used to create compositionally targeted depositions of Fe-Cr-Al on a set of 8, 1.27 cm diameter sintered Al_2O_3 stubs. Al_2O_3 was used as the substrate instead of Si due to the relatively low melting point of Si and the high temperatures involved in this stage of the investigation. The composition of Fe-Cr-Al deposited on each Al_2O_3 token was controlled by placing the tokens on model-predicted locations of the sputtering chamber substrate holder during deposition. Ti was sputtered onto the tokens before depositing Fe-Cr-Al to act as an adhesion layer between the Fe-Cr-Al film and the Al_2O_3 tokens.

After deposition, the samples were cyclically heat treated for cumulative times of 5 min, 10 min, 30 min, 60 min, 120 min, 180 min, and 360 min and air quenched using the procedure outlined in chapter 4 for the investigation of NiAl BCs. The samples were characterized with Raman/fluorescence spectroscopy using the 632.8 nm red laser. During these measurements, the Ti adhesion layer had secondary purposes. First, it acted as an indicator for film spallation, as Ti oxide Raman peaks would be observed if significant film spall occurred. Second, it blocked any fluorescence/Raman signal from the substrate from effecting the sample characterization.

6.2 Results and Discussion

In-Situ Intermediate Temperature Diffraction Studies

Fig. 6.2 shows representative diffraction patterns from the as-deposited and 690 K annealed Fe-Cr-Al film . Fig. 6.2 A) shows the presence of diffraction peaks at 44.1° 2-θ and 64.6° 2-θ consistent with Fe-Cr-Al[18], a (100) textured Ti peak[6] at 34.7° 2-θ (JCPDF#89-2762), and a peak at 38.24° 2-θ consistent with Cr crystal phases (JCPDF#65-3316), in the as-deposited sample. The absolute 2-θ location of the Fe-Cr-Al diffraction peaks shift slightly across the samples as the peak location depends

97

www.manaraa.com

on the composition of the film, as stated in section 2.2. Only samples with a Cr content in excess of 40.2 at.% exhibited the Cr diffraction peak. The existence of the Cr phase at high Cr content is due to limited solubility of Cr in the Fe-Cr-Al alloy at room temperature.
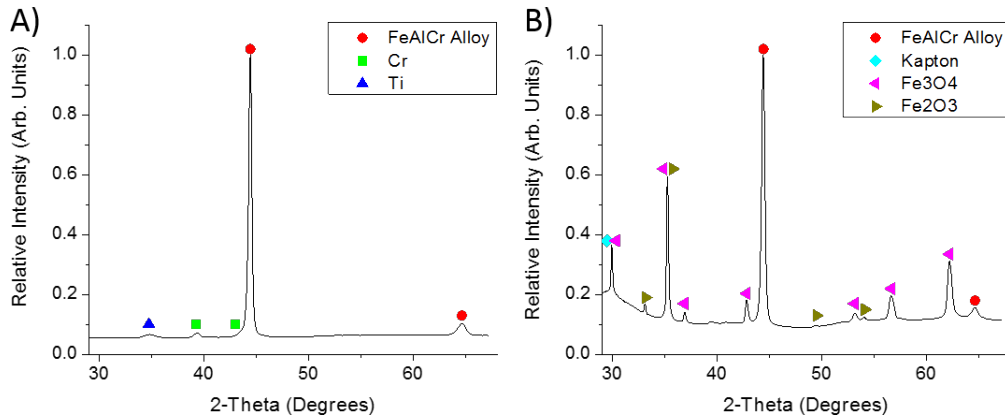
Figure 6.2   Representative diffraction patterns from A) a as-deposited Fe-Cr-Al sample and B) an oxidized Fe-Cr-Al sample. The diffraction pattern in B) is after the sample was heat treated at 690 K. Both patterns are normalized to the Fe-Cr-Al alloy phase peak at 44.1 ° 2-θ.

Fig. 6.2 B) shows that the oxidized samples typically exhibited diffraction peaks at 29.9° 2-θ. 35.2° 2-θ, 42.8° 2-θ, and 62.2° 2-θ indicative of stressed Fe_3O_4 (JCPDF#86-1353), peaks at 33.2° 2-θ, 35.6° 2-θ, and 44.5° 2-θ indicative of Fe_2O_3 (JCPDF#33-0664), as well as the Fe-Cr-Al alloy peak. Additionally, a broad peak located at 35° 2-θ due to reflection of the x-rays off the Kapton dome were also present. The 2-θ location of the Kapton dome background peak shifted significantly depending on the sample position because of changes to the angle of incidence between the x-rays and the dome. During the higher temperature diffraction measurements, the Kapton dome peak aliased with the 29.9° 2-θ Fe_3O_4 peak and the 33.2° 2-θ Fe_2O_3 peak, altering the absolute intensity of these peaks slightly during the diffraction analysis. Diffraction from neither Cr nor Al oxides were observed in any of the intermediate temperature diffraction measurements.

After the diffractions pattern were background subtracted, the intensities of each diffraction pattern was normalized using against the Fe-Cr-Al peak by using the following equation:

$$N\left(2\theta\right) = \frac{I\left(2\theta\right)}{I_{Fe-Cr-Al}} \tag{6.1}$$

Where $N\left(2\theta\right)$ is the normalized intensity of the diffraction at 2-θ, $I\left(2\theta\right)$ is the background subtracted intensity of the diffraction at 2-θ, and $I_{Fe-Cr-Al}$ was the intensity of the Fe-Cr-Al peak from the Voigt peak fitting of the diffraction pattern. This normalization was performed so that qualitative comparative analysis of the amount of the different crystal species in the diffraction patterns could be performed. The Fe-Cr-Al peak was chosen for this normalization as it was the highest intensity peak of each diffraction pattern and did not alias with the other crystal phases or the Kapton background. It should be noted that care must be taken when interpreting the results of this normalization as secondary effects, such as grain growth, could create compositionally sensitive artifacts.

Analysis of the diffraction from as-deposited and 420 K annealed sample showed no signs of observable oxides. As the sample was heated to 420 K from room temperature, the existence of the Cr diffraction peak vanished for samples with Cr content in excess of 43.5 at.%. This indicates that as the sample was heated, Cr phase was absorbed into the Fe-Cr-Al alloy due to the increased solubility of Cr. A more detailed discussion of the Cr phase dynamics can be found in Ref. [10].

As the sample was raised to 556 K, the sample formed a relatively uniform Fe_3O_4 across all compositions, as shown in Fig. 6.3 A). Fig. 6.3 shows the relative intensity of the 62.1° 2-θ Fe_3O_4 peak as a function of composition. The 62.1° 2-θ peak was chosen for analysis as it is the most intense Fe_3O_4 peak and did not alias with alias with the other crystal phases or the Kapton background. The uniform Fe_3O_4 relative intensity indicates that no composition of the sample was preferentially oxidized at these temperatures.

99
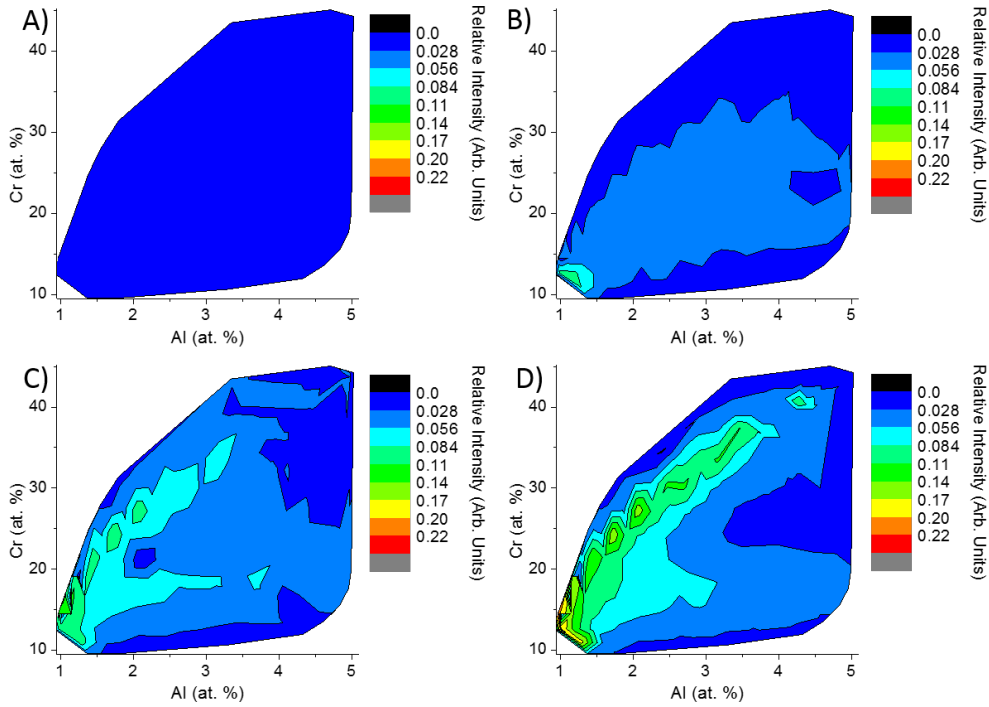
Figure 6.3   The relative intensities of the 62.1° 2-θ Fe$_3$O$_4$ diffraction when the sample was heated to A) 556 K, B) 626 K, C) 690 K for the first set of measurements and D) 690 K for the second set of measurements. All diffraction peak intensities were determined by fitting the background subtracted peaks with a Voigt profile.

Continued and preferential oxidation of the sample was observed when the sample was heated to 626 K. This is shown by the increase in the relative intensity of the Fe$_3$O$_4$ throughout samples with > 62 at.% Fe, shown in Fig. 6.3 B). Diffraction from Fe$_2$O$_3$ was also observed in samples with a Cr:Al ratio greater than ten, as shown by Fig 6.4 A). Fig. 6.4 shows the relative intensity of the 33.2° 2-θ Fe$_2$O$_3$ diffraction peaks. This Fe$_2$O$_3$ peak was chosen because it was the highest intensity peak for Fe$_2$O$_3$.

At 690 K, the diffraction peak intensities from both Fe$_3$O$_4$ and Fe$_2$O$_3$ in samples with more than 3.08 at.% Al remained fairly constant, shown in Fig. 6.3 C) and Fig. 6.4 B), respectively. Samples with lower Al concentration showed continued growth of Fe$_3$O$_4$ and Fe$_2$O$_3$, indicated by the increase of the relative intensity of these oxides

100
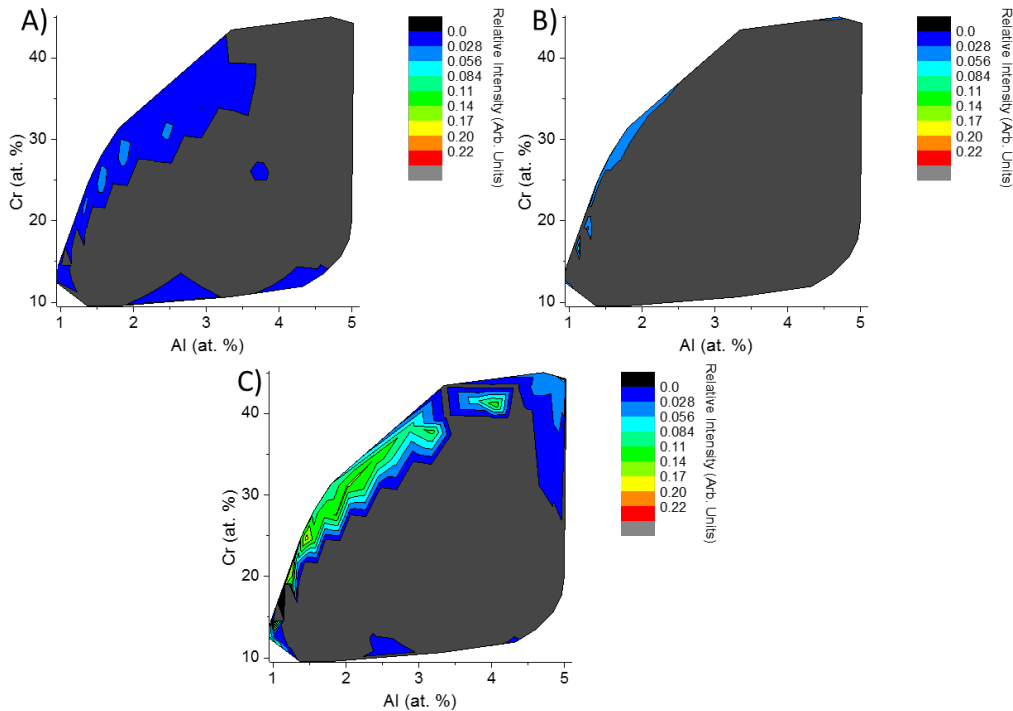
Figure 6.4   The relative intensities of the 33.2° 2-θ Fe$_2$O$_3$ diffraction when the sample was heated to A) 556 K, B) 626 K, C) 690 K for the first set of measurements and D) 690 K for the second set of measurements. All diffraction peak intensities were determined by fitting the background subtracted peaks with a Voigt profile.

in these samples. It should be noted that the Kapton background aliased with the Fe$_2$O$_3$ in this sample, limiting the amount of analysis that could be performed. This analysis of the initial oxidation of the CCS sample at 690 K suggests that samples > 3.08 at.% Al are sufficient to provide oxidation resistance at these temperatures.

In the second set of diffraction measurements at 690 K, further Fe oxidation was observed as shown by Fig. 6.3 D) and Fig. 6.4 C). The Fe$_3$O$_4$ peak intensities increased across the entire sample except for samples containing > 3.08 at.% Al and 20.0 at.% - 32.9 at.% Cr. The intensity of the Fe$_2$O$_3$ also increased, but existed in the same composition region that it was observed to exists during the 626 K diffraction measurements.

Overall, the oxidation resistance of samples containing > 3.08 at.% Al and 20.0

at.% - 32.9 at.% Cr agrees well with previous bulk oxidation studies of Fe-Cr-Al alloys, which identified oxidation resistance in bulk alloys containing 3-10 at.% Al and 15-23 at.%. The only significant difference between this thin-study and the previous studies is that the amount of allowable amount of Cr in the thin-film samples was a little higher than in the bulk samples. This could be due to incorporation of other alloying constituents and alloy processing, which can alter the absolute range of oxidation resistance of such alloys.

Focused Cyclic High Temperature Raman Studies

An "oxide phase diagram" was created from the results of the intermediate temperature diffraction investigations, as shown in Fig. 6.5. Further investigation of the alloy performance from these regions at 1323 K was performed by depositing 8 Fe-Cr-Al samples on Al_2O_3 stubs. The samples were then cyclically heated at 1323 K, and characterized using Raman spectroscopy. The composition of each of these samples is indicated in Fig. 6.5 with a star or square. For the sake of brevity, only the samples that exhibited the most α-Al_2O_3, labeled with stars in Fig. 6.5 will be discussed in detail here. These samples were chosen because in this manner, a "best case" comparison of each of the regions was made. Analysis of the samples labeled with squares can be found in Ref. [10]. After the Raman measurements were taken, a cubic spline background subtraction was performed on the resulting Raman spectra.

Fig. 6.6 show the Raman spectra of the representative sample from each region after each cyclic heat treatment. No spectra are given for the as-deposited sample because no observable oxides had formed. The Raman data showed peaks indicative of Fe_3O_4 at 302 cm^{-1}, 514 cm^{-1}, 534 cm^{-1}, and 663 cm^{-1} Raman shift and Fe_2O_3 at 227 cm^{-1}, 246 cm^{-1}, 293 cm^{-1}, 412 cm^{-1}, 498 cm^{-1}, 610 cm^{-1}, and 1332 cm^{-1} Raman shift [18]. α-Al_2O_3 fluorescence peaks were also observed at 1370.4 and 1400.4 cm^{-1} Raman shift. Unlike the Raman/fluorescence measurements in the NiAl BCs

102
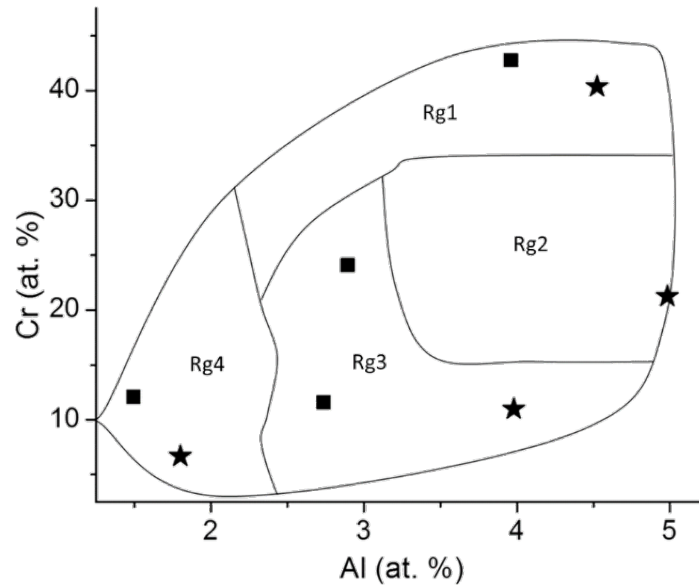
Figure 6.5   A diagram showing the four regions that exhibited different oxidation behavior during the *in-situ* intermediate temperature oxidation investigation. Region 1 (Rg1) - major Fe_2O_3 growth, Region 2 (Rg2) - suppressed oxidation, Region 3 (Rg3) - moderate Fe_3O_4 growth, and Region 4 (Rg4) - major Fe_3O_4 growth. The squares and stars represent the composition of the samples deposited for the cyclic high-temperature oxidation investigation.

study of chapter 4, the Fe-Cr-Al Raman spectra were not transformed to absolute wavelength and are stated in Raman shift since both Raman and fluorescence peaks are present and resolvable. None of the Raman spectra showed peaks at 396 cm^{-1}, 515 cm^{-1}, and 638 cm^{-1} Raman shift indicative of anatase titania or at 439 cm^{-1}, 611 cm^{-1}, and 805 cm^{-1} Raman shift indicative of rutile titania [68]. The absence of any titania peaks indicates that complete failure of the Fe-Cr-Al films did not occur during this investigation.

Similar to the diffraction patterns in the intermediate temperature *in-situ* investigation, each Raman spectra was normalized to the 610 cm^{-1} Fe_3O_4 Raman peak. This peak was chosen because it was present in all spectra. The representative sample from Rg1, shown in Fig. 6.6 A), shows that Fe_3O_4 was the major oxide that was formed from the 5 minute to the 120 minute heat treatment. In the 180 minute Raman
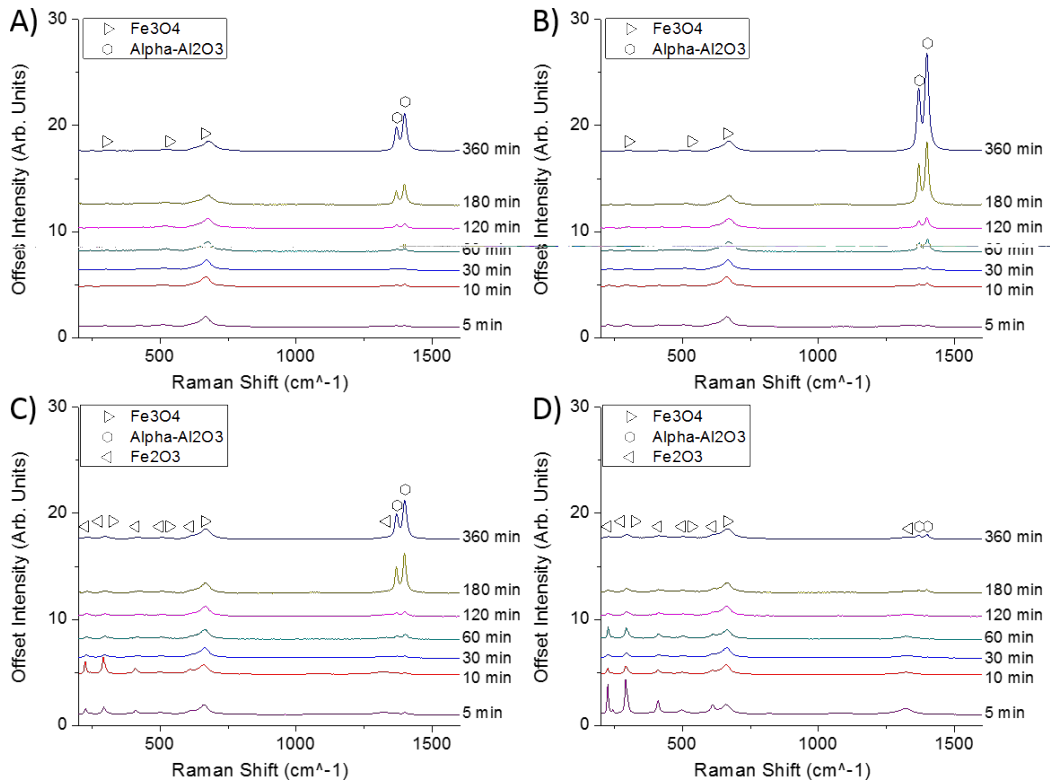
Figure 6.6 The Raman spectra of the representative sample from A) Rg1, B) Rg2, C) Rg3, and D) Rg4 with respect to cumulative time that the sample was heated at 1323 K. All Raman spectra are normalized to the Fe_3O_4 Raman active peak located at 610 cm^{-1} Raman shift.

spectrum, a moderate intensity α-Al_2O_3 peak forms, which increases significantly in intensity after heat treatment for 360 minutes . This shows that a significant amount of α-Al_2O_3 forms after 120 minutes, and continues to form. The α-Al_2O_3 likely forms after Fe has been depleted from the surface of the thin-film due to oxidation, causing an excess of Al in the surface of the film.

Rg2, shown in Fig. 6.6 B) shows that initially the sample oxidized to form Fe_3O_4. Fe_3O_4 was the only major oxide that was detected by Raman until the sample was heat treated for 60 minutes. The sample that was heat treated for 60 minutes exhibited moderate intensity α-Al_2O_3 peaks. These peaks increase significantly in all heat treatments after 60 minutes, up to the last 360 min heat treatment. In the 360 minute heat treated sample, the main α-Al_2O_3 reaches a relative intensity of 9.28,

104

indicating strong α-Al_2O_3 growth on the surface of the film. This strong growth of α-Al_2O_3 further supports that alloys in this region create a passivating oxide, and are promising candidate as high-temperature oxidation resistant coatings.

The Rg3 sample, shown in Fig. 6.6 C) exhibited major Fe_2O_3 peaks in the 5 and 10 min heat treatment as shown in figure 6(C). After 30 minutes of heat treatment, the Fe_2O_3 peaks significantly reduce in relative intensity compared to Fe_3O_4, potentially due to either Fe_2O_3 spallation or a disproportional growth of Fe_3O_4 during the heat treatment. After 30 minutes of heat treatment, the oxidation dynamics of the Rg3 sample are similar to the Rg1 sample, where α-Al_2O_3 peaks of similar intensity appear after the 180 and increase in intensity after 360 min of heat treatment.

Rg4 shows very high very intensity Fe_2O_3 peaks exist in the sample after the 5 min heat treatment, as shown in Fig. 6.6. These peaks significantly decrease after 10 minutes of heat treatment, and reach similar relative intensities to the Rg3 sample after 120 minutes of heat treatment. Unlike the other regions, the Rg4 samples does not exhibit major α-Al_2O_3 peaks appear throughout the heat treatments of this region. At most, a moderate intensity α-Al_2O_3 forms after the sample undergoes 360 minutes of heat treatment. This shows that of all the regions identified, Rg4 is the least likely region to form a passivating oxide, and should not be used as a oxidation resistant coating.

Comparison of the results from the cyclic high-temperature heat treatment study to the *in-situ* intermediate temperature study show that overall the results of these two studies agree. Samples in Rg2 of both studies showed the best oxidation resistance, while samples in Rg4 showed rapid and extensive Fe oxidation. The two separate studies do disagree slightly on the relative amount of Fe_2O_3 and Fe_3O_4 that form in Rg1 and Rg3, but these differences could be due to the major temperature and heating time differences of the two studies as well as differences in probe depth of Raman and XRD.

105

6.3 Conclusions

The HTE framework developed in chapters 3, 4, and 5 was applied to investigate the potential for Fe-Cr-Al thin-films to be used high-temperature oxidation-resistant coatings for nuclear cladding materials. The study used a 2-stage investigation of the oxidation dynamics of Fe-Cr-Al alloys. In the first stage, an *in-situ* diffraction study was performed on a sputtered CCS Fe-Cr-Al sample at temperatures ranging from 420 K to 690 K. Four separate distinct composition regions were identified that showed different oxidation dynamics. The results of this study showed that samples containing > 3.08 at.% Al and 20.0 at.% - 32.9 at.% Cr, balance Fe showed suppressed oxidation.

In the second stage of the investigation, 8 compositional focused Fe-Cr-Al samples were cyclic heat treated at 1323 K for times ranging from 5 to 360 minutes. The compositions of the samples were selected to range the four previously identified compositions regions. Raman spectroscopy was used to characterize the sample and identify the different oxides that formed after each heat treatment cycle. The study further confirmed the conclusion that samples with > 3.08 at.% Al, 20.0 at.% - 32.9 at.% Cr, and balance Fe are strong potential candidates as high-temperature oxidation resistance for nuclear cladding materials. Samples in this region showed strong α-Al$_2$O$_3$ growth was observed after 60 minutes, 120 minutes faster than samples in the other compositional regions. The other compositional regions showed significant Fe oxide growth, with the most Fe-heavy samples having the worst oxidation resistance. The results from this study agree strongly with previous bulk studies of Fe-Cr-Al resistance, which have shown that bulk alloys containing 3-10 at.% Al, 15-23 at.%, balance Fe have strong high-temperature resistance.

CHAPTER 7

CRYSTAL PHASE STABILITY OF SCSZ AND BYC AS INTERMEDIATE TEMPERATURE SOFC ELECTROLYTES

7.1 OVERVIEW

Section 1.2 outlined the operation of SOFCs and the function of the three major part of the SOFC assembly. It also detailed the need for the development of intermediate temperature electrolyte materials, that will have a high ionic conductivities between 773 K - 1023 K. These intermediate temperature electrolyte materials could vastly lower the operating temperature of SOFCs, reducing the overall operational cost of such devices [8, 57]. Previously, two separate methods of increasing SOFC electrolyte ionic conductivities have been proposed. The first method is to replace the current YSZ electrolyte material, which has high oxygen ion resistance at temperatures lower than 1123 K, with materials whose ionic conductivity is higher in the intermediate temperature range, such as ScSZ or BYC [80, 109, 110, 128]. The second method is to reduce the thickness of the electrolyte layer from the 10s-100s of microns to < 500 nm, shortening the total diffusion length of the oxygen anions as they travel travel through the electrolyte. One synthesis approach that could be used to deposit thin-film SOFC electrolyte materials is magnetron sputtering. This PVD technique is capable of depositing multiple classes of materials, such as oxides, nitrides, and metals, and can controllably deposit dense and continuous thin-films with thicknesses much less than 500 nm [2, 59].

In this chapter, the details of two separate HTE evaluations of magnetron sput-

tered SOFC electrolye materials will be given. In the first half of the chapter, the details of an investigation of the effect of magnetron sputtering synthesis conditions and post-processing on the crystallinity and crystal phase of ScSZ thin-films will be given. In the second half of the chapter, the details of a preliminary investigation on the effect of BYC composition on the deposited BYC phase and the thermal stability of the crystal phases will be given. Both of these investigation utilized the tools developed in 3, 4, and 5, to accelerate the exploration of these materials.

7.2   ScSZ Motivation and Experimental

Scandia-stabilized zirconia (ScSZ) has gained recent attention as an alternative solid electrolyte material. Previous studies have shown that it has a oxygen ion conductivity of 0.30 S/cm at 1073 K, more than twice that of YSZ at that temperature. They have also shown that the highly ionic conductivity cubic phase of ScSZ is stable for 10 - 13 mol.% Sc_2O_3 doping into ZrO_2 [136]. As stated in the previous section, this ionic conductivity could be further increased by creating a thin-film ScSZ electrolyte, but traditional synthesis methods, such as the ceramic method and screen printing, cannot easily make such thin materials. These technique create highly defected films, with small pinholes or cracks, when films thickness is less than 1 micron [71].

As stated previously, magnetron sputtering could be used to synthesize relatively defect free thin-films. One potential obstacle for ScSZ thin films is the formation of an undesired meta-stable phased during deposition, as seen in chapter 4, due to the high energy particles used in sputtering. This is an especially large concern because ScSZ is known to form a rhombohedral phase at temperatures in excess of 1372 K, which has a much smaller ionic conductivity then the cubic ScSZ phase [136]. As the particle energy of the depositing atoms is a function of sputtering condition, this issue could be overcome by identifying sputtering conditions in which a stable cubic ScSZ phase is deposited.

Here, the details of an investigation on the effect of sputtering deposition condition and sample post processing on the crystal phase and crystallinity of sputtered 30 nm ScSZ films will be given. In this investigation, the developed HTE tools and a 3-factor, 4-level full factorial design was used to synthesize, process, and characterize multiple ScSZ thin-films. The crystal phase, crystallinity, and the crystal texture of the as-deposited and processed films were characterized using 2D XRD.

Thin-films were synthesized by RF sputtering an 11 mol.% Sc_2O_3 ScSZ target onto 7.62 cm by 2.54 cm single crystal Si substrates. Each sample was deposited via a permutation of the low, medium, and high factor levels of gun power, oxygen concentration, and deposition temperature shown in Table 7.1. 23 of the 27 possible permeations of samples conditions were deposited in this manner, with the 4 excluded permeations being the 35 W depositions in the presence of 5 vol.% and 10 vol.% oxygen at 773 K and 923 K. These four deposition were excluded due to prohibitively long deposition times (< 0.1 Å/min). Due to the high temperatures used in this investigation, silver paste was used to mount the samples to the sample holder before each deposition. Film thickness for all samples was measured to be 30.24 ± 2.80 nm via reflectometry. Once all deposition were complete, each wafer was cut into three 2.54 cm by 2.54 cm squares. One of these wafers from each set was not annealed, one was annealed at 1273 K for 4 hours, and the last was annealed for 1273 K for 8 hours. The post anneal temperature was selected as it represents a likely temperature that the electrolyte will be subjected to during deposition/processing of the cathode or anode.

After all films were deposited and processed, the samples were characterized using the SAXSLAB Ganesha 200 XL small angle/wide angle diffraction system described in section 2.2. The resulting 2D diffraction patterns were analyzed to gain information about the crystallinity and crystal texture of the films. They were also converted to 2θ-I diffraction plots, which were analyzed to determine the crystal phase of each

Table 7.1   The levels and values of deposition parameters and annealing times used to synthesize samples. *Annealing temperature was 1273 K.

Factor Level	Gun Power (W)	O_2 Concentration (vol.%)	Deposition Temperature (K)	Annealing Time* hrs
Low	35	0	298	0
Medium	50	5	773	4
High	65	10	923	8

sample and to assist in crystallinity analysis. See section 2.2 for details about how the 2D and 2θ-I patterns can be related to the different aspects of a crystal phase A Zeiss Ultraplus Thermal Field Emission SEM using a 10 keV beam intensity, 4.6 nm working distance, and a secondary electron detector was used to quantify the crystal grain growth after the annealing procedure and to ensure that the films were continuous and uniform (i.e. absence of cracks and lack of delamination/spallation).

7.3   ScSZ Results and Discussion

The diffraction patterns from each sample showed diffraction peaks located at 30.0° 2-θ, 34.5 ° 2-θ, and 48.9° 2-θ, as shown in Fig. 7.1, which are indicative of the (111), (200), and (220) cubic ScSZ crystal planes, respectively [99]. Furthermore, no diffraction peaks associated with secondary phases were observed in any of the samples. These results indicate that the formation of cubic ScSZ phase is insensitive to the sputtering deposition conditions covered by the factorial design and that the crystals are thermally stable up to 1273 K. Analysis of the cubic ScSZ peak location as a function of annealing time showed that all peaks shifted by $\sim 0.5°$ 2-θ between for every set of as-deposited samples and annealed samples. Fig. 7.1 shows this shift in the 50 W sample that was deposited without oxygen in the chamber. Note that only the 2θ-I diffraction pattern of this sample are shown here for the sake of clarity. The observed peak shift indicates that the crystals expanded upon annealing.

110

This expansion is likely due to the fact that the sputtered ScSZ films were oxygen deficient, and upon annealing the oxygen in the surrounding air replaced the defect sites in the crystal lattice, forming a stoichiometric ScSZ. The deposition of oxygen deficient oxides when using sputtering is a well-known phenomena [98].
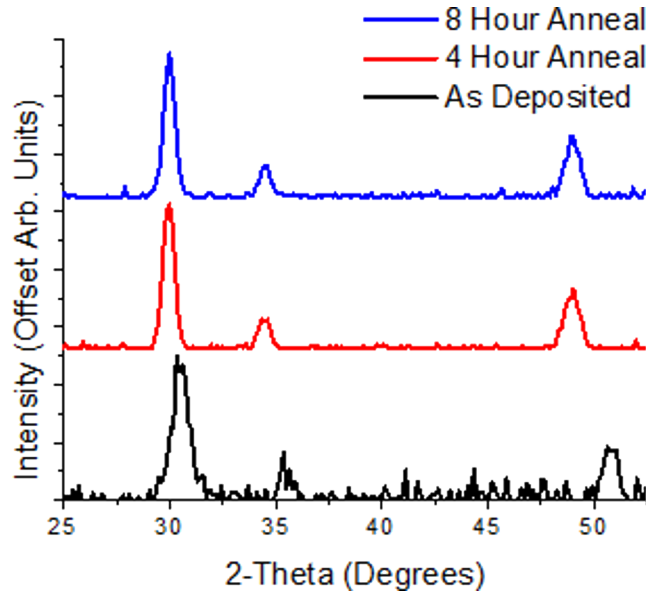
Figure 7.1   XRD patterns of the ScSZ samples deposited at 50 W, 0 vol% O_2, and 298 K. The diffraction patterns shows that independent of annealing time, the only crystal phase that was detected by XRD was the desired cubic phase.

A combined analysis of diffraction peak shape from the 2θ-I and the 2D diffraction patterns was performed to determine the crystallinity of each sample. From this analysis, each sample was determined to be either near randomly oriented crystals (here referred to as disordered), be slightly-textured, or be moderately-textured based on the peak shape in the 2D XRD and 2θ-I diffraction patterns. See section 2.2 for an explanation of how diffraction peak shape relates to crystal texture. Fig. 7.2, shows the results of this crystallinity analysis for all samples.

Fig. 7.2 shows that independent of sputtering power and oxygen concentration, all the as-deposited samples synthesized at 298 K were disordered. Upon annealing, the diffraction peaks associated with these samples become more defined, and the
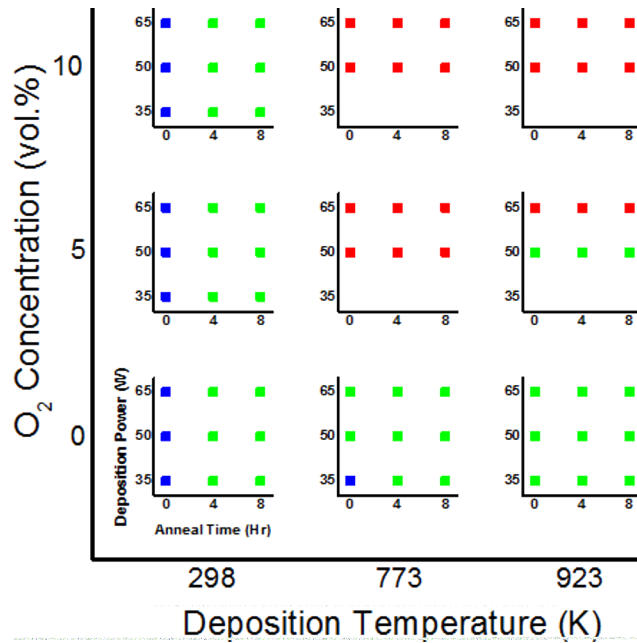
Figure 7.2   The results of the crystallinity analysis from all of the ScSZ sample. Each sample was determined to have disordered crystals (blue squares), slightly textured crystals (green squares), or moderately textured crystals (red squares).

crystals go from disordered to slightly textured. This is an expected trend due to the potential oxygen inclusion into the cubic lattice and grain growth. The sample that was deposited with 35 W power at 773 K also showed this behavior. The fact that all the "low energy" (i.e. low power and low substrate temperature) samples expressed this trend shows that when depositing with a low energy, the as-deposited crystals do not have enough energy to form an ordered structure.

Analysis of the 773 K and 923 K depositions with no oxygen (right two dataset on the bottom row of Fig. 7.2) showed that independent of deposition power and annealing, the films contained slightly-textured cubic ScSZ crystals. This trend implies that without the inclusion of O_2 during deposition, a slightly ordered crystal stucture was deposited, and that the current annealing procedure was either too short or too low energy for a moderately ordered structure to form.

Analysis of the higher temperature, 773 K and 923 K, higher O_2 concentration,

5 vol.% and 10 vol.% depositions showed that moderately textured crystals were deposited. This moderate texture persisted throughout the annealing procedure. The formation of moderately textured crystals during the higher temperatures, higher O_2 concentration depositions implies that a combination of both of these factors is necessary to form a moderately ordered crystal structure. This is most likely because there was an increased energy at the substrate surface due to the higher temperature and the reduction of the oxygen deficiencies in the crystals that formed due to the inclusion of O_2 lowered. The higher temperature, higher O_2 depositions resulted in textured growth potentially because the higher particle energies allowed the deposited particles diffuse and attain thermodynamically favorable crystal growth, while the increased oxygen concentration decreased the oxygen vacancies defects in the crystals that were grown, allowing for more ordered crystals to grow.

Previous studies have shown that the oxygen ion conductivity of an electrolyte can increase if the electrolyte is textured [58, 106]. From the crystallinity analysis, the degree of sample texture was qualitatively defined. A more quantitative analysis of the degree of texturing of these films was performed by calculating the ratio of the (111) to (220) peak intensities of each film. These peak intensities were determined by fitting each background subtracted peak with a Voigt profile. Fig. 7.3 shows the results from these calculations. Four samples were removed from Fig. 7.3; the 50 W, 5 vol.% O_2 773 K, 4 hr annealed sample, the 65 W, 5 vol.% O_2, 773 K, 4 hr and 8 hr annealed samples, and the 65 W, 10 vol.%, 773 K, 4 hr annealed sample because they showed signs of silver paste contamination, leading to inaccurate texture calculation on these films.

The as-deposited thin-films deposited in 0 vol.% or 5 vol.% O_2 atmosphere became more (111) as they were annealed for 4 hrs, shown in Fig. 7.3. The degree of (111) texturing of these 4 hr annealed samples decrease as they were annealed for an additional 4 hrs (8 hrs total). This trend is in stark contract to the sample deposited
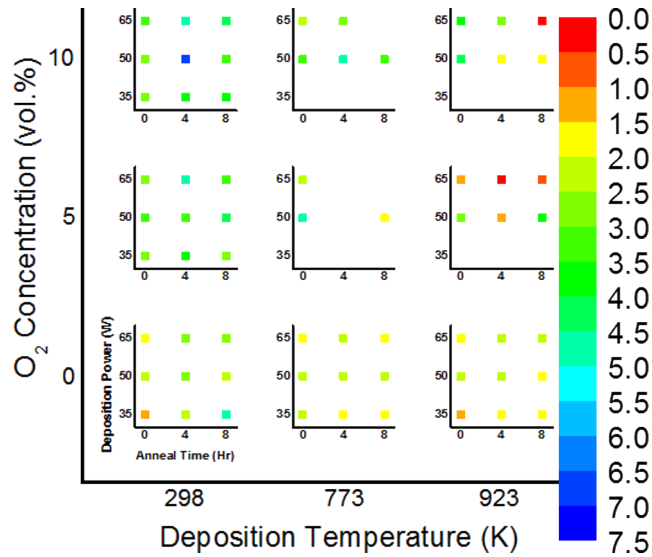
Figure 7.3   A representation of the degree of (111) vs. (220) texturing measured from each sample. The color of each point represents the value of the (111) peak intensity divided by the (220) peak intensity.

with 50 W or 65 W in a 10 vol.% O_2 atmosphere and a substrate temperature of 923 K. The samples deposited at these elevated powers and oxygen concentration became (220) textured after annealing. This (220) texturing persisted as the samples were annealed for 8 hrs total, showing that the texturing of these samples was stable. Currently, no physical explanation for these trends has been discovered.

The effect on the grain size growth as a function of annealing time was evaluated on the sample deposited at 923 K, 65 W deposition power, and 10 vol.% O_2 concentration. The grain size of the samples annealed for different lengths of time were quantified via SEM. For this analysis, an additional sample deposited at 923 K, 65 W deposition power, and 10 vol.% O2 concentration was annealed for 12 hours to better understand grain size growth dynamics. This sample was chosen for SEM analysis because it showed the highest degree of (220) stable texturing. The SEM images from the 4 hr, 8 hr, and 12 hr annealed sample are shown in Fig. 7.4. Fig. 7.4 shows that the samples were highly continuous, showing no signs of pinhole or crack formation. The as-deposited was not included in this analysis because the grains of this sam-

114

www.manaraa.com
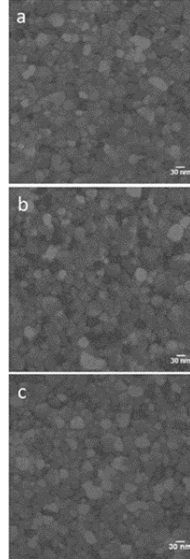
Figure 7.4   SEM images of the ScSZ deposited at 65 W, 10 vol.% O$_2$, and 923 K after undergoing a a) 4 hr anneal, b) hr anneal, and c) 12 hour anneal at 1273 K.

ple were too small to resolve with the available SEM. The grain size distribution of each sample was quantified by measuring the shortest and longest widths of over 300 crystal grains in each SEM image, referred to here as L_S and L_L respectively. The L_S and L_L value of each grain was then transformed into a scalar estimation of grain size, D with:

$$D = \sqrt{L_S * L_L} \tag{7.1}$$

This analysis assumes that each grain can be approximated by an ellipse, and the value of D is equivalent to the diameter of a circle with the same area as an ellipse with a short and long axis of length L_S and L_L, respectively. D is a less biased estimation of the grain size than just the measurement of either the L_S or L_L of each grain. The distribution of the grain sizes of the 4 hr, 8 hr, and 12 hr annealed samples were then determined, as shown in Fig. 7.5.

The average grain size was calculated to be 23.9 nm, 25.8 nm, and 27.4 nm, for the 4 hr, 8 hr, and 12 hr annealed samples, respectively. This means that little-to-
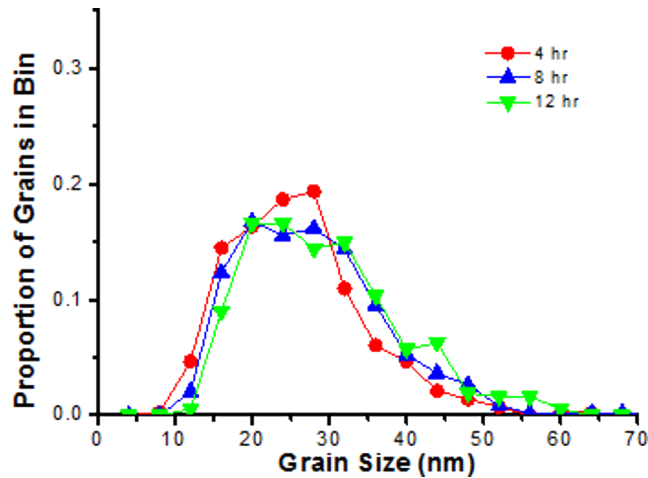
Figure 7.5   The measured grain size distribution of the ScSZ sample deposited at 65 W, 10 vol.% O_2, and 923 K and different annealing times. Each data point represents a bin size of 4 nm.

moderate grain growth occurred as the sample was annealed, with a 14.6% increase in the average grain size from the 4 hour annealed sample to the 12 hour annealed sample. Grain growth is probably due to smaller grains being incorporated into larger grains as the samples were annealed. This hypothesis is supported by the fact that as the samples were annealed, the distributions of the grains became more skewed to the right, shown in Fig. 7.5.

7.4   ScSZ Conclusions

Here, an investigation of the effect of sputtering conditions and processing on the crystal phase, crystallinity, and degree of texturing of ScSZ thin-films for SOFC electrolyte applications was performed. The samples were deposited at various gun powers, oxygen concentrations, and substrate temperature and were annealed at 1273 K for various annealing times. The the value of these four factors were set via a 3-level, 4-factor full factorial design of experiments.

Analysis of the crystal phase showed that all samples exhibited a pure cubic ScSZ phase, independent of deposition conditions and post-annealing. This indicates that

116

the creation of thin-film ScSZ electrolytes with the desired crystal phase can easily be achieved via magnetron sputtering. The crystallinity analysis showed that samples that were deposited onto substrates heated to 773 K or 923 K in the presence of 5 or 10 vol.% O_2 were moderately textured, while samples deposited at lower temperatures and oxygen concentrations were either disordered or slightly textured. A detailed analysis of the degree of texturing of each film showed that films with thermally stable (220) texturing could be achieved by depositing the samples with a gun power of 50 W or 65 W in a 10 vol.% O_2 atmosphere. Overall, this analysis shows that an ScSZ thin-film with the desirable crystal properties for SOFC electrolytes (aka desired crystal phase and a stable texture) could be deposited at a gun power of 50 W - 65 W, 10 vol.% O_2 atmosphere, and a substrate temperature of 923 K. Analysis of the amount of expected crystal grain growth with respect to annealing was performed on the samples that were deposited at 65 W, vol.% O_2 and 923 K. This analysis showed that as the sample was annealed the average grain size increased from 23.9 nm for the 4 hr annealed sample to 27.4 nm for the 12 hr annealed sample, indicating slight-to-moderate grain growth as the samples were annealed.

7.5 Preliminary Investigation of BYC

As stated in section 1.3, Huang *et al.* showed that BYC showed excellent oxygen ion conductivity [53]. Similar to other modified BYO electrolytes, BYC has a fluorite crystal structure with a high oxygen ion conductivity. This phase decomposes into a rhombohedral phase, which has a relatively low oxygen ion conductivity, at high temperatures. The absolute temperature of this decomposition varies and the oxygen ion conductivity of the material strongly depends on the composition of the BYC. Huang *et al.*'s previously studied the $(Bi_2O_3)_{0.75}(Y_2O_3)_{0.25}(CeO_2)_x$ psuedo-binary of BYC and found that a CeO_2 concentration of 5 mol% CeO_2 or more could stabilize the desired cubic phase of BYC when the sample was heated to . They also showed

117

that if the BYC contained 5 mol% to 10 mol% CeO_2, the high oxygen conductivity of BYO was retained. During all of these studies, a traditional ceramic synthesis method was used. Using the HTE framework developed in this thesis, the results of this previous BYC study were extended to investigate the sputter synthesis of BYC covering a larger portion of the ternary composition space. The details of synthesis of a BYC CCS magnetron sputtered thin-film sample and preliminary results on the deposition and thermal stability of the fluorite BYC phase will be given here.

Four CCS BYC samples were created by co-sputtering Bi_2O_3, Y_2O_3, and CeO_2 targets at 40 W RF, 75 W RF, and 18 W RF, respectively onto 7.62 cm diameter Si wafers. During deposition, the chamber was backfilled with Ar gas to a pressure of 0.667 Pa. These deposition parameters were determined by the sputtering model developed in chapter 3, and were designed to encompass part of the pseudo-binary composition of BYC from Huang *et al.*'s investigation. Each deposition was performed for 30 mins producing films with an average thickness of 103 nm. After deposition three of the samples were heat treated for 24 hours at different temperatures, one at 773 K, one at 873 K, and the last at 1073 in a Vulcan 3-550 box furnace. After the heat treatment, XRD was used to characterize 317 points on each sample using the SLAC assembly described in 2.2. The resulting XRD patterns were then analyzed to determine if only diffraction peaks indicative of the fluorite BYC were present in the sample or not.

The as-deposited, 773 K, and 873 K $Bi_2O_3)_{0.659}(Y_2O_3)_{0.284}(CeO_2)_{0.057}$ samples diffraction patterns are shown in Fig. 7.6. The as-deposited diffraction pattern shows broad diffraction peaks, with the only resolvable peak being located at 28.8° 2-θ. The broadness of these peaks indicate that the as-deposited samples were nanocrystalline in nature. The diffraction pattern of the sample after being heat treated at 773 K shows diffraction peaks located at 28.8° 2-θ, 33.2° 2-θ, 47.8° 2-θ, 56.8° 2-θ, 59.5° 2-θ, 69.9° 2-θ, 77.1° 2-θ, and 79.5° 2-θ, which are indicative of the fluorite BYC structures
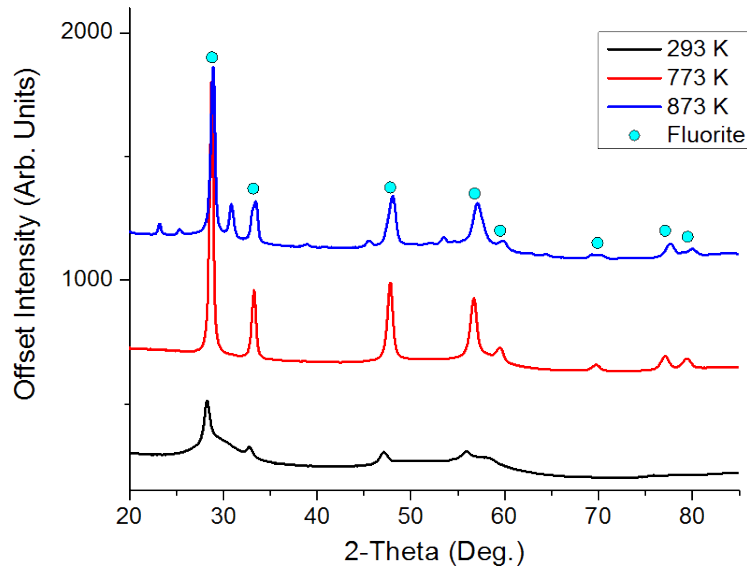
Figure 7.6   XRD patterns of the $(Bi_2O_3)_{0.659}(Y_2O_3)_{0.284}(CeO_2)_{0.057}$ samples. The sample annealed at 1073 K have unlabeled peaks that are associated with undetermined phases.

[53]. When the sample was annealed at 873 K, the fluorite peaks shift to the right and of multiple peaks appear that are indicative of secondary phases. Labeling of the secondary phase peaks is ongoing. A binary classification of the analyzed phases of all samples was performed, where each sample was labeled as containing pure fluorite BYC or a mixture of fluorite BYC and secondary phases.

Fig. 7.7 shows the results of the phase labeling from the BYC CCS samples and the results from Huang *et. al*'s previous investigation of BYC compositions annealed at temperatures between 1273-1373 K for 24 hours. Fig. 7.7 A) shows that a pure BYC fluorite structure was exhibited in samples containing less than 74.0 mol% Bi_2O_3. Fig. 7.7 B) shows that the compositional region where a pure fluorite BYC phase was observed shrank significantly after annealing, being constrained to samples containing less than 67.5 mol% Bi_2O_3. This compositional region shrank even more in the sample that was annealed at 873 K, only being observed in the samples with Bi_2O_3 content of less than 65 mol.%, shown in Fig. 7.7 C). Fig. 7.7 D) shows that no

119
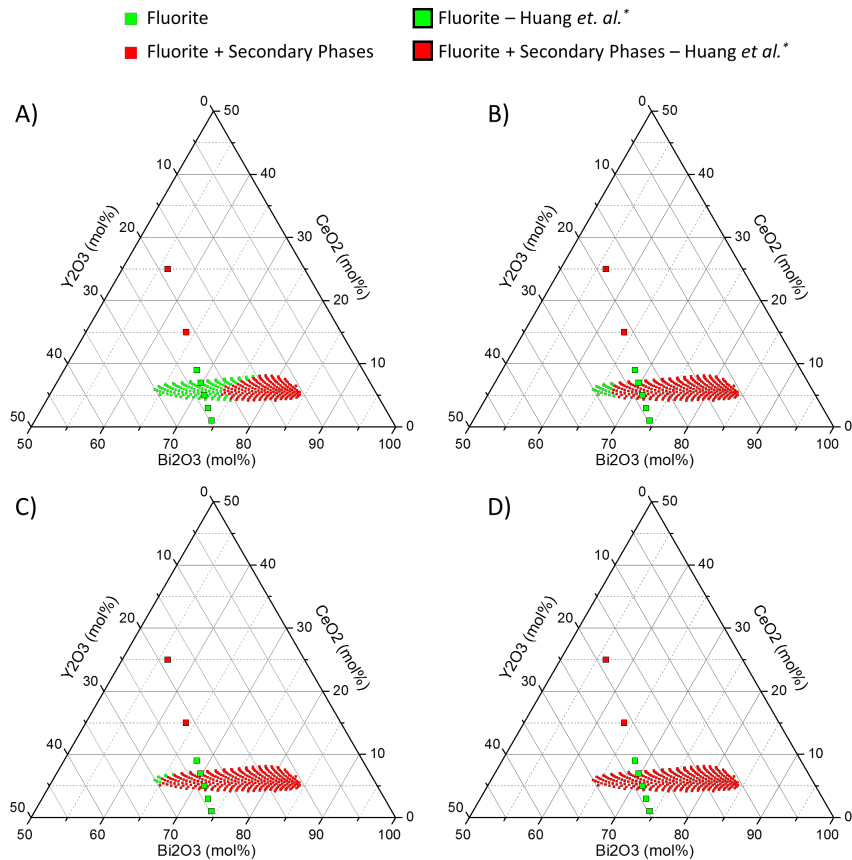
Figure 7.7   The phase labeling results of the A) as-deposited BYC sample and the samples annealed at B) 773 K, C) 873 K, and D) 1073 K for 24 hrs. *The data points and their phase analysis are with reference to the results found in ref. [53]

sample containing a pure fluorite BYC phase were observed in the sample that was annealed at 1073 K.

Comparison of these results with the previous results from Huang *et al.*'s study show that the two studies has different compositional regions of fluorite phase thermal stability. The current thin-film study did not show the existence of a pure fluorite phase within the entire studied composition regime after the sample was annealed at 1073 K for 24 hrs, while Huang *et al.* showed a stable fluorite phase in samples containing between 1 to 9 mol% CeO_2 after being annealed at 1273 K for 24 hrs. The disagreement between these two investigation is probably due to a combination of low melting temperature of Bi (544 K) and Bi_2O_3 (1090 K) and the differences

120

in bulk and thin-film materials. In the current thin-film investigation, the surface area to volume ratio is much larger than it is for bulk BYC materials. This means that changes in the sample that occur at the surface will have a much larger effect in thin-film samples than they will in bulk samples.

In the current BYC thin-film investigation, it is possible that the Bi/Bi_2O_3 species melted and left the surface of the sample during the annealing process. This would depreciate the overall Bi_2O_3 content in the sample significantly, causing massive changes in the composition of the sample and thus the BYC phase. This hypothesis was tested by measuring the Bi content at a single point on the as-deposited sample and the 1273 K annealed sample using EDS. The results of these measurements are shown in Fig. 7.8. Fig. 7.8 shows that the measured Bi signal significantly decreased after the sample was annealed. This result supports the hypothesis that the Bi content of the sample decreases significantly during the annealing, thus detrimentally effecting the crystal phase stability the sample.
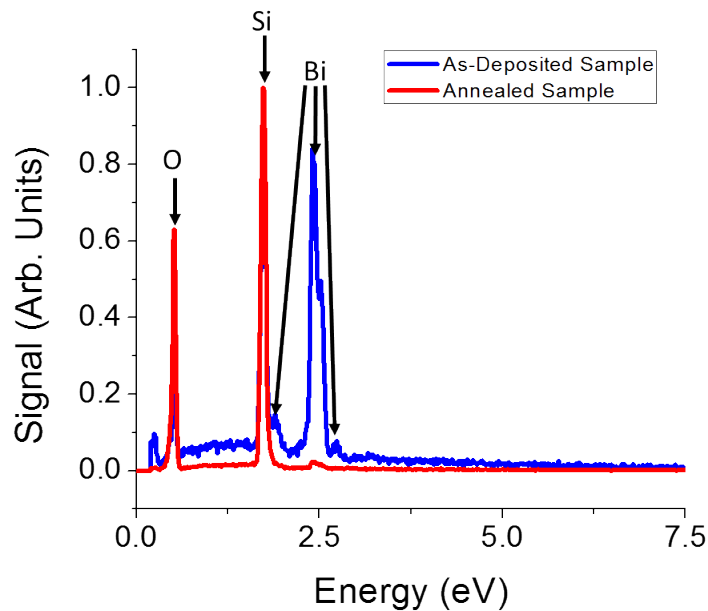
Figure 7.8   Then measured EDS spectra of the as-deposited sample and the sample annealed at 1073 K for 24 hrs.

The current thin-film investigation showed that the deposition of fluorite BYC phase could be achieved in samples containing $<$ 74.0 mol% Bi_2O_3, but that the deposited phase was highly nanocrystalline. The investigation showed that the sample annealed for 24 hours in at 773 K caused the fluorite phase of BYC to degrade in samples containing more 67.5 mol% Bi_2O_3. The amount of this degradation increased as the annealing temperature was increased, leading to no samples containing a pure BYC flourite phase when the sample was annealed at 1073 K for 24 hours. These results disagreed with previous studies, which showed that bulk BYC containing 1 mol% to 9 mol% CeO_2 contained a thermally stable BYC fluorite phase in samples annealed at 1273 K for 24 hours. The differences between the thin-film and bulk BYC phase stability was attributed a loss of Bi/Bi_2O_3 during the annealing process, which was supported by EDS measurements of the as-deposited and 1023 K annealed sample.

122

CHAPTER 8

CONCLUSIONS AND FUTURE WORK

8.1 CONCLUSIONS

High temperature thin-film materials are used in a variety of energy applications, such as corrosion resistant coatings and solid oxide fuel cell electrolytes. Design and optimization of such thin-film materials represent a hard engineering challenge due to the need to maintain high figure of merit while operating under harsh environments. This challenge is further exacerbated by the high number of engineering considerations and large number of parameters that need to be optimized. This large parameter space causes traditional one-by-one investigations of such systems to be prohibitively time consuming. HTE is an alternative experimental paradigm, which can significantly decrease the time needed to explore the large parameter space by performing sample synthesis, characterization, and analysis using quick-serial or parallel techniques.

In this thesis, a novel HTE framework which utilizes model guided sample synthesis, a combination of *in-situ* and *ex-situ* diffraction and spectroscopic techniques, and a semi-supervised machine learning algorithm to expedite the investigation of crystal phase dynamics of high-temperature thin-film materials was developed. This framework was then used to investigate the corrosion resistance Fe-Cr-Al alloys for nuclear cladding materials, and evaluate scandia-stabilized-zirconia (ScSZ) and bismuth-yttria-ceria (BYC) stability as thin-film SOFC electrolyte materials.

A semi-empirical sputtering model was developed to assist in the rapid synthesis of thin-film samples deposited via magnetron sputtering. The model can accurately

account for the effect of tilted sputtering guns and chimney shadowing effect. This model was validated through a series of experimentally measured deposition rates of Cu deposited with 0° to 31.3° gun-tilts, DC powers varying from 50 W to 200 W, and from guns with a short or tall chimney. The model predictions had a 2.12% ± 1.71% average relative error for the tall chimney predictions, and 4.14% ± 3.02%. The model's capabilities were extended by using a soft constrained, multiple stage multi-start Nelder-Mead optimization procedure to intelligently identify deposition conditions for sputtered HTE thin films. Validation of the optimization procedure showed that it had an average calculation time of 29.8 seconds to accurately determine sputtering conditions for a desired deposition. Overall, the combination of the semi-empirical model and the optimization procedure represents a 3-4 order of magnitude acceleration in the rate at which HTE samples can be designed and deposited.

A HTE experimental methodology that utilized XRD, Raman spectroscopy, and fluorescence to characterize the phase dynamics of a high-temperature sputtered CCS thin-film samples was developed. The methodology was validated on the well studied NiAl bond coat system. In this validation study, a CCS NiAl sample was cyclically heat treated at 1323 K, and the oxidation dynamics were monitored. The results of this study agreed with the previously reported trends that alloys containing higher amounts of Ni preferentially formed Al_2O_3 was observed.

SS-AutoPhase, a semi-supervised machine learning algorithm that performs automated phase mapping of diffraction and spectroscopic data was developed. SS-AutoPhase uses k-means clustering to automatically select representative data that a human expert analyzes and labels. This labeled data is used to train an AdaBoost classifier, which can then be used to automatically phase label new datasets. The performance of SS-AutoPhase was evaluated on an "open" FeGaPd CCS thin-film sample. The investigation showed that SS-AutoPhase had a minimum accuracy of 82.6% when using $\geq 15\%$ of the total dataset for training. SS-AutoPhase was used to

124

create a predicted most probable phase diagram and compared with the phase labels from HCA, MST, NMF, and the human expert. Overall, the comparison showed that NMF, SS-AutoPhase were in higher agreement with expert analysis than the phase labels HCA and MST.In addition to being in high agreement with the expert analysis, SS-AutoPhase was the only algorithm to identify the existence of an new unknown phase. The identification of this new phase and the high accuracy of SS-AutoPhase exhibited the robust nature of SS-AutoPhase to perform automatic phase labeling.

The developed HTE framework was used in a 2-stage investigation to evaluate the potential for Fe-Cr-Al thin-films to be used as high-temperature oxidation-resistant coatings for nuclear cladding materials. In the first stage, a CCS Fe-Cr-Al sample at temperatures ranging from 420 K to 690 K was monitored using *in-situ* diffraction. The intermediate temperature study showed four separate compositional regions which expressed different oxidation dynamics were identified. Furthermore, it showed that samples containing > 3.08 at.% Al and 20.0 at.% - 32.9 at.% Cr, balance Fe, exhibited suppressed oxidation. In the second stage, 8 Fe-Cr-Al samples were deposited whose composition covered the four identified regions of oxidation. The 8 samples were cyclically heat treated at 1323 K for times ranging from 5 to 360 minutes, and oxidation dynamics were monitored using Raman spectroscopy/fluorescence. The high temperature investigation showed that samples with > 3.08 at.% Al, 20.0 at.% - 32.9 at.% Cr, and balance Fe exhibited strong α-Al_2O_3 growth after 60 minutes, 120 minutes faster than samples in the other compositional regions. The results from both the intermediate and high temperature Fe-Cr-Al CCS samples agreed that samples with > 3.08 at.% Al, 20.0 at.% - 32.9 at.% Cr are strong potential candidates as high-temperature oxidation resistance for nuclear cladding materials.

The developed HTE framework was also used to evaluate the effect of sputtering conditions and processing on the crystal phase, crystallinity, and degree of texturing of the ScSZ thin-films was investigated using XRD. A 3^4 full factorial design of

125

the gun power, oxygen concentration, substrate temperature, and post deposition annealing time at 1273 K was used to create 69 samples. XRD measurements indicated that pure cubic ScSZ was present in all the samples, showing that deposition of thin-film ScSZ electrolytes with the desired crystal phase can easily be achieved via magnetron sputtering. Analysis of the crystallinity and degree of texture of the samples showed that moderately textured films with thermally stable (220) texturing could be achieved by depositing the samples with a gun power of 50 W or 65 W in a 10 vol.% O_2 atmosphere.

8.2 Future Work: SS-AutoPhase

During the phase predictions of the "open" FeGaPd CCS thin-film sample diffraction data, it was observed that the negatively biased nature of the crystals phases in this dataset negatively impacted the true positive rate and accuracy of SS-AutoPhase. One potential method to overcome this issue is to alter the training procedure of the AdaBoost classifier. In this altered training procedure, the AdaBoost classifier could be trained multiple times with a unbiased subset (i.e. same number of trues and positives) of the total training data. Each time the AdaBoost classifier is trained, a different permutation of the total training data could be used to generate the unbiased subset of data. The reason that the ensemble of unbiased AdaBoost classifiers would need to be used instead of just a single one is that by using less training data, a single AdaBoost classifier will have a relatively low accuracy. This accuracy could be recovered by using each AdaBoost classifier to perform phase labeling on new datasets, and using analysis techniques similar to the ones used evaluate the predicted most probable phase diagram.

126

8.3 Future Work: FeCrAl Thin-Films for Oxidation Resistant Coatings Nuclear Cladding Materials

During the evaluation of Fe-Cr-Al oxidation resistance, it was determined that alloys containing > 3.08 at.% Al, 20.0 at.% - 32.9 at.% Cr were strong potential candidates as high-temperature oxidation resistance for nuclear cladding materials. It was also observed that the amount of Cr in these thin films was a little higher than the results from previous studies of bulk Fe-Cr-Al samples. Even though characterization of these samples did not show the presence of Cr oxides, this increased Cr content could lead to the growth of $CrO_2(OH)$ when in the presence of high temperature steam. As stated in section 1.2, $CrO_2(OH)$ will vaporize, causing damage to the Fe-Cr-Al coating. Evaluation of this potentially damaging $CrO_2(OH)$ phase growth will be investigated by depositing a CCS sample focused on the oxidation resistant region from the current Fe-Cr-Al evaluation (Rg2). This sample will subjected to high-temperatures in the presence of a steam and evaluated using the same procedure outlined in the cyclic high temperature evaluation used in section 6.2.

8.4 Future Work: ScSZ Thin-Films as SOFC Electrolytes

The crystallographic investigation of magnetron ScSZ thin-films to be used as SOFC electrolytes showed that the desired cubic crystal phase could easily be deposited. It also showed that the sputtering conditions could be controlled to create samples with various crystallinity and textures. In the future, the results of this study will be used to deposit samples with varying crystallinity and textures onto Pt foil. The ionic conductivity of these sample will then be measured via impedance spectroscopy. The sample that has the highest ionic conductivity will then be used to create a full SOFC assembly, which will be evaluated. The performance from this full SOFC assembly will be compared to that of a SOFC assembly with a ScSZ electrolyte created using

traditional ceramic synthesis techniques.

8.5   Future Work: BYC Thin-Films as SOFC Electrolytes

The high-temperature phase stability study of BYC showed that the fluorite phase decomposed to unknown phases at relatively low temperatures compared to previous bulk studies of this material. It was hypothesized that the Bi/Bi_2O_3 compounds in the sample are melting then leaving the sample surface, causing the sample composition to change and destabilize the fluorite BYC phase. Initial EDS measurements supported this hypothesis, showing that that the Bi content of the annealed sample was significantly smaller than the as-deposited sample. In the future, the identity of the secondary phases will be determined. This phase identification will give key insight into potential degradation pathways of the fluorite phase. Furthermore, compositional analysis of deposited BYC thin-films processed at multiple temperatures between 293 K and 1073 K will be performed. Once the mechanism associated with the fluorite BYC decomposition has been identified, potential solutions to overcome this issue will be identified.

128

Bibliography

[1] Hiroshi Arikawa, Hiroyasu Nishiguchi, Tatsumi Ishihara, and Yusaku Takita. Oxide ion conductivity in Sr-doped La10Ge6O27 apatite oxide. *Solid State Ionics*, 136-137:31–37, 2000.

[2] E. N. Armstrong, K. L. Duncan, D. J. Oh, J. F. Weaver, and E. D. Wachsman. Determination of Surface Exchange Coefficients of LSM, LSCF, YSZ, GDC Constituent Materials in Composite SOFC Cathodes. *Journal of The Electrochemical Society*, 158:B492–B499, 2011.

[3] David Arthur and Sergei Vassilvitskii. k-means++: The Advantages of Careful Seeding. In *Proceedings of the eighteenth annual ACM-SIAM symposium on Discrete algorithms*, pages 1–11, 2007.

[4] Gordon Barr, Wei Dong, and Christopher J. Gilmore. High-throughput powder diffraction. II. Applications of clustering methods and multivariate data analysis. *Journal of Applied Crystallography*, 37(2):243–252, 2004.

[5] Laurent Allan Baumes, Manuel Moliner, Nicolas Nicoloyannis, and Avelino Corma. A reliable methodology for high throughput identification of a mixture of crystallographic phases from powder X-ray diffraction data. *CrystEngComm*, 10(10):1321, 2008.

[6] M. Birkholz, C. Genzel, and T. Jung. X-ray diffraction study on residual stress and preferred orientation in thin titanium films subjected to a high ion flux during deposition. *Journal of Applied Physics*, 96(12):7202–7211, 2004.

[7] D. Brassard, S. Fourmaux, M. Jean-Jacques, J. C. Kieffer, and M. A. El Khakani. Grain Size Effect on the Semiconductor-Metal Phase Transition Characteristics of Magnetron-Sputtered VO2 Thin Films. *Applied Physics Letters*, 87:051910, 2005.

[8] D.J.L. Brett, A. Atkinson, N.P. Brandon, and S.J. Skinner. Intermediate Temperature Solid Oxide Fuel Cells. *Chemical Society Reviews*, 37:1568–1578, 2008.

[9]   Jonathan K. Bunn, Richard Z. Voepel, Zhiyong Wang, Edward P. Gatzke, Jochen A. Lauterbach, and Jason R. Hattrick-Simpers. Development of an Optimization Procedure for Magnetron-Sputtered Thin Films to Facilitate Combinatorial Materials Research. *Industrial & Engineering Chemistry Research*, 55:1236–1242, 2016.

[10]   Jonathan Kenneth Bunn, Randy L Fang, Mark R Albing, Apurva Mehta, Matthew J Kramer, Matthew F Besser, and Jason R Hattrick-Simpers. A high-throughput investigation of Fe-Cr-Al as a novel high-temperature coating for nuclear cladding materials. *Nanotechnology*, 26(27):274003, 2015.

[11]   Jonathan Kenneth Bunn, Shizhong Han, Yan Tong, Yan Zhang, Jianjun Hu, and Jason Ryan Hattrick-Simpers. Generalized machine learning technique for automatic phase attribution in time variant high-throughput experimental studies. *Journal of Materials Research*, 30(7):879–889, 2015.

[12]   Jonathan Kenneth Bunn, Jianjun Hu, and Jason R. Hattrick-Simpers. Semi-Supervised Approach to Phase Identification from Combinatorial Sample Diffraction Patterns. *Jom*, 68(8):2116–2125, 2016.

[13]   Jonathan Kenneth Bunn, C J Metting, and J R Hattrick-Simpers. Development of an Accurate Semi-Empirical Model for Tilted-Gun Planer Magnetron Sputtering Accounting for Chimney Shadowing. *JOM*, 67(1):154–163, 2015.

[14]   D. Caplan and M. Cohen. The Volatilization of Chromium Oxide. *Journal of The Electrochemical Society*, 108(5):438, 1961.

[15]   Mu Chai and J Michael Brown. Effects of static non-hydrostatic strss on the R lines of ruby. *Geophysical Research Letters*, 23(24):3539–3542, 1996.

[16]   J F Chang, H H Kuo, I C Leu, and M H Hon. The effects of thickness and operation temperature on ZnO : Al thin film CO gas sensor. *Sensors and Actuators, B: Chemical*, 84(2-3):258–264, 2002.

[17]   Keke Chang, Denis Music, Moritz to Baben, Dennis Lange, Hamid Bolvardi, and Jochen M Schneider. Modeling of Metastable Phase Formation Diagrams for Sputtered Thin Films. *Science and Technology of Advanced Materials*, 17:210–219, 2016.

[18]   Xiang Chen, Rick Haasch, and James F. Stubbins. Impedance spectroscopy and microstructural characterization of the corrosion behavior of FeCrAl alloy in lead-bismuth eutectic. *Journal of Nuclear Materials*, 431(1-3):125–132, 2012.

130

[19] Ting Cheng, James R. Keiser, Michael P. Brady, Kurt A. Terrani, and Bruce A. Pint. Oxidation of fuel cladding candidate materials in steam environments at high temperature and pressure. *Journal of Nuclear Materials*, 427(1-3):396–400, 2012.

[20] D.R. Clarke and C.G. Levi. Materials Design for the Next Generation Thermal Barrier Coatings. *Annual Review of Materials Research*, 33(1):383–417, 2003.

[21] C. Corbella, M. Vives, A. Pinyol, E. Bertran, C. Canal, M. C. Polo, and J. L. Andújar. Preparation of metal (W, Mo, Nb, Ti) containing a-C:H films by reactive magnetron sputtering. *Surface and Coatings Technology*, 177-178:409–414, 2004.

[22] Jun Cui, Yong S. Chu, Olugbenga O. Famodu, Yasubumi Furuya, Jason R Hattrick-Simpers, Richard D. James, Alfred Ludwig, Sigurd Thienhaus, Manfred Wuttig, Zhiyong Zhang, and Ichiro Takeuchi. Combinatorial search of thermoelastic shape-memory alloys with extremely small hysteresis width. *Nature materials*, 5(4):286–90, 2006.

[23] Stefano Curtarolo, Gus L W Hart, Marco Buongiorno Nardelli, Natalio Mingo, Stefano Sanvito, and Ohad Levy. The high-throughput highway to computational materials design. *Nature materials*, 12(3):191–201, 2013.

[24] Sebastien Dryepondt, Aurelie Rouaix-Vande Put, and Bruce A. Pint. Effect of H2O and CO2 on the Oxidation Behavior and Durability at High Temperature of ODS-FeCrAl. *Oxidation of Metals*, 79(5-6):627–638, feb 2013.

[25] EG&G Technical Services Inc. Fuel Cell Handbook. 7 Edition(November):3–1, 2004.

[26] J. Engkvist, S. Canovic, K. Hellström, A. Järdnäs, J.-E. Svensson, L.-G. Johansson, M. Olsson, and M. Halvarsson. Alumina Scale Formation on a Powder Metallurgical FeCrAl Alloy (Kanthal APMT) at 900-1,100 Degree C in Dry O2 and in O2 + H2O. *Oxidation of Metals*, 73(1-2):233–253, sep 2009.

[27] Stefano Ermon, Ronan Le Bras, Santosh K Suram, John M Gregoire, Carla P Gomes, Bart Selman, and Robert B. Van Dover. Pattern Decomposition with Complex Combinatorial Constraints: Application to Materials Discovery. *CoRR*, 1411.7441, 2014.

[28] Jeffrey W. Fergus. Electrolytes for Solid Oxide Fuel Cells. *Journal of Power Sources*, 162:30–40, 2006.

131

[29] Yoav Freund and Robert E Schapire. A Decision-Theoretic Generalization of On-Line Learning and an Application to Boosting. *Journal of Computer and System Sciences*, 55(1):119–139, 1997.

[30] Kuan Z. Fung and Anil V. Virkar. Phase Stability, Phase Transformation Kinetics, and Conductivity of Y2O3-Bi2O3 Solid Electrolytes Containing Aliovalent Dopants. *Journal of the American Ceramic Society*, 74:1970–1980, 1991.

[31] J Gassiot. The Bakerian Lecture: On the Stratifications and Dark Bands in Electrical Discharges as Observed in Torricellian Vacuums. *Philosophical Transactions of the Royal Society of London*, 148:1–16, 1858.

[32] Randall Gauntt, Donald Kalinich, Jeff Cardoni, Jesse Phillips, Andrew Goldmann, Susan Pickering, Matthew Francis, Kevin Robb, Larry Ott, Dean Wang, Curtis Smith, Shawn St Germain, David Schwieder, and Cherie Phelan. Fukushima Daiichi Accident Study (Status as of April 2012). *Sandia National Laboratory Report, SAND2012-6173, Albuquerque, NM*, 2012.

[33] Julie A. Glasscock, Piers R. F. Barnes, Ian C. Plumb, and Nick Savvides. Enhancement of Photoelectrochemical Hydrogen Production from Hematite Thin Films by the Introduction of Ti and Si. *Journal of Physical Chemistry C*, 111:16477–16488, 2007.

[34] B. Gleeson, N. Mu, and S. Hayashi. Compositional factors affecting the establishment and maintenance of Al2O3 scales on Ni-Al-Pt systems. *Journal of Materials Science*, 44(7):1704–1710, feb 2009.

[35] H. Götlind, F. Liu, J.-E. Svensson, M. Halvarsson, and L.-G. Johansson. The Effect of Water Vapor on the Initial Stages of Oxidation of the FeCrAl Alloy Kanthal AF at 900 Degree C. *Oxidation of Metals*, 67(5-6):251–266, apr 2007.

[36] A. Gras-Marti and J. a. Valles-Abarca. Slowing down and thermalization of sputtered particle fluxes: Energy distributions. *Journal of Applied Physics*, 54(2):1071, 1983.

[37] Martin L. Green, Jason Ryan Hattrick-Simpers, Ichiro Takeuchi, Sara C Barron, Ajey M Joshi, Tony Chiang, Apurva Mehta, and Albert Davydov. Fulfilling the Promise of the Materials Genome Initiative via High-Throughput Experimentation. pages 1–13, 2014.

[38] J. Gregoire, M. Lobovsky, M. Heinz, F. DiSalvo, and R. van Dover. Resput-

tering Phenomena and Determination of Composition in Codeposited Films. *Physical Review B*, 76(19):195437, nov 2007.

[39] W R Grove. On the Electro-Chemical Polarity of Gases. *Philosophical Transactions of the Royal Society of London*, 142:87–101, 1852.

[40] Daniel C. Harris and Michael D. Bertolucci. *Symmetry and Spectroscopy; An Introduction to Vibrational and Electronic Spectroscopy.* Courier Corporation, 1978.

[41] J. A. Hartigan and M. A. Wong. Algorithm AS 123: A K-Means Clustering Algorithms. *Journal of the Royal Statistical Society, Series C (Applied Statistics)*, 28(1):100–108, 1979.

[42] Jason R Hattrick-Simpers, John M Gregoire, and A Gilad Kusne. Perspective : Composition âĂŞ structure âĂŞ property mapping in high-throughput experiments : Turning data into knowledge Perspective : Composition âĂŞ structure âĂŞ property mapping in high-throughput experiments : Turning data into knowledge. *APL Materials*, 4(053211), 2016.

[43] Jason R. Hattrick-Simpers, Dwight Hunter, Corneliu M. Craciunescu, Kyu Sung Jang, Makoto Murakami, James Cullen, Manfred Wuttig, Ichiro Takeuchi, Samuel E. Lofland, Leonid Benderksy, Noble Woo, Robert Bruce Van Dover, Toshiya Takahashi, and Yasubumi Furuya. Combinatorial investigation of magnetostriction in Fe-Ga and Fe-Ga-Al. *Applied Physics Letters*, 93(10):4–6, 2008.

[44] Jason R Hattrick-Simpers, Cun Wen, and Jochen Lauterbach. The Materials Super Highway: Integrating High-Throughput Experimentation into Mapping the Catalysis Materials Genome. *Catalysis Letters*, 2014.

[45] Shigenari Hayashi, W E N Wang, Daniel J Sordelet, and Brian Gleeson. Interdiffusion Behavior of Pt-Modified Gamma-Ni + Gamma'-Ni3Al Alloys Coupled to Ni-Al - Based Alloys. *Metallurgical and Materials Transactions A*, 36:1769–1775, 2005.

[46] Baoping Bob He, Uwe Preckwinkel, and Kingsley L Smith. Fundamentals of Two-Dimensional X-ray Diffraction (XRD2). *Advances in X-ray Analysis*, 43(c):273–280, 1999.

[47] Mariette Hellenbrandt. The Inorganic Crystal Structure Database (ICSD)âĂŤPresent and Future. *Crystallography Reviews*, 10(1):17–22, 2004.

[48] A Holzwarth and Wilhelm F. Maier. Catalytic phenomena in combinatorial libraries of heterogeneous catalysts. *Platinum Metals Review*, (1):16–21, 2000.

[49] Arnold Holzwarth, Schmidt Hans-Werner, and Wilhelm F. Maier. Devection of Catalytic Activity in Combinatorial Libraries of Heterogeneous Catalysts by IR Thermography. *Angewandte Chemie - International Edition*, 37(19):2644–2647, 1998.

[50] P. Y. Hou. Segregation behavior at TGO/bondcoat interfaces. *Journal of Materials Science*, 44(7):1711–1725, sep 2009.

[51] P Y Hou, A P Paulikas, and B W Veal. Stress Development and Relaxation in Al2O3 During Early Stage Oxidation of β -NiAl. *Materials at High Temperatures*, 22(3-4):535–543, 2005.

[52] P.Y. Hou. Segregation Phenomena at Thermally Grown Al2O3 /Alloy Interfaces. *Annual Review of Materials Research*, 38(1):275–298, aug 2008.

[53] Keqin Huang, Man Feng, and John B. Goodenough. Bi2O3-Y2O3-CeO2 solid solution oxide-ion electrolyte. *Solid State Ionics*, 89:17–24, 1996.

[54] Keqin Huang, Robin S Tichy, and John B Goodenough. Superior Perovskite Oxide-Ion Conductor; Strontium- and Magnesium-Doped LaGaO3: I, Phase Relationships and Electrical Properties. *Journal of American Ceramics Society*, 81(10):2565–2575, 1998.

[55] Citrine Informatics. Fe-Ga-Pd, 2006.

[56] A Jaboski. Efficiency of Anti-Stokes Fluorescence in Dyes. *Nature*, 131:839–840, 1933.

[57] Allan J. Jacobson. Materials for Solid Oxide Fuel Cells. *Chemistry of Materials*, 22:660–674, 2010.

[58] Jun Jiang. *The Role of Strain and Structure on Oxygen Ion Conduction in Nanoscale Zirconia and Ceria Thin Films.* PhD thesis, University of Delaware, 2014.

[59] San Ping Jiang. Dependence of Cell Resistivity on Electrolyte Thickness in Solid Oxide Fuel Cells. *Journal of Power Sources*, 183:595–599, 2008.

134

[60] Daisuke Kan, Christian J. Long, Christian Steinmetz, Samuel E. Lofland, and Ichiro Takeuchi. Combinatorial search of structural transitions: Systematic investigation of morphotropic phase boundaries in chemically substituted BiFeO3. *Journal of Materials Research*, 27(21):2691–2704, 2012.

[61] Igor Kosacki, Harlan U. Anderson, Yasunobu Mizutani, and Kenji Ukai. Non-stoichiometry and electrical transport in Sc-doped zirconia. *Solid State Ionics*, 152-153:431–438, 2002.

[62] Rainer Küngas, Fred Bidrawn, Eyas Mahmoud, John M. Vohs, and Raymond J. Gorte. Evidence of surface-reaction rate limitations in SOFC composite cathodes. *Solid State Ionics*, 225:146–150, 2012.

[63] Aaron Gilad Kusne, Tieren Gao, Apurva Mehta, Liqin Ke, Manh Cuong Nguyen, Kai-Ming Ho, Vladimir Antropov, Cai-Zhuang Wang, Matthew J. Kramer, Christian Long, and Ichiro Takeuchi. On-the-fly machine-learning for high-throughput experiments: search for rare-earth-free permanent magnets. *Scientific Reports*, 4:6367, 2014.

[64] Ronan Le Bras, Theodoros Damoulas, John M Gregoire, Ashish Sabharwal, Carla P Gomes, and R Bruce Van Dover. Constraint Reasoning and Kernel Clustering for Pattern Decomposition With Scaling. *Principles and Practice of Constraint Programming âĂŞ CP 2011*, 6878:508–522, 2011.

[65] Ze Lei and Qingshan Zhu. Low Temperature Processing of Dense Nanocrystalline Scandia-Doped Zirconia (ScSZ) Ceramics. *Solid State Ionics*, 176:2791–2797, 2005.

[66] J S Liebig, P Frach, H Bartzsch, D Schulze, and H Schwanbeck. Numerical modelling of charged particle motion in electric and magnetic fields to assist magnetron design. *Surface and Coatings Technology*, 97(1-3):626–632, 1997.

[67] D. M. Lipkin and D. R. Clarke. Measurement of the stress in oxide scales formed by oxidation of alumina-forming alloys. *Oxidation of Metals*, 45(3-4):267–280, apr 1996.

[68] Zhufang Liu and Robert J Davis. Investigation of the Structure of Microporous Ti-Si Mixed Oxides by X-ray, UV Reflectance, FT-Raman, and FT-IR Spectroscopies. *Journal of Physical Chemistry*, 98:1253–1261, 1994.

[69] C. J. Long, D. Bunker, X. Li, V. L. Karen, and I. Takeuchi. Rapid identification of structural phases in combinatorial thin-film libraries using x-ray diffrac-

135

tion and non-negative matrix factorization. *Review of Scientific Instruments*, 80(10):1–6, 2009.

[70] C. J. Long, Jason R Hattrick-Simpers, M. Murakami, R. C. Srivastava, I. Takeuchi, V. L. Karen, and X. Li. Rapid structural mapping of ternary metallic alloy systems using the combinatorial approach and cluster analysis. *Review of Scientific Instruments*, 78(7), 2007.

[71] Neelima Mahato, Amitava Banerjee, Alka Gupta, Shobit Omar, and Kantesh Balani. Progress in Material Selection for Solid Oxide Fuel Cell Technology: A Review. *Progress in Materials Science*, 72:141–337, 2015.

[72] Wilhelm F. Maier, Klaus Stowe, and Simone Sieg. Combinatorial and high-throughput materials science. *Angewandte Chemie - International Edition*, 46(32):6016–6067, 2007.

[73] Samuel H. Margueron and David R. Clarke. Stress anisotropy of the R-line luminescence lifetime in single crystal Cr-doped sapphire (ruby). *Journal of Applied Physics*, 101(9):093521, 2007.

[74] N. Matsunami, Y. Yamamura, Y. Itikawa, N. Itoh, Y. Kazumata, S. Miyagawa, K. Morita, and R. Shimuzu. A semiempirical formula for the energy dependence of the sputtering yield. *Radiation Effects Letters*, 57:15–21, 1980.

[75] P. S. McLeod and L. D. Hartsough. High-rate sputtering of aluminum for metallization of integrated circuits. *Journal of Vacuum Science and Technology*, 14(1):263–265, 1977.

[76] X Q Meng, X J Fan, and H X Guo. A new fromula on the thickness of films deposited by planar and cylindrical magnetron sputtering. *Thin Solid Films*, (335):279–283, 1998.

[77] C Mennicke, E Schumann, M Ruhle, R J Hussey, G I Sproule, and M J Graham. The Effect of Yttrium on the Growth Process and Microstructure of a-Al2O3 on FeCrAl. *Oxidation of Metals*, 49:455–466, 1998.

[78] Christopher Jason Metting, Jonathan Kenneth Bunn, Ellen Underwood, Stephen Smoak, and Jason R Hattrick-Simpers. Combinatorial Approach to Turbine Bond Coat Discovery. *ACS combinatorial science*, 15:419–424, 2013.

[79] Kevin Meyer, Ivan K Schuller, and Charles M Falco. Thermalization of sputtered atoms. *Journal of Applied Physics*, 52:5803, 1981.

136

[80] K. Minami, T. Masui, N. Imanaka, L. Dai, and B. Pacaud. Redox Behavior of CeO2-ZrO2-Bi2O3 and CeO2-ZrO2-Y2O3 Solid Solutions at Moderate Temperatures. *Journal of Alloys and Compounds*, 408-412:1132–1135, 2006.

[81] N Mironova-Ulmane, A Kuzmin, I Steins, J Grabis, I Sildos, and M Pärs. Raman scattering in nanosized nickel oxide NiO. *Journal of Physics: Conference Series*, 93:012039, dec 2007.

[82] National Renewable Laboratory. *1 – 10 kW Stationary Combined Heat and Power Systems Status and Technical Potential*. Number November. U.S. Deparment of Energy, Golden, Colorado, 2010.

[83] National Science and Technology Council. Materials Genome Initiative for Global Competitiveness. (June), 2011.

[84] National Science and Technology Council. Materials Genome Initiative Strategic Plan. (June), 2014.

[85] J Nelder and R Mead. A simplex method for function minimization. *The Computer Journal*, 7(6):308–313, 1965.

[86] L. Niewolak, D. Naumenko, E. Wessel, L. Singheiser, and W.J. Quadakkers. Optical fluorescence spectroscopy for identification of minor oxide phases in alumina scales grown on high temperature alloys. *Materials Characterization*, 55(4-5):320–331, nov 2005.

[87] K. Nomura, Y. Mizutani, M. Kawai, Y. Nakamura, and O. Yamamoto. Aging and Raman Scattering Study of Scandia and Yttria Doped Zirconia. *Solid State Ionics*, 132:235–239, 2000.

[88] Elizabeth J Opila. Volatility of common protective oxides in high-temperature water vapor: current understanding and unanswered questions. In *Materials Science Forum*, volume 461, pages 765—-774. Trans Tech Publications, 2004.

[89] A L Patterson. The Scherrer formula for X-ray particle size determination. *Physical Review*, 56:978, 1939.

[90] Fabian Pedregosa and G Varoquaux. Scikit-learn: Machine learning in Python. *Journal of Machine Learning Research*, 12:2825–2830, 2011.

[91] John H Perepezko. Materials science. The hotter the engine, the better. *Science*, 326:1068–1069, nov 2009.

[92] F S Pettit. Oxidation Mechanisms for Ni-Al Alloys at Temperatures Between 900 and 1300 C. *Transactions of the Metallurgical Society of AIME*, 239(9):1296–1305, 1967.

[93] B. a. Pint and K. L. More. Characterization of alumina interfaces in TBC systems. *Journal of Materials Science*, 44(7):1676–1686, feb 2009.

[94] B. a. Pint, K. a. Terrani, M. P. Brady, T. Cheng, and J. R. Keiser. High temperature oxidation of fuel cladding candidate materials in steam-hydrogen environments. *Journal of Nuclear Materials*, 440(1-3):420–427, 2013.

[95] Radislav a Potyrailo, Krishna Rajan, Klaus Stowe, Ichiro Takeuchi, Bret Chisholm, and Hubert Lam. Combinatorial and High-Throughput Screening of Materials Libraries: Review of State of the Art. *ACS combinatorial science*, 13:579–633, 2011.

[96] R. C. Reed. *The Superalloys: Fundamentals and Applications.* Cambridge University PRess, Cambridge, U.K., 2006.

[97] D. Renusch, M. Grimsditch, I. Koshelev, B. W. Veal, and P. Y. Hou. Strain determination in thermally-grown alumina scales using fluorescence spectroscopy. *Oxidation of Metals*, 48(5-6):471–495, dec 1997.

[98] B. Saha, N.S. Das, and K.K. Chattopadhyay. Combined Effect of Oxygen Deficient Point Defects and Ni Doping in Radio Frequency Magnetron Sputtering Deposited ZnO Thin Films. *Thin Solid Films*, 562:37–42, 2014.

[99] S. Sarat, N. Sammes, and A. Smirnova. Bismuth Oxide Doped Scandia-Stabilized Zirconia Electrolyte for the Intermediate Temperature Solid Oxide Fuel Cells. *Journal of Power Sources*, 160:892–896, 2006.

[100] S Schiller, K Goedicke, J Reschke, V Kirchhoff, S Schneider, and F Milde. Pulsed Magnetron Sputter Technology. *Surface and Coatings Technology*, 61:331–337, 1993.

[101] M. P. Seah, C. a. Clifford, F. M. Green, and I. S. Gilmore. An accurate semi-empirical equation for sputtering yields I: for argon ions. *Surface and Interface Analysis*, 37(5):444–458, may 2005.

[102] Pedro Serna, Laurent a. Baumes, Manuel Moliner, and Avelino Corma. Combining high-throughput experimentation, advanced data modeling and funda-

mental knowledge to develop catalysts for the epoxidation of large olefins and fatty esters. *Journal of Catalysis*, 258(1):25–34, 2008.

[103] R B Setterlund and G R Prescott. Corrosion Characteristics of FeAlCr Allots in High T Petrol Applications.pdf. *Corrosion- National Association of corrosion Engineers*, 17:103–108, 1961.

[104] Aniketa Shinde, Dan Guevarra, Joel A. Haber, Jian Jin, and John M. Gregoire. Identification of optimal solar fuel electrocatalysts via high throughput in situ optical measurements. *Journal of Materials Research*, 30(03):442–450, 2015.

[105] P. Sigmund. On the Number of Atoms Displaced By Implanted Ions or Energetic Recoil Atoms. *Applied Physics Letters*, 14(3):114, 1969.

[106] M. Sillassen, P. Eklund, N. Pryds, N. Bonanos, and J. Bottiger. Concentration-Dependent Ionic Conductivity and Thermal Stability of Magnetron-Sputtered Nanocrystalline Scandia-Stabilized Zirconia. *Solid State Ionics*, 181:1140–1145, 2010.

[107] M. Sillassen, P. Eklund, M. Sridharan, N. Pryds, N. Bonanos, and J. Bøttiger. Ionic conductivity and thermal stability of magnetron-sputtered nanocrystalline yttria-stabilized zirconia. *Journal of Applied Physics*, 105(10):1–7, 2009.

[108] A. K. Singh. *Advanced X-ray Techniques in Research and Industry*. IOP Press, 2005.

[109] Preetam Singh and John B. Goodenough. Sr1-xKxSi1-yGeyO3-0.5x: A New Family of Superior Oxide-Ion Conductors. *Energy & Environmental Science*, 5:9626, 2012.

[110] Preetam Singh and John B Goodenough. Monoclinic Sr1-xNaxSiO3-0.5x: New Superior Oxide Ion Electrolytes. *Journal of American Chemical Society*, 135:10149–10154, 2013.

[111] Chunshan Song. Fuel processing for low-temperature and high-temperature fuel cells. Challenges, and opportunities for sustainable development in the 21st century. *Catalysis Today*, 77:17–49, 2002.

[112] B C H Steele. Appraisal of Ce1-yGdyO2-y/2 electrolytes for IT-SOFC operation at 500 Degree C. *Solid State Ionics*, 129(1-4):95–110, 2000.

[113] D. W. Strickler and W. G. Carlson. Electrical Conductivity in the ZrO2-Rich Region of Several M2O3-ZrO2 Systems. *Journal of the American Ceramic Society*, 48(8):286–289, 1965.

[114] S Swann. Magnetron sputtering. *Physics in Technology*, 19(6):67–75, 1988.

[115] I. Takeuchi, C. J. Long, O. O. Famodu, M. Murakami, J. Hattrick-Simpers, G. W. Rubloff, M. Stukowski, and K. Rajan. Data management and visualization of x-ray diffraction spectra from thin film ternary composition spreads. *Review of Scientific Instruments*, 76(6):062223, 2005.

[116] Yusuke Taki. Film Structure and Optical Constants of Magnetron-Sputtered Fluoride Films for Deep Ultraviolet Lithography. *Vacuum*, 74:431–435, 2004.

[117] Kurt A. Terrani, Chad M. Parish, Dongwon Shin, and Bruce A. Pint. Protection of zirconium by alumina- and chromia-forming iron alloys under high-temperature steam exposure. *Journal of Nuclear Materials*, 438(1-3):64–71, 2013.

[118] M.W. Thompson. II. The Energy Spectrum of Ejected Atoms During the High Energy Sputtering of Gold. *Philosophical Magazine*, 18:377–414, 1968.

[119] Office of Fossil Energy US Deparment of Energy. Why SOFC Technology?, 2016.

[120] J. A. Valles-Abarca and A. Gras-Marti. Evolution towards thermalization, and diffusion, of sputtered particle fluxes: Spatial profiles. *Journal of Applied Physics*, 55(5):1370–1378, 1984.

[121] A Vande Put, S Dryepondt, and B Pint. Cyclic Oxidation Behavior of ODS FeCrAl Alloys at High Temperature in H2O and CO2 Rich Atmosphere. In *Corrosion 2011*, pages 13–17, Houston, Tx, 2011. NACE International.

[122] A Velon and I Olefjord. Oxidation Behavior of Ni3Al and Fe3Al: II. Early Stage of Oxide Growth. *Oxidation of Metals*, 56(5):425–452, 2001.

[123] Céline Viazzi, Jean Pierre Bonino, Florence Ansart, and Antoine Barnabé. Structural study of metastable tetragonal YSZ powders produced via a sol-gel route. *Journal of Alloys and Compounds*, 452(2):377–383, 2008.

[124] R. Viswanathan, D. Gandy, and K. Coleman, editors. *Advances in Materials Technology for Fossil Power Plants: Proceedings from the Fifth Internationl Conference.* ASM International, Marco Island, Florida, 2008.

[125] Alfred Von Engel. *Ionized Gases.* Oxford University Press, 1994.

[126] Eric Wachsman, Tatsumi Ishihara, and John Kilner. Low-temperature solid-oxide fuel cells. *MRS Bulletin*, 39(09):773–779, 2014.

[127] Robert K. Waits. Planar magnetron sputtering. *Journal of Vacuum Science and Technology*, 15(2):179–187, 1978.

[128] Tao Wei, Preetam Singh, Yunhui Gong, John B. Goodenough, Yunhui Huang, and Kevin Huang. Sr3-3xNa3xSi3O9-1.5x (x = 0.45) as a Superior Solid Oxide-Ion Electrolyte for Intermediate Temperature-Solid Oxide Fuel Cells. *Energy & Environmental Science*, 7:1680, 2014.

[129] Qingzhe Wen, Donald M Lipkin, and David R Clarke. Luminescence Characterization of Chromium-Containing Theta-Alumina. *Journal of American Ceramics Society*, 81(12):3345–3348, 1998.

[130] J Will, A Mitterdorfer, C Kleinlogel, D Perednis, and L J Gauckler. Fabrication of thin electrolytes for second-generation solid oxide fuel cells. *Solid State Ionics*, 131:79–96, 2000.

[131] Peter Wray. Materials for nuclear energy in the post-Fukushima era. *American Cermic Society Bullitin*, 90(6):24–28, 2011.

[132] R.T. Wu and R.C. Reed. On the compatibility of single crystal superalloys with a thermal barrier coating system. *Acta Materialia*, 56(3):313–323, feb 2008.

[133] X. D. Xiang, Xiaodong Sun, Gabriel Briceno, Yulin Lou, Kai-An Wang, Hauyee Chang, William G. Wallace-Freedman, Sung-Wei Chen, and Peter G. Schultz. A Combinatorial Approach to Materials Discovery. *Science*, 268(5218):1738–1740, 1995.

[134] Gang Xu, Ya-Wen Zhang, Chun-Sheng Liao, and Chun-Hua Yan. Doping and Grain Size Effects in Nanocrystalline ZrO2-Sc2O3 System with Complex Phase Transitions: XRD and Raman Studies. *Physical Chemistry Chemical Physics*, 6:5410–5418, 2004.

141

[135] Osamu Yamamoto. Solid oxide fuel cells: fundamental aspects and prospects. *Electrochimica Acta*, 45(15-16):2423–2435, 2000.

[136] Osamu Yamamoto, Yoshinori Arati, Yasuo Takeda, Nobuyuki Imanishi, Yasumobu Mizutani, Masayuki Kawai, and Yasuhisa Nakamura. Electrical Conductivity of Stabilized Zirconia with Ytterbia and Scandia. *Solid State Ionics*, 79:137–142, 1995.

[137] Y. Yamamura. Contribution of anisotropic velocity distribution of recoil atoms to sputtering yields and angular distribution of sputtered atoms. *Radiation Effects*, 55:49–56, 1981.

[138] Y Yamamura and M Ishida. Monte Carlo simulation of the thermalization of sputtered atoms and reflected atoms in the magnetron sputtering discharge. *Journal of Vaccum Science and Technology*, 13:101–112, 1995.

[139] Y. Yamamura, N. Matsunami, and N. Itoh. Theoretical Studies on an Empirical Formula for Sputtering Yield at Normal Incidence. *Radiation Effects and Defects in Solids*, 71:65–86, 1983.

[140] J C Yang, E Schumann, I Levin, and M Ruhle. Transient Oxidation of NiAl. *Acta Materialia*, 46(6):2195–2201, 1998.

[141] Haijiang Yu and David R Clarke. Effect of Codoping on the R-Line Luminescence of Cr3+-Doped Alumina. *Journal of American Ceramics Society*, 85(8):1966–1970, 2002.

[142] Z. Q. Yu, R. Devanathan, W. Jiang, P. Nachimuthu, V. Shutthanandan, L. Saraf, C. M. Wang, S. V. N. T. Kuchibhatla, and S. Thevuthasan. Integrated Experimental and Modeling Study of Ionic Conductivity of Scandia-Stabilized Zirconia Thin Films. *Solid State Ionics*, 181:367–371, 2010.

[143] R Zarnetta, R. Takahashi, Marcus L Young, A. Savan, Yasubumi Furuya, Sigurd Thienhaus, B Maass, M. Rahim, J Frenzel, H Brunken, Yong S. Chu, V Srivastava, R D James, I. Takeuichi, G Eggeler, and Alfred Ludwig. Identification of Quaternary Shape Memory Alloys with Near-Zero Thermal Hystersis and Unprecidented Functional Stability. *Advanced Functional Materials2*, 20:1917–1923, 2010.

[144] Y. Zhang, B.a. Pint, J.a. Haynes, and I.G. Wright. A platinum-enriched $\gamma+\gamma$' two-phase bond coat on Ni-based superalloys. *Surface and Coatings Technology*, 200(5-6):1259–1263, nov 2005.

[145] Y W Zhang, S Jin, Y Yang, G B Li, S J Tian, J T Jia, C S Liao, and C H Yan. Electrical conductivity enhancement in nanocrystalline (RE2O3)(0.08)(ZrO2)(0.92) (RE=Sc, Y) thin films. *Applied Physics Letters*, 77(21):3409–3411, 2000.

Appendix A

Sputter Modeling Appendix

A.1 Copper Deposition Rate Results

Table A.1 contains a summary of all experimental results from the copper depositions that were used in 3.1.

Table A.1   The collected Cu deposition rate data from the crystal monitor for all experimental conditions used.

Tall Chimney Measurements			Short Chimney Measurements		
Gun Power (W)	Gun Tilt (Deg.)	Dep Rate (Å/sec)	Gun Power (W)	Gun Tilt (Deg.)	Dep Rate (Å/sec)
50	31.3	1.18	50	31.3	1.39
50	28.3	1.11	50	25.3	1.25
50	25.3	1.01	50	19.2	1.06
50	22.3	0.85	50	13.1	0.78
50	19.2	0.66	50	6.7	0.51
50	17.7	0.57	50	0	0.30
100	31.3	2.38	100	31.3	2.70
100	28.3	2.22	100	25.3	2.44
100	25.3	2.00	100	19.2	2.08
100	22.3	1.69	100	13.1	1.54
100	19.2	1.33	100	6.7	0.98
100	17.7	1.14	100	0	0.56
150	31.3	3.70	150	31.3	4.00
150	28.3	3.33	150	25.3	3.70
150	25.3	3.03	150	19.2	3.13
150	22.3	2.63	150	13.1	2.27
150	19.2	2.00	150	6.7	1.43
150	17.7	1.72	150	0	0.80
200	31.3	4.76	200	31.3	5.26
200	28.3	4.35	200	25.3	4.76
200	25.3	4.00	200	19.2	4.00
200	22.3	3.45	200	13.1	2.94
200	19.2	2.70	200	6.7	1.85
200	17.7	2.27	200	0	1.04

144

A.2 Justification For Particle Straight-Line Assumption

The assumption that sputtered particles fly in a straight-line path was validated using two approaches. In the first approach, the average number of particle collisions a Cu particle undergoes during its flight from the target to the substrate was calculated using Meyer *et al.*'s approach [79]. At the conditions used here, a Cu particle undergoes 4 collisions on average; far from the limit of thermalization. In the second approach, the energy of the Cu atoms at the substrate surface was calculated using a modified form of Valles-Abarca and Gras-Marti's model [120]. The velocity stopping approximation for thermalized particles along with the Thompson distribution of initial energy flux of particles from the target were used [118]. This calculation showed that the average energy of particles at the substrate was more than 70 times greater than the thermalized energy of the background gas (0.026 eV). Therefore, the straight-line path assumption was valid using two separate methods, justifying the expression describing the shape of the shadow cast from a circular chimney.

A.3 Sputter Model Predictions of 100 W and 200 W Copper Depositions

A.4 Sputter Model Sensitivity Analysis

Due to the non-linear nature of the model equations, relative errors of the predictions can be highly sensitive to the accuracy of the measurements used to define the system geometry. To quantify these errors, an input sensitivity analysis of the model was performed by first artificially perturbing a single geometric input of the model by a percentage of the measured value and then performing the numerical integration algorithm to calculate Υ_{pred}. In this analysis, $R_{T,Out}$, R_C, and L_C for both the short and tall chimney models were tested to determine the effect of deviations of the input on the magnitude of the predicted error. These parameters were chosen because

145
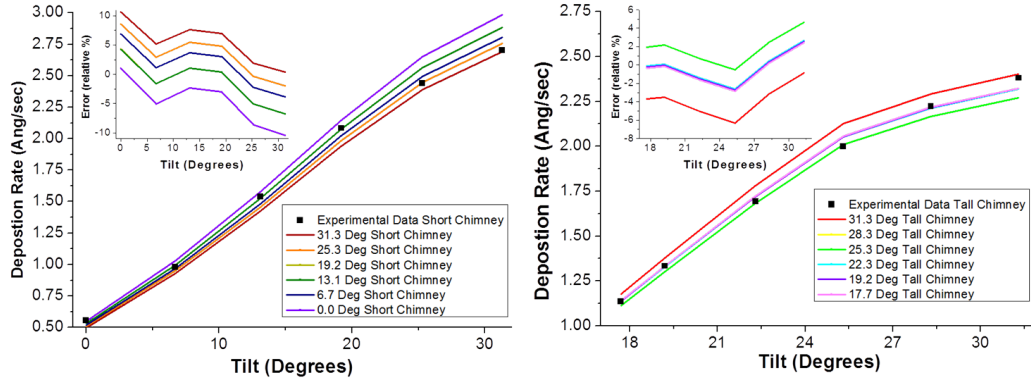
Figure A.1   The experimental (black points) and predicted deposition rates (lines) over the entire gun-tilt range for the short (Left) and tall (Right) chimney data for the 100 W model prediction. The inset plot is the relative error of the each model prediction. Each data set uses a different reference gun tilt. The figure shows that the models using a gun-tilt of 19.2° give the most accurate results when compared to the experimental data.

they are either difficult to measure or are not readily accessible, such as the $R_{T,Out}$ parameter, which is not easily measured without a well-defined target erosion ring. These obstacles can lead to errors in the model prediction. This error sensitivity analysis provides insight into how deviations in the aforementioned variables affect the error in the model prediction.

The error was calculated by subtracting the absolute error of the model using the changed geometric condition from the absolute error of a single experimentally measured geometric condition. The results for the models with a reference gun-tilt of 19.2° for the tall and short chimney models are shown in Fig. A.3 and Fig. A.4, respectively.

Figs. A.3 and A.4 do not show a systematic positive trend in the magnitude of the relative error for any geometric variable, which suggests that the measured values for each parameter were close to the actual parameter value. The tall chimney sensitivity analysis shown in Fig. A.3 reveals that in general there is a 0% to 6.4% increase in model error if $R_{T,Out}$ or L_C is less than ±8.67% of the actual value. Fig. A.3(A)

146
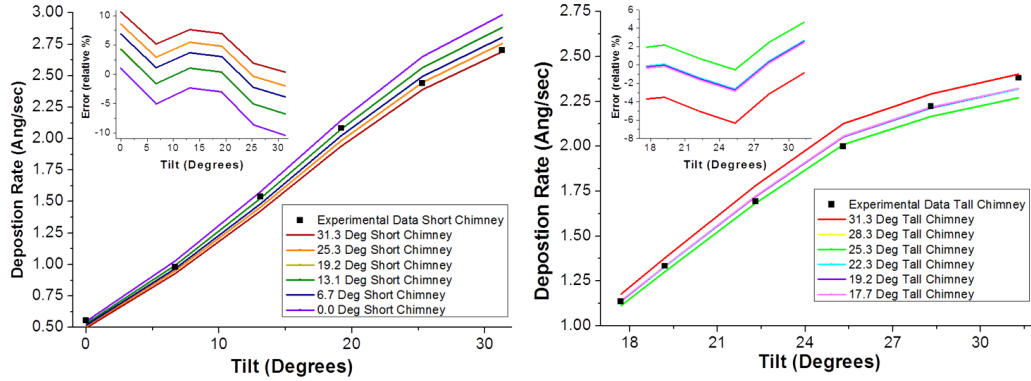
Figure A.2   The experimental (black points) and predicted deposition rates (lines) over the entire gun-tilt range for the short (Left) and tall (Right) chimney data for the 200 W model prediction. The inset plot is the relative error of the each model prediction. Each data set uses a different reference gun tilt. The figure shows that the models using a gun-tilt of 19.2° give the most accurate results when compared to the experimental data.

and Fig. A.3(C) show that the error increases 17.25% if L_C or $R_{T,Out}$ is greater than ±8.67% of the actual value. Fig. A.3(B) shows that the model has a similar response to a ±8.67% error in R_C when compared to the other variables, but that the error of the model quickly increases by more than 30% if there is greater than ±8.67% error in R_C. All of the subplots in Fig. A.3 show that the model is more sensitive if the gun-tilt of the prediction is higher.

Fig. A.4 shows that, similar to the tall chimney models, the short chimney models are more resilient to an error in $R_{T,Out}$ and L_C than to an error in R_C. The short chimney sensitivity analysis shows that in general, for all of the tested parameters, a ±14.73% error in the measured parameter will increase the model error by less than 7.94%. Exceptions to this statement are shown in Fig. A.4(B) for a >6.27% change in R_C for slightly tilted models (< 3.77° tilt) and Fig. A.4(C) for a >4.90% error in $R_{T,Out}$ for highly tilted models (> 30.40° tilt). In the case of a slightly tilted model with a >6.27% error in R_C the model error can increase by up to 15.71%. In the case of a highly tilted model with a >4.90% error in $R_{T,Out}$, the model error increases

147
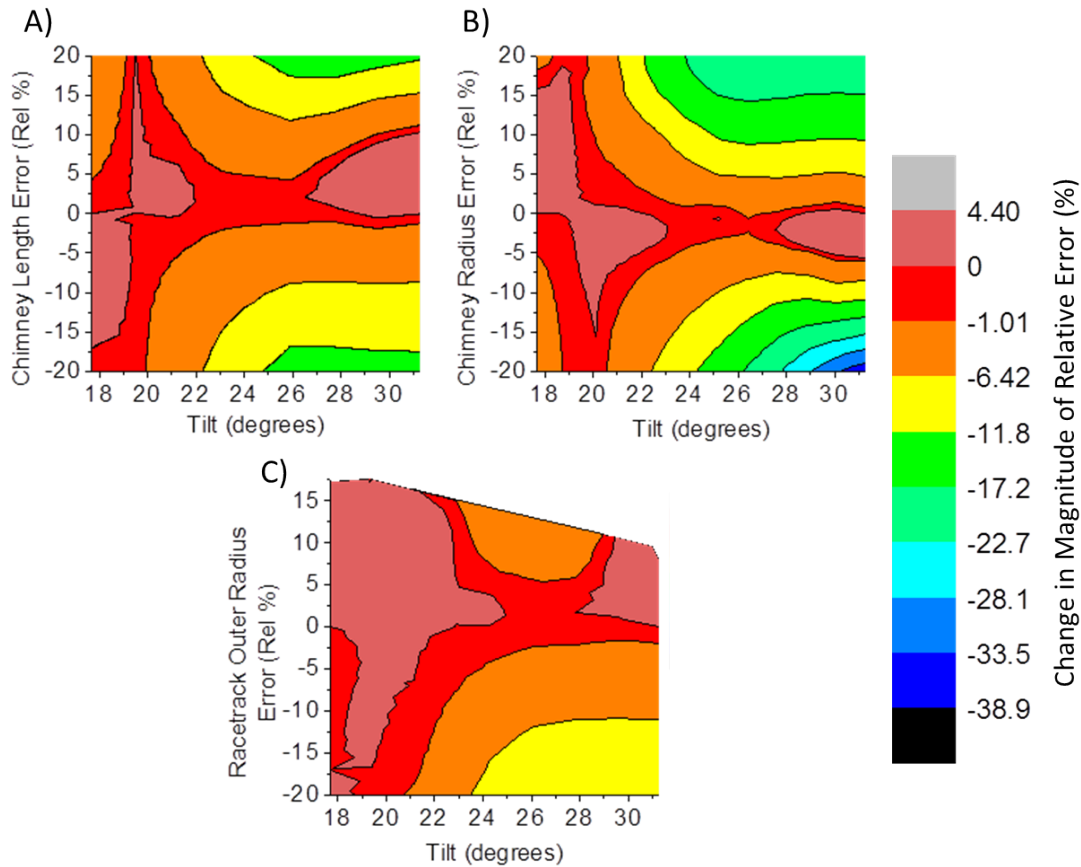
Figure A.3 Sensitivity analysis performed for the 50 W data for the tall chimney models calibrated at 19.2° gun-tilt. Plot A) shows the results with the chimney length changed, plot B) shows the results with the chimney radius changed, and plot C) shows the results with the outer racetrack radius changed.

by up to 11.83%. This trend in the error is similar to the error trend seen in the large chimney models, and has a similar physical explanation: at highly titled gun geometries less of the target is shadowed and so an increase in the radius of the target would have a substantial effect on the amount of the being target shadowed.

The sensitivity analysis indicates that, for small chimney models, a 8.67% error in any of the input parameters will introduce less than 6.4% error in the model prediction. It also indicates that, for a tall chimney model, a 14.73% error in any of these input will introduce less than 7.94% error in the model prediction with the exception of highly tilted models with a >4.90% error in $R_{T,Out}$, which showed an
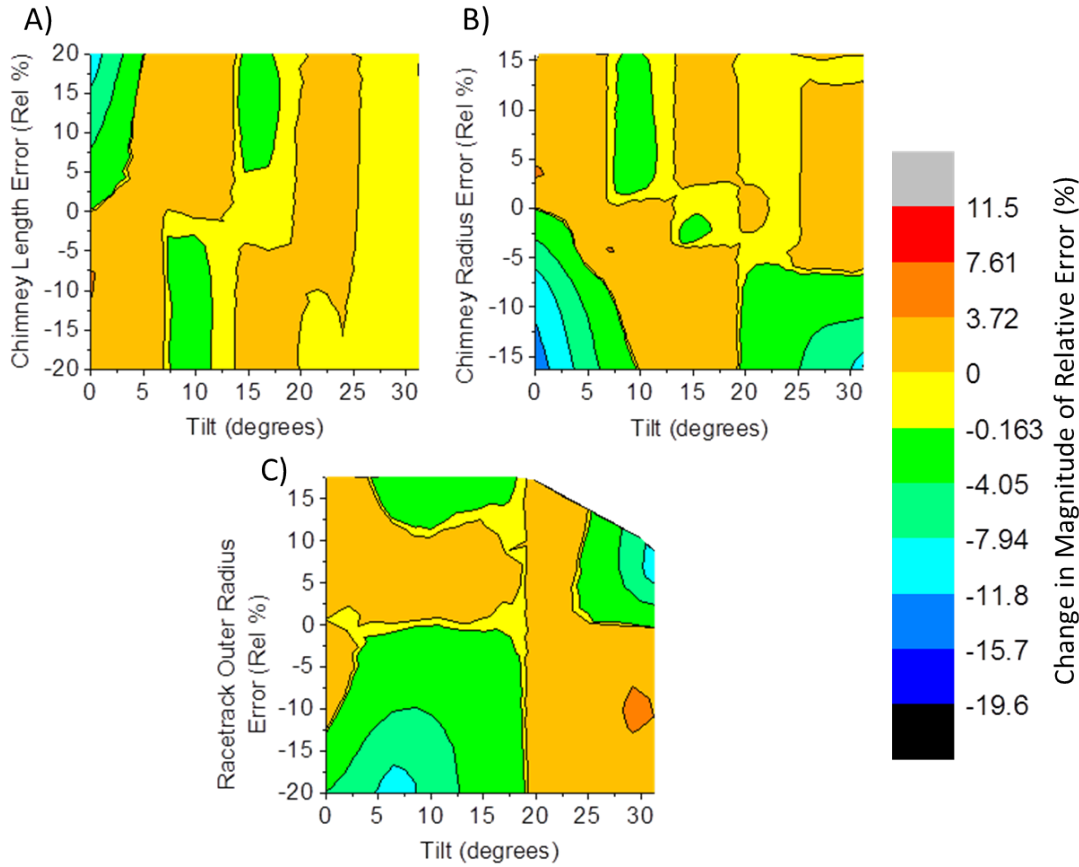
Figure A.4 Sensitivity analysis performed for the 50 W data for the short chimney models calibrated at 19.2° gun-tilt. Plot A) shows the results with the chimney length changed, plot B) shows the results with the chimney radius changed, and plot C) shows the results with the outer racetrack radius changed.

increase in the model error to up to 11.83%, or for a slightly tilted model, a $>6.27\%$ error in R_C, which showed an increase in the model error up to 15.71%. This shows that for the small chimney models, the input parameters do not need to be as accurate as they do for tall chimney models. The analysis also shows that, if there is deviation in the measurement for $R_{T,Out}$, the model losses predictive capabilities at gun tilts much higher than the calibration tilt (predicted gun-tilt $> 11.2°$ calibration gun-tilt), or if there is deviation in the measurement of R_C then tall chimney models lose predictive capabilities. This is important because of the difficulty in measuring $R_{T,Out}$ and R_C.

149

A.5 Secondary Sputter Model Optimization Validation

The sensitivity and performance of the optimization procedure on the experimentally measured deposition rate profile was evaluated. While the optimization procedure is not intended to determine the sputtering conditions of a characterized thin film, the noisy experimental data will act as a surrogate for a non-ideal deposition rate spread, i.e., a deposition rate spread that cannot be obtained exactly for a specific sputtering geometry. This is important to analyze because it is likely that the optimization procedure will be used to determine deposition spreads that are created based on experimental needs. The film was simulated at each of the 24 experimentally measured points and the Frobenius norm of the difference of the simulated and measured deposition rates was calculated. The discrepancy between the experimental and simulated data as measured by the Frobenius norm was 0.799, which served as the benchmark optimization objective value for accuracy; meaning if the optimization produced a film whose difference from the simulated film had a Frobenius norm of less than or equal to 0.799, the optimization was considered to be a success.

The optimization procedure was performed using n_{seed} of 100 points and n_{start} of 2 due to the high accuracy and fast calculations times this condition showed in section 3.2. The optimization was repeated 100 times. Only the optimized sputtering conditions with the lowest objective function values were used during analysis. The average optimized sputtering condition and objective function value were calculated. The average objective value was 0.494, 38% lower than the Frobenius norm value calculated when the model was directly compared to the measured results. This lower objective function value shows that the optimization was successful in minimizing the difference between the optimized and measured deposition rate values, and successfully determined a valid sputtering condition.

On average, the optimization determined that the film should be sputtered with a 101 W gun power, a 62° gun tilt, and a substrate height of 68 mm (see Table 3.3,

150

Condition 1 for expected value). The optimized sputtering conditions were 42.8%, 10.1%, and 19.4% different than the expected values for the gun power, gun tilt, and substrate height, respectively. The reason the optimized and expected sputtering conditions are different, but both yield similar films, is shown in the response plots of Fig. 3.6. As previously stated, close to the optimal sputtering condition, the response surface flattens out and the value of the objective function is close to 0 if multiple sputtering conditions are changed in a coupled manner. This means that slight errors from the measurement and model can shift the optimal sputtering conditions, and will yield a very similar deposition rate profile.

This analysis shows that the optimization procedure can determine sputtering conditions that would yield a deposition rate profile within the error of the experimentally measured and simulated deposited thin film. It also showed that the proposed procedure determined a sputtering condition that was different than the expected sputtering condition. This difference is due to errors of the model, noise in the measured values, and the flat response surface around the minimum. This flat response surface shows that if the sputtering conditions are changed in a coupled manner very similar deposition rate spreads will be obtained.

151

Appendix B

SS-AutoPhase Appendix

B.1 Crystal Phase Predictions
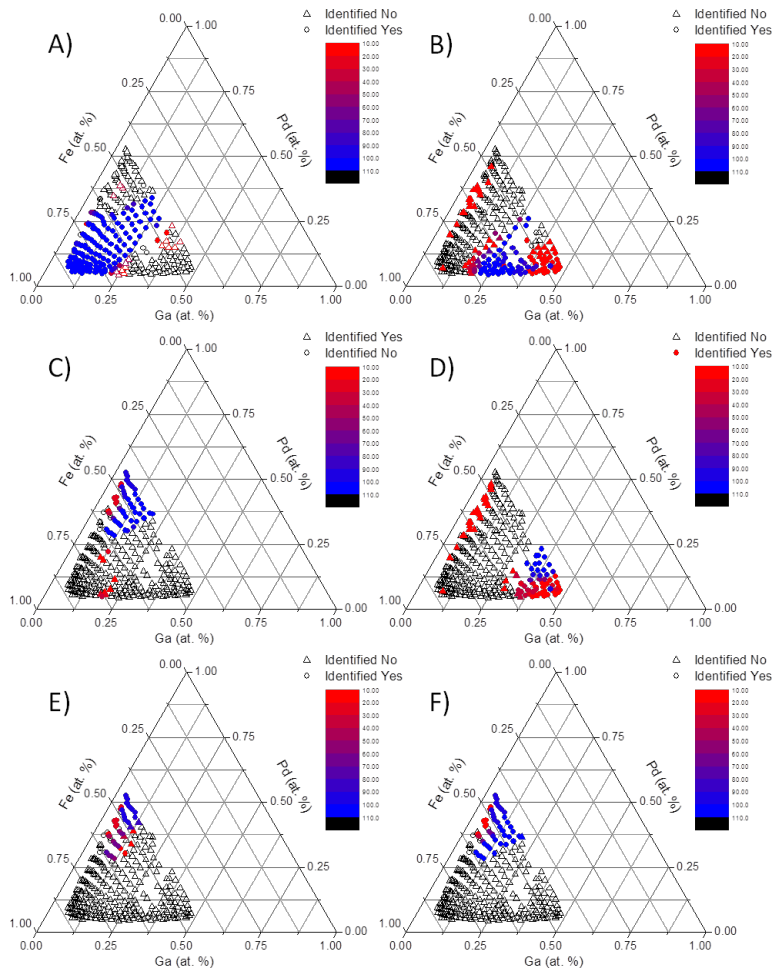
Figure B.1   The phase predictions for A) BCC Fe, B) FCC Fe, C) FCC FePd, D) Hexagonal FeGa, E) Pd_9 and Fe_3Si, and F) Unknown 2. The data point shape indicates what the result from the MEPMA was; circle-identified as present, triangle-identified as not present. The data point color indicates the number of repeats that labeled a data point as containing the phase.

Appendix C

Copyright Permission

Figure C.1   Copyright permission for J. K. Bunn, C. J. Metting, and J. R. Hattrick-Simpers, (2015). A Semi-Empirical Model for Tilted-Gun Planer Magnetron Sputtering Accounting for Chimney Shadowing. JOM, 67(1), 154-163.

Figure C.2   Copyright permission for J. K. Bunn, R. Z. Voepel, Z. Wang, E. P. Gatzke, J. A. Lauterbach, and J. R. Hattrick-Simpers, (2016). Development of an Optimization Procedure for Magnetron-Sputtered Thin Films to Facilitate Combinatorial Materials Research. Industrial and Engineering Chemistry Research, 55(5), 1236-1242.

Figure C.3 Copyright permission for C. J. Metting, J. K. Bunn, E. Underwood, S. Smoak, J. R. Hattrick-Simpers, (2013). Combinatorial Approach to Turbine Bond Coat Discovery. ACS Combinatorial Science, 15(8), 419-424.

Figure C.4   Copyright permission for J. K. Bunn, J. Hu, and J. R. Hattrick-Simpers, (2016). Semi-Supervised Approach to Phase Identification from Combinatorial Sample Diffraction Patterns. JOM, 68(8), 2116-2125.

Re: Reprint Permission

KS Kathryn Shaw <Kathryn.Shaw@iop.org> on behalf of Permissions <permissions@iop.org>

🖕 ↩ Reply all | ∨

Mon 10/17, 4:43 AM
BUNN, JONATHAN ⮟

Inbox

💬 | Action Items 🔒

Dear Jonathan Kenneth Bunn,

Thank you for your email and for taking the time to seek this permission.

We can allow you to use figures in your thesis, even if it is going on ProQuest. It is only the entire article which we won't allow to go on proQuest.

Therefore, please include citation details, "© IOP Publishing. Reproduced with permission. All rights reserved" and for online use, a link to the Version of Record.

Please let me know if you have any further questions.

In the meantime, I wish you the best of luck with the completion of your dissertation.

Kind regards,

Kathryn Shaw

Copyright & Permissions Team
Gemma Alaway – Rights & Permissions Adviser
Kathryn Shaw - Editorial Assistant

Figure C.5   Copyright permission for J. K. Bunn, R. L. Fang, M. R. Albing, A. Mehta, M. J. Kramer, M. F. Besser, and J. R. Hattrick-Simpers, (2015). A high-throughput investigation of Fe-Cr-Al as a novel high-temperature coating for nuclear cladding materials. Nanotechnology, 26(27), 274003.